Theses and Dissertations

5-2017

Controlled Synthesis and Utilization of Metal and Oxide Hybrid Nanoparticles

Cameron Cowgur Crane
University of Arkansas, Fayetteville

Recommended Citation

Controlled Synthesis and Utilization of Metal and Oxide Hybrid Nanoparticles

A dissertation submitted in partial fulfilment
of the requirements for the degree of
Doctor of Philosophy in Chemistry

by

Cameron Crane
Hendrix College
Bachelor of Arts in Chemistry, 2011

May 2017
University of Arkansas

This dissertation is approved for recommendation to the Graduate Council.

_____
Dr. Jingyi Chen
Dissertation Director

_____
Dr. Jim Hinton
Committee member

_____
Dr. Bill Durham
Committee member

_____
Dr. Ryan Tian
Committee member

_____
Dr. Colin Heyes
Committee member

Abstract

This dissertation reports the development of synthetic methods concerning rationally-designed, hybrid, and multifunctional nanomaterials. These methods are based on a wet chemical, solution phase approach that utilizes the knowledge of synthetic organic and inorganic chemistry to generate building blocks in solution for the growth of nanocrystals and hybrid nanostructures. This work builds on the prior knowledge of shape-controlled synthesis of noble metal nanocrystals and expands into the challenging realm of the more reactive first row transition metals. Specifically, a microemulsion sol-gel method was developed to synthesize Au-SiO_2 dimers as precursors for the synthesis of segmented heterostructures of noble metals that can be used for catalysis. This microemulsion sol-gel method was modified to synthesize an aqueous suspension of oxidation-resistant Cu-SiO_2 core-shell nanoparticles that can be used for sensing and catalysis. A thermal decomposition approach was developed, wherein zero-valence metal precursor complexes in the presence of seed nanoparticles produced metal-metal oxide core-shell structures with well-controlled shell thickness. This method was demonstrated on $AuCu_3$-Fe_3O_4, $AuCu_3$-NiO, and $AuCu_3$-MnO core-shell systems. Switching the core from $AuCu_3$ alloy to pure Cu, this method could extend to Cu-Fe_3O_4 and Cu-MnO systems. Further etching the Cu core in these core-shell structures led to the formation of the hollow metal oxides which provides a versatile route to hollow nanostructures of metal oxides. This work develops the synthetic library of tools for the production of hybrid nanostructures with multiple functionalities.

Acknowledgements

I would like to thank my parents, Tim and Beth, from whom I learned curiosity and grit -the stuff one needs plenty in the research lab. And I would like to thank Angela, who supported me through all of the challenge graduate school offers. I would also like to thank my academic advisor and mentor, Professor Jingyi Chen, who guided me through graduate school, as well as Dr. Shutang Chen who introduced me to nanoparticle synthesis. I would like to thank the members of my graduate committee: Dr. Jingyi Chen, Dr. Jim Hinton, Dr. Bill Durham, Dr. Ryan Tian, and Dr. Colin Heyes for their invaluable advice which was always useful and generously provided. And I would like to thank the other students in the Chen lab that provided me with priceless advice and encouragement.

Table of Contents

Chapter III.   Synthesis of Copper-Silica Core-Shell

  Nanostructures with Sharp and Stable Localized

List of Abbreviations

LSPR	Localized Surface Plasmon Resonance
MASG	Mask Assisted Seeded Growth
TEM	Transmission Electron Microscopy
HRTEM	High Resolution Transmission Electron Microscopy
XRD	X-Ray Diffraction
UV-vis	Ultra Violet-visible
AA	Atomic Absorption
SERS	Surface Enhanced Raman Spectroscopy
ORR	Oxygen Reduction Reaction
TM	Transition Metal
TOP	Tri-n-octylphosphine
OLAM	Oleylamine
TEOS	Tetraethoxysilane
PVP	polyvinylpyrrolidone
TDA	Tetradecylamine
ODE	Octadecene
$Cu(acac)_2$	Copper (II) 2,4-pentanedionate
DDA	Discrete Dipole Approximation
FFT	Fast Fourier Transform
rcf	Relative centrifugal force

List of Tables and Figures

Chapter III

Chapter IV

List of Published Articles

Chapter 2: Mask-Assisted Seeded Growth of Segmented Metallic Heteronanostructures

Cameron C. Crane, Jing Tao, Feng Wang, Yimei Zhu, and Jingyi Chen
The Journal of Physical Chemistry C **2014** *118* (48), 28134-28142
DOI: 10.1021/jp5094433

Chapter 3: Synthesis of Copper-Silica Core-Shell Nanostructures with Sharp and Stable Localized Surface Plasmon Resonance

Cameron C. Crane, Feng Wang, Jun Li, Jing Tao, Yimei Zhu, and Jingyi Chen
The Journal of Physical Chemistry **2017**, *121* (10), 5684–5692
DOI: 10.1021/acs.jpcc.6b11891

1. Introduction

1.1 Noble Metal Nanostructures

1.1.1 Advantages of Nanomaterials

Nanostructures, also referred to as nanoparticles, are solid structures with at least one dimension between 1 and 100 nanometers (nm) in length.[1] In this work, metal and metal-oxide nanostructures are produced using wet-chemical methods familiar to synthetic chemistry. These nanostructures are a small portion of a great body of contemporary research across all divisions of the physical and life sciences.[2-5] The potential rewards for controlling matter at the nanoscale are difficult to overstate; as described by the famous Richard P Feynman, "There is plenty of room at the bottom"; meaning firstly, that even after the revolutionary advances in physics and chemistry in the first half 20th century, the amount of productive and exciting research from the study of the extremely small is enough to keep scientists busy well into the 21st century. Secondly, moving to the nanoscale is not simply a matter of incremental scaling down of familiar physics from the macroscale, but that new emergent properties of matter will provide fruitful study.[6]

Nanoparticles find applications in virtually every discipline: Semiconducting nanoparticles have been incorporated into light emitting diodes for televisions and computer monitors[7], used as fluorescence imaging tools[8], and explored as a data storage medium to enhance data storage capacity in computer memory[9]. Metallic nanostructures have been used since antiquity as coloring agents in transparent solids. For instance, the stained glass in gothic era churches, the famous Lycurgus Cup, and Michael Faraday's curious gold colloid all derive their remarkable properties from the optical effect of metallic nanostructures interacting with visible light.[10] The

remarkable optical properties of metal nanoparticles are used today in Surface Enhanced Raman Spectroscopy (SERS) to amplify the analyte signal so dramatically that single molecules and their constituent covalent bonds can be spectroscopically probed and imaged.[11] In fact, optically active nanoparticles can outperform many conventional organic dyes by enhancing the absorption efficiency and operate at many different wavelengths of light.[12] Ag and Cu nanoparticles are used as extremely efficient antimicrobial agents.[13] Magnetic nanoparticles of a specific small size range, known as superparamagnetic nanostructures, can be used to enhance the contrast of medical MRI imaging, resulting in superior imaging of malignant tissues, leading to improved chances of diagnosis and detection of cancer.[14] Additionally, nanostructures offer an exciting and promising platform as a drug delivery vehicle, inspiring new classes of antibiotics and anti-cancer drugs in which nanoparticles are injected into a patient, where they are designed to travel to a tumor or damaged tissue site and release their payload of cancer therapy drug or antibiotics.[15,16]

Precise control over the fabrication of materials at the nanoscale offers a route to implement myriad improvements over materials produced with conventional processing techniques: A direct result of working at the nanoscale is the savings in the volume of materials required, indeed, the amount of material that can be conserved by converting conventional materials to nanoscale size regime is difficult to overstate.[17] Because of the high costs of many materials used in the chemical industries, microprocessors, or in precious metal catalysis, many product designs that would otherwise function exceptionally well are never pursued because of the volume of prohibitively expensive of materials required.[18]
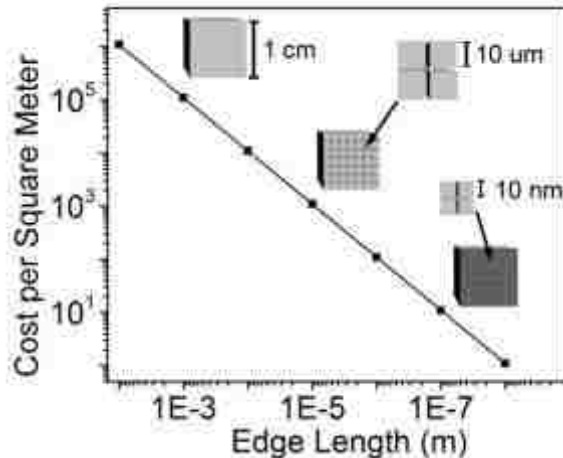
Figure 1: Illustration of cost and material savings from reducing particle size to the nanoscale. 1 cubic centimeter of platinum exhibits 6 cm^2 surface area as a single piece, but divided into 10 nm cubes, the same amount of platinum exhibits 60,000 cm^2.

Using the precious metal platinum as an example in a thought experiment shown in **Figure 1**, a piece of platinum is first presented as a solid cube, 1 cm on a side. Continuing the experiment, the same cube of platinum has been divided into cubes that are 10 um on a side. Now, with the same amount of platinum, the cost per square area has decreased one thousand fold, and by the time the cubes are divided again to be 10 nm on a side, the cost has decreased 1 million fold. In this way, the cost can be driven down orders of magnitude by increasing the surface area of the platinum for a static mass of metal; because the surface is where the chemistry happens, any internal volume of platinum is wasted, coupled with the cubic relationship of volume to edge length, the amount of available surface area increases 1 million times as the edge length decreases from 1 cm to 10 nm, and the normalized cost per surface area decreases from 1 million dollars, to 1 dollar per square meter. Of course, producing large quantities of nanometer scale particles is easier done in this thought experiment than in practice. As the size of metals is reduced to the nanoscale, in addition to increasing the surface area, many interesting properties begin to emerge that are not manifest in the bulk material, making nanoscience an exciting field

3

to study.[19] These emergent properties most germane to the materials herein are introduced below.

1.1.2 Localized Surface Plasmon Resonance
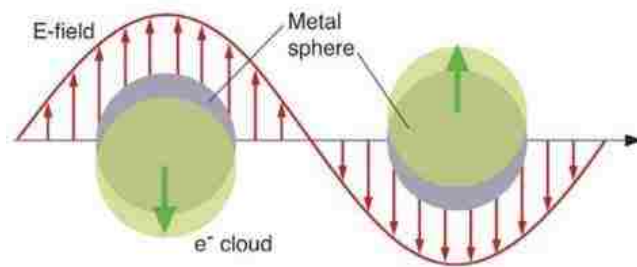
Figure 2 Schematic illustration of the electron cloud of a metallic nanoparticle interacting with the electromagnetic field of visible light. (Reproduced by permission from reference 21 Copyright © 2003 American Chemical Society.)

$$C_{ext} = \frac{24\pi^2 R^3 \varepsilon_m^{3/2}}{\lambda} \frac{\varepsilon''}{(\varepsilon'+2\varepsilon_m)^2+\varepsilon''^2} \qquad (1)$$

In equation (1), R is the radius of the sphere, λ is the wavelength of light, ε_m is the surrounding dielectric medium, and $\varepsilon'(\lambda) + i\varepsilon''(\lambda)$ is the wavelength dependent complex dielectric function of the material.[10] The mean free path for electron in metals near room temperature is 10-100 nm.[20] Resultantly, something very interesting happens when the size of the metal particle is in the 10-100 nm size range; localized surface plasmon resonance (LSPR) occurs, and is the phenomenon where conduction electrons oscillate sympathetically with incident electromagnetic radiation as shown above in **Figure 2**.[21] The optical spectra of colloidal nanoparticles, occurring in the visible spectral range for particles made of Au, Cu, and Ag, are defined by both absorption

4

and scattering of light. Mie's solution to Maxwell's equations for metallic spheres provides an

excellent explanation for the LSPR effect contributing to the absorption component.[22] Au and

Ag are the most dependable materials to prepare such nanoparticles due to their resistance to

oxidation, or 'noble' character. Although examples of Cu nanoparticles exhibiting LSPR exist,

they are exceedingly rare due to the susceptibility of Cu to oxidize in ambient, and especially

aqueous, conditions.[23] As discussed below, the absorption arising from LSPR combines with the

light scattering effect to produce the net extinction spectrum, which has advantages over

conventional organic dyes.[12]
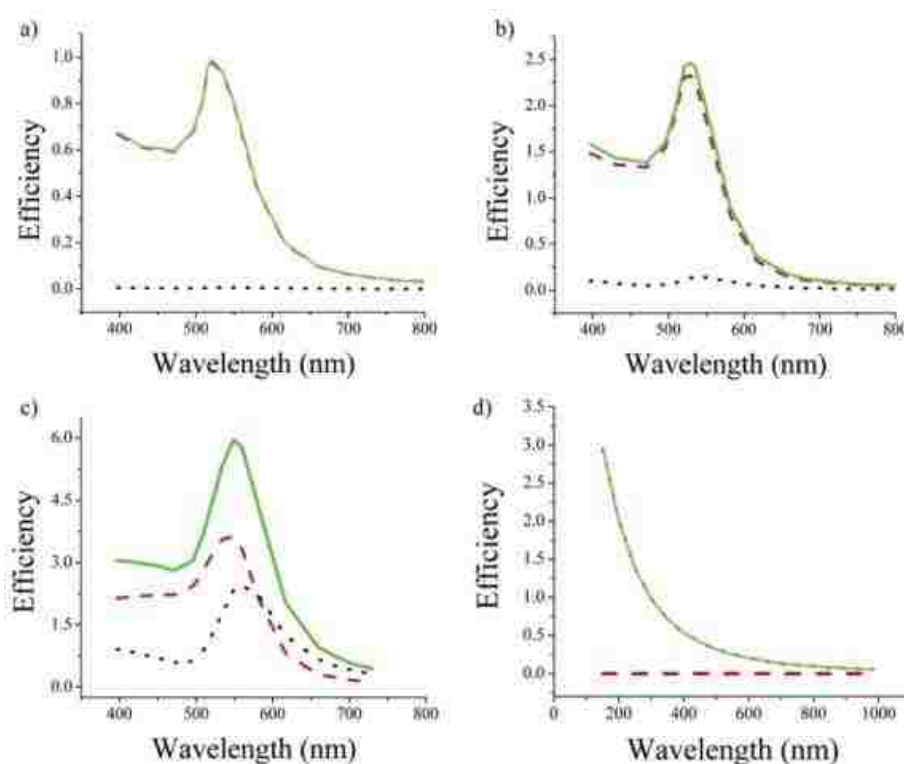
Figure 3: Calculated spectra of the efficiency of absorption Q_{abs} (red dashed), scattering Q_{sca} (black dotted), and extinction Q_{ext} (green solid) for gold nanospheres (a) D) 20 nm, (b) D) 40 nm, (c) D) 80 nm, and polystyrene nanospheres (d) D) 300 nm. (Reproduced by permission from reference.24   Copyright © 2006 American Chemical Society.)

The scattering and absorption components of Au nanoparticles combine to produce the effective extinction spectrum as shown in **Figure 3**, the black dotted line is the scattering component, and increases drastically in efficiency, Q_{ext}, as the Au nanoparticles increase in size from 20, to 80 nm. The absorption efficiency, Q_{abs}, also increased with the Au nanoparticle size, although for the 20 nm particles, the extinction spectrum is produced by absorption only. When the LSPR active particles are replaced by polystyrene particles, the extinction efficiency, Q_{ext}, is derived entirely from the scattering component. The absorption efficiency is approximately five time greater than conventional dyes, and the scattering of larger, ~80 nm Au, particles exhibit higher scattering than other dark field imaging particles, such as polystyrene microparticles.[24]
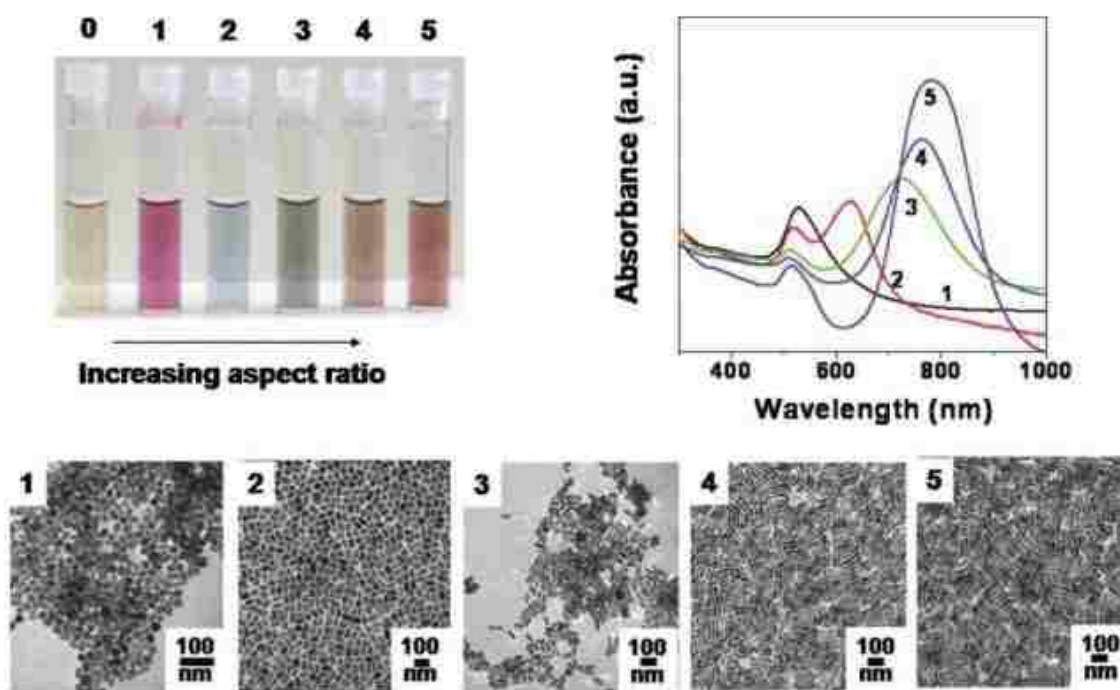
Figure 4: Aqueous suspensions of 4 nm gold nanospheres (vial 0) and progressively higher aspect ratio gold nanorods, as shown in TEM images 1-5. The extinction spectra are shown at top right corresponding to 1-5. (Reproduced by permission from reference 20. Copyright © 2008 Royal Society of Chemistry.)

In addition to the dielectric environment and metal comprising the nanostructure, the shape of the nanostructure affects the mean free path of the oscillating conduction electrons and alters the energy of maximum absorption from the LSPR.[25] By carefully controlling of the reaction conditions that generate the nanostructure, the length of Au and Ag nanorods have been produced to extend the LSPR as far as 1600 nm, well into the near infrared region (NIR).[26] This has practical value for sensing applications, such as Raman spectroscopy, as the nanorods aspect ratio's effect on the LSPR profile provides a route to match common laser wavelengths with the maximum LSPR absorption for optimized signal strength.[27] Furthermore, the spectral NIR region is necessary for applications inside biological systems, referred to as the biological transparent window due to the high penetration into tissue.[16] As shown in **Figure 4**, increasing the aspect ratio of Au nanorods changes the color of the solution, and the lambda max, from 520 nm for spherical Au particles, to 800 nm for 100 nm Au nanorods. Also shown in the spectra, are the two modes of the plasmon, the longitudinal arising from the wave propagating the length of the rod, and the transverse originating from the width of the rod, allowing for multiple wavelengths of excitation.

1.1.3   Metal Nanostructure Synthesis

1.1.3.1 Synthetic Strategies

Approaches to manufacturing nanostructures can be broadly grouped into two categories: The top-down and bottom-up approaches comprise all nanostructure production techniques.[28] As depicted in **Figure 5**, the Top-Down approach starts with the bulk, or macroscale, material and mechanically converts the material to the nanoscale through grinding, cutting, or other means. This strategy has the advantage of scalability which suits it well for industrial settings, but has

7

disadvantages when the material is very rare or expensive, such as platinum or gold, or if fine

shape control is necessary.
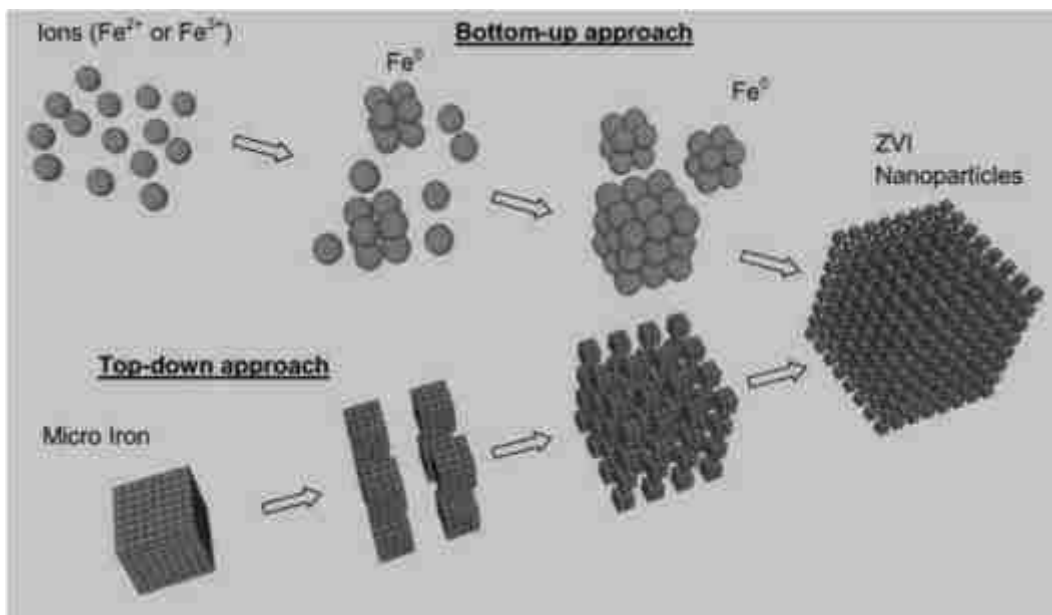
Figure 5: Representation of Top-Down and Bottom-Up approaches to generating nanostructures. (Reproduced by permission from reference 29. Copyright © 2009 Royal Society of Chemistry.)
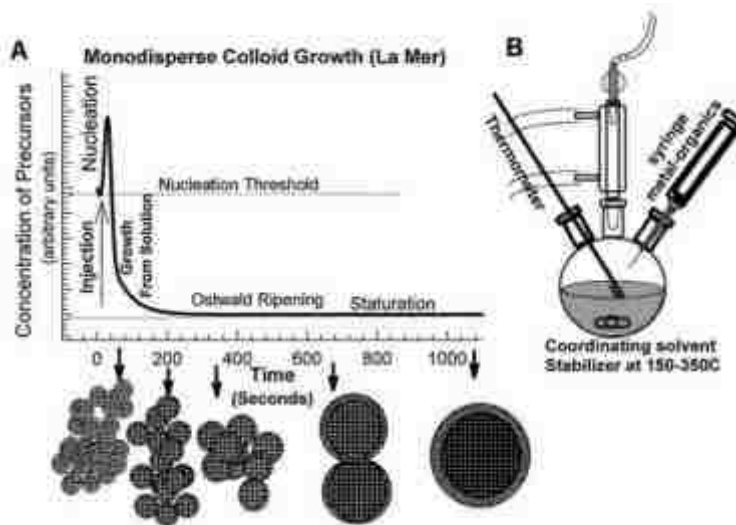
Figure 6: (A) Schematic of a typical solution phase nucleation and growth of crystals using (B) an illustration of a setup used to produce nanocrystals. (Reproduced by permission from reference 30. Copyright © 2000 Annual Reviews.)

The bottom-up approach, as the name suggests, is essentially the reverse of the top-down approach; rather than breaking apart matter, nanostructures are formed by building the structure from atoms. This latter approach takes a que from nature, and relies largely on nucleation and crystal growth to produce uniform and shapeable nanostructures.[31] The advantage of the bottom-up approaches is uniformity, shape control, and very little material requirements. The disadvantages are the low yields produced, potential for scalability, high temperatures required, and purification of the products. For example, the precipitation of snow or rain, beginning with humid air, followed by condensation and eventual precipitation is an example of a colloidal bottom up approach to produce water particles as solid crystals or liquid drops, respectively.[32] To contrast with a bottom up approach, the thought experiment depicted in **Figure 1** would be

considered a Top-Down method, where a solid block is sequentially, broken into many smaller pieces of the same material.

The nanostructures described herein were produced using a bottom-up wet-chemical approach, utilizing a set up as depicted in **Figure 6B**, consisting of a solution of precursors under inert gas inside a round bottom flask, magnetically stirred. Metallic nanocrystal precursors can be injected using air free techniques as shown; by taking advantage of the physics of colloidal crystal growth, complex heteronanostructures can be produced. As shown in **Figure 6A**, the initial nanoparticle nucleation occurs after a critically high concentration of nuclei are present in solution, after which the first crystals are formed, which quickly, acting as seeds for further nanoparticle growth, deplete the remaining nuclei from the solution.[33] As will be discussed below, if multiple metals are present in the solution, a seeded co-reduction occurs, which has implications for the final composition and shape.[34] After the growth phase, secondary and tertiary metals can be added to alloy with the seeds or undergo heterogeneous growth, forming a shell on the first material. Through selection of temperature, reaction rate, and use of surfactants, a precise shape can be selected; resultantly, the overall reaction can be complex, and the key points germane to the following chapters are outlined below.

1.1.3.2 Shape Controlled Synthesis
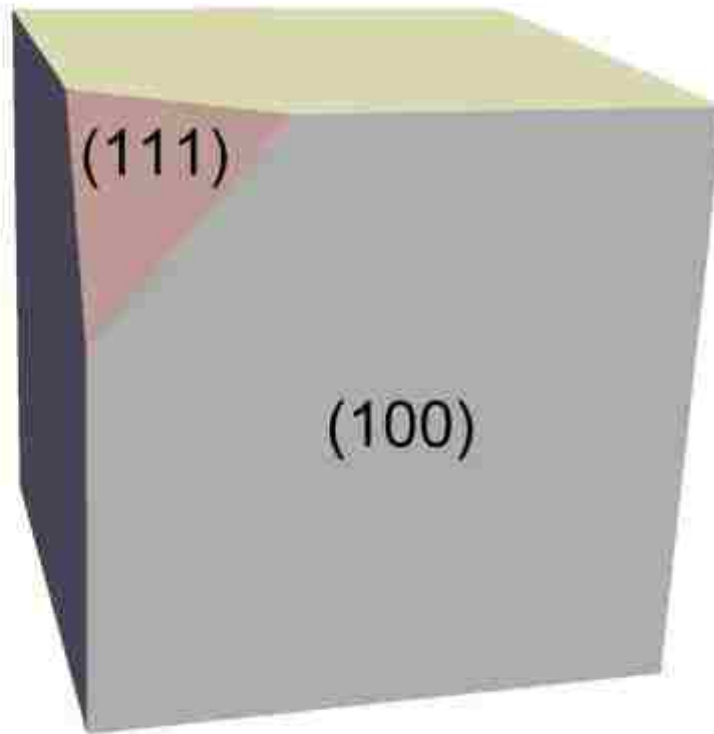
Figure 7: Cube of *fcc* material exhibiting 6 faces of (100), and truncated corner of a (111) surface facet.

Through careful selection of surfactant, oxidizing environment, and reducing environment, the relative growth rates on the surface of a nanocrystal can be promoted relative to others, controlling the final crystal shape. Herein, 'growth' of nanocrystals refers to the addition of atoms to a crystal surface, becoming incorporated into the nanocrystal. For Au, Cu, and Ag, which are typical nanocrystal materials due to their optical and catalytic activity, the atoms arrange themselves as face centered cubic or *fcc*. For an *fcc* single crystal, if growth on the <100> direction proceeds faster than <111>, a truncated octahedron or perfect octahedron will be produced as the (111) facet, shown as the brown surface in **Figure 7**, increases in surface area. Conversely, if the growth rates are reversed, such that atoms are added faster to the <111> surfaces than the <100>, the truncated surfaces will disappear, producing truncated cubes, or ultimately perfect cubes of 6 (100) faces if the growth proceeds to completion.[35]

As mentioned above, the conversion of a cube into an octahedral structure and vice versa, is true for single crystal particles; introducing crystals with stacking faults referred to as "twinned" or "multiply twinned" seeds can have a dramatic effect on the potential shapes of the final crystal or alloy.[36] Twinning can be minimized by introducing an etchant, or oxidant, into the reaction during the early formation of crystal nuclei, during the period between reduction of ions into atoms and crystal seed growth as shown in **Figure 6**, to chemically attack the twin boundaries of the formed crystal seeds. Alternatively, Twining can be enhanced by adding reagents, such as NaBr in the case of Ag, and makes the difference between singly twined bipyramids and single crystal cubes.[37]

Structures	Shapes	Schematic drawings	Metals
single-crystal	perfect/truncated cube[a]		Pd, Ag, Au, Pt, Cu, Rh, Bi, Fe
	perfect/truncated octahedron[a]		Pd, Ag, Au, Pt
	perfect/truncated tetrahedron[a]		Ag, Au, Pt, Rh
	rectangular bar		Pd, Ag, Pt
	octagonal rod		Pd, Au, Fe, Co, Ni
	rectangular or octagonal wire		Pb, In, Sn, Sb, Fe, Co
singly twinned	right bipyramid		Pd, Ag
	beam		Ag
multiply twin-ned	decahedron[a]		Pd, Ag, Au
	icosahedron[a]		Pd, Au
	five-fold twinned pentagonal rod		Pd, Ag, Au, Cu
	five-fold twinned pentagonal wire		Ag, Au, Cu
	triangular/hexagonal plate		Pd, Ag, Au, Cu, Pb, Bi, Co, Ni
	disc		Sn, Co

[a] Platonic solid.

Figure 8: Table of nanocrystalline shapes resulting from *fcc* metals of single crystal, singly twinned, and multiply twinned seeds. (Reproduced by permission from reference[38]. Copyright © 2009 WILEY-VCH Verlag GmbH & Co. KGaA, Weinheim.)

13

The seeds with twinning are more susceptible to oxidative etching due to the high surface energy of the facet boundary and are etched slightly more often than the seeds that survive the oxidizing environment in greater numbers.[39] In a properly designed reaction, the seeds return to constituent atoms and then re reduce many times. As this process is repeated in the presence of an etchant, the colloid will 'evolve' only single crystal nuclei that can mature into nanoparticles of single crystal character. Conversely, as shown in **Figure 8**, there are additional shapes possible when the particles are twinned, and this requires an environment with little etching activity.[38]

As discussed below in section 1.2, alloyed nanostructures can offer advantages over monometallic nanostructures. The successful of shape control of monometallic nanostructures does not translate perfectly to the shape control of alloyed nanostructures; however, the change in activity of the constituent metals provides an opportunity to introduce varying shapes and compositions of metal. For example, a seeded co-reduction approach can produce a variety of nanostructures of noble metals. Multiply twinned Au nano particles take on a decahedral form as shown in **Figure 8**, were found to produce Au_xCu_{1-x} nanorods as shown in **Figure 9** when Au and Cu atoms were present in the reaction solution with the Au seeds.[40] The five-fold twinned surface were found to be critical to the final shape; the reactive twin crystal boundaries seeded the growth of Cu atoms, producing a Cu rich side of the Au particle. This Cu portion simultaneously alloys with the Au, and continues to grow as Cu and Au atoms are added. This co-reduction approach grows the decahedra into a nanorod, through co addition of Cu and Au atoms in the direction of the five-fold twin axis until the reagents Au and Cu are depleted. These types of reactions follow the experimental set up described in **Figure 6**, but include a second injection of crystal growth material, in this case Cu, to initiate the co-reduction and produce the

14

rods. This approach is significant because it first introduced and then amplified anisotropy in the seed crystal by targeting the twinned surface, and exploited the twinning to yield $AuCu_3$ nanorods.
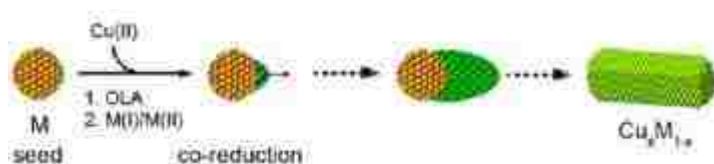
Figure 9: Seed mediated co-reduction process to produce Cu_xM_{1-x} nanorods through anisotropic growth of Cu and Au. (Reproduced by permission from reference 40. Copyright © 2013 American Chemical Society.)

The seeded co-reduction takes advantage of the fact that the energetic barrier to add atoms onto a crystal surface is typically much lower than the energy barrier to homogeneous nucleation of atoms to form crystal seeds. This effect can be exploited to produce a variety of nanostructures from a single reaction mixture, as shown in **Figure 10**.[41] As a demonstration of the effect that reaction rate has on the shapes produced through seeded co-reduction methods, Pd tipped octapods were produced when Au and Pd were reduced simultaneously at a fast rate; the shape was produced by the competition for crystal growth between the two metals. When the reduction was slowed, the shape was thermodynamically driven, rather than kinetically driven, and the final shape acted to minimize the surface energy of the particle by forming an octahedron and maximizing the internal volume.
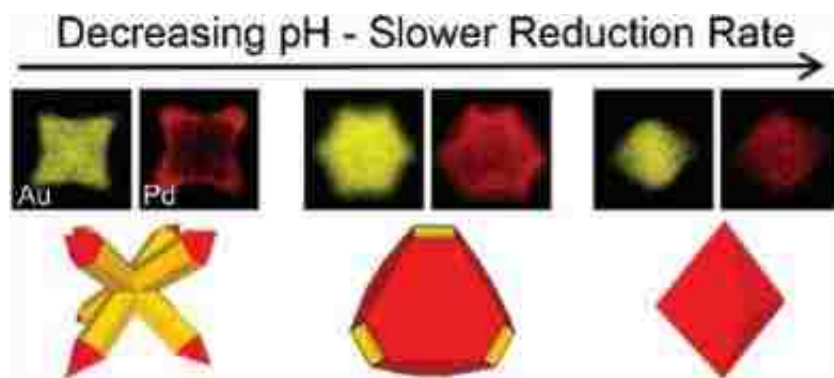
Figure 10: Au-Pd shape controlled alloyed nanostructures. (Reprinted by permission from reference 41. Copyright © 2012 American Chemical Society)

Silica can be introduced into nanostructures to physically protect the particles from aggregation and dramatically slow or even stop unwanted chemical reactions such as dissolution or oxidation. Silica, SiO_2, has been incorporated into nanostructures to improve the colloidal stability and chemically protect the inner metallic or semiconductor core. SiO_2 and similar materials, such as TiO_2, serve as a protective barrier against agglomeration and Ostwald ripening of the core particles, acting as solid barrier around the particle in place of surfactants. The silica itself is can be stabilized as a suspension via electrostatic repulsion between the silica shells.[42] The shells also chemically protect the cores, by slowing the diffusion of oxidants to the core in the case of porous SiO_2, or completely preventing interaction with the solution when the SiO_2 is dense enough. SiO_2 shells have successfully been employed into core-shell structures using quantum dots[43], and transition metal oxides such as Fe_3O_4[44], as well Au, and Ag metals[45], although the other metal exhibiting visible LSPR, Cu, has had significant challenges

16

incorporating into silica due to the reactivity of the Cu and the susceptibility to oxidize in aqueous conditions. For this reason, nano sized Cu LSPR effects have garnered very little study.

1.1.3.3 Total Synthesis of Nanostructures
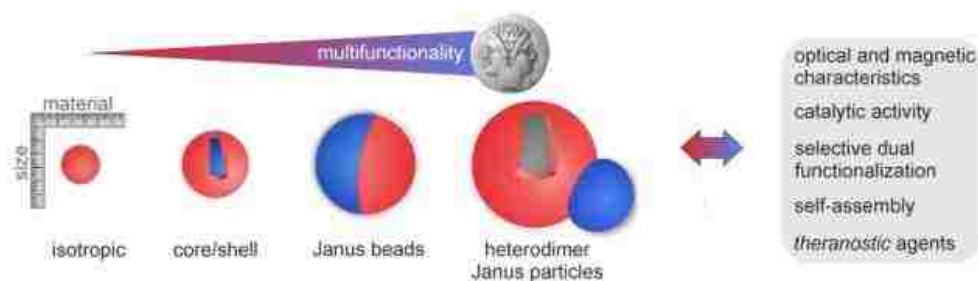
Figure 11: Illustration of the increasing complexity and multifunctionality of nanostructures as primitive isotropic structures are compared with core-shell, Janus particles, and heterodimer Janus particles.   (Reproduced by permission from Reference 46. Copyright © 2014 Beilstein-Institut)

Janus nanoparticles, also referred to as 'two-faced' particles, are of special interest due to their multifunctionality, as well as the synthetic challenge of producing two or more distinct surfaces on a single nanoparticle. As shown in **Figure 11**, Janus nanoparticles can combine two surfaces and/or materials into a single particle such as plasmonic activity and magnetism, catalytic activity and self-assembly, etc.[46] Anisotropic nanostructures such as Janus particles and related heteronanostructures allow for an opportunity to design the rational and sequential synthesis of increasingly complex nanostructures with applications in a wide range of fields.[48] This approach can be compared to the approach taken in organic synthesis, where "text book reactions" such as oxidation, addition, substitution, condensation, and ring opening exist as chemical tools because of their dependability and ubiquity.[47] These reactions are derived from

the predictable reactivities of molecules and functional groups and are studied and catalogued, providing a roadmap to produce natural products or new materials. As shown in **Figure 12**, parallel to the conventional chemical strategies such as utilizing protecting groups, chemoselectivity, and separation techniques, a corresponding nanostructure strategy can be employed. For example, in protein sequencing, c-terminal amino acids are protected and de-protected to produce the desired protein structure; in colloidal total synthesis, epitaxial growth of metals can be used to direct heterogeneous nucleation onto a metal, Ag onto Au for example, rather than onto an oxide surface.
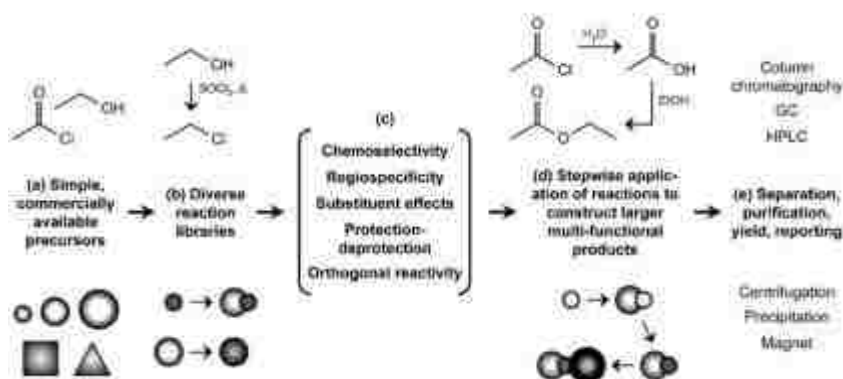
Figure 12: Comparison of traditional stepwise chemical synthesis to the analogous heteronanostructures stepwise approaches. (Reproduced by permission from reference 47. Copyright © 2013 WILEY-VCH Verlag GmbH & Co. KGaA, Weinheim.)

1.2 Multifunctional Applications

1.2.1 Catalytic Applications

Combining the high surface area of nanoparticles with the enhanced activity of alloyed metal-noble metal nanostructures makes the shape controlled synthesis of alloyed metals, especially the seeded co-reduction approach, a significant area of study as heterogeneous catalysis.[49] The problem of CO poisoning serves as an illustration of how alloyed nanostructures can solve a critical engineering problem. The use of platinum nanoparticles as catalysts, as in a polymer exchange fuel cell for instance, suffer from decreased activity over time due to CO adsorption.[50] Elimination of CO is also a concern as a common intermediate in direct alcohol fuel cells, and is produced at the anode of a fuel cell can cross over to the cathode and deactivates the Pt catalyst used in the oxygen reduction reaction (ORR). Modification of the metal electronic d-band, through allowing with transition metals(TM) and through TM-N and TM-P bonds leads to a lowering of catalyst surface poisoning by intermediates.[51] Although some ambiguity in the literature exists, the electrochemical community has accepted the "bi-functional mechanism" to rationalize the effect a second element imparts on Pt based catalytic surfaces.[52] As proposed by Watanabe and Motoo, the two metals together exhibit a combined catalytic activity greater than either one of the metals alone.[53] This bi-functional mechanism is depicted below in equations 2 and 3, and schematically in **Figure 13**.

$$Ru+H_2O \rightarrow Ru(OH)_{ads}+H^+e^- \quad\quad\quad (2)$$

$$Pt(CO)_{ads}+Ru(OH)_{ads} \rightarrow CO_2+Pt+Ru+H^++e^- \quad\quad (3)$$
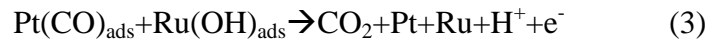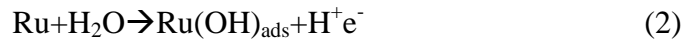
Although the deactivation of Pd is less will understood than Pt as the exact poisoning mechanisms are not characterized, alloying has still shown to increase activity.[54] A general strategy to alloy the primary metal to maximize the effects of the bi-functional mechanism is to

choose an oxophilic secondary metal that readily forms a bond with the unwanted intermediate, such as $(OH)_{ads}$ for Pt, preferentially compared to the primary metal. The second mechanism, which can arise from alloying as well as metallic layering, e.g. core-shell structures, is the modification in the electronic character of the primary catalyst (Pt, Pd, etc.). When the Pt or Pd is grown over or alloyed with a second metal, the electronic properties of the metal d-orbital change, reducing the interaction strength of reaction intermediates. In the case of CO and Pt, the synergistic interaction responsible for poisoning between the *5d-2π** orbitals between the metal and CO becomes weaker when Pt d bands energy is altered. Much of Pd loss of activity is believed to be from loss agglomeration of the particles together and dissolution of the metal into solution, especially in acidic solutions, during use.[55] Alloying of the Pd particles has shown some evidence of resisting this effect. Thus alloying of metals provides an additional synthetic handle to improve catalytic activity of traditionally catalytic metals.

1.2.2 Magnetic Nanoparticles
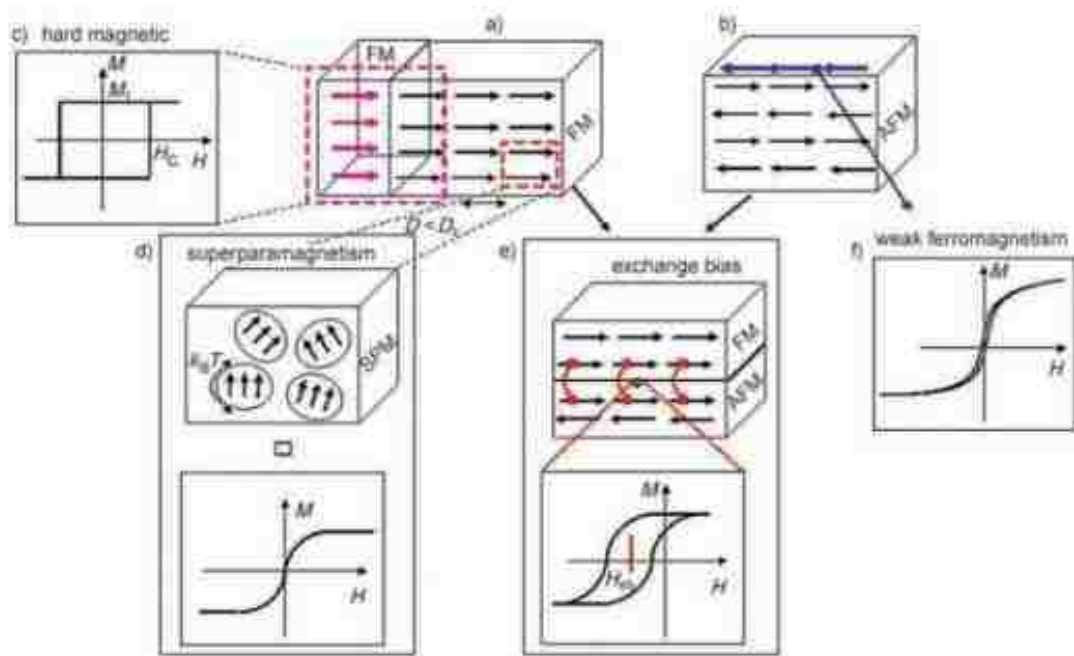
Figure 13: The different magnetic effects occurring in magnetic nanoparticles. (a) a ferromagnet (b) antiferromagnet, D is the diameter, D_c is the critical diameter. (c) hard magnet. (d) supermagnetic material. (e) an exchange bias effect when a ferromagnet is interfaces an anfiferromagnet. (f) weak ferromagnetism arising from uncompensated surface spins. (Reproduced From Reference 56. Copyright © 2007 WILEY-VCH Verlag GmbH & Co. KGaA, Weinheim)

As described above, the properties of nanoparticles are often quite distinct from the bulk material's characteristics. In addition to chemical reactivity and optical activity, the magnetic behavior of ferromagnetic materials changes when the size of the nanoparticle is equal to the magnetic domain size, typically 10-20nm.[56] When this condition is met, the material is said to be superparamagnetic, meaning that the particles exhibit no remanence or coercivity, or that there is a lack of hysteresis in a magnetization curve, as shown in **Figure 13** (d). This is a

desirable and necessary quality for magnetic nanoparticles as a colloid of permanent magnets will be unable to resist magnetically driven aggregation that would render them incompatible with biological systems.[57] The superparamagnetic nanoparticles however can behave as an ideal colloidal suspension, while also exhibiting strong magnetic susceptibility, allowing them to be used as designed for magnetic imaging techniques.[58] Combining the superparamagnetism of nanoscale magnetite, Fe_3O_4, with the tunable LSPR of noble metal nanostructures is of great interest as a synthetic challenge and for biomedical and theranostic applications.

1.2.3 Theranostic Applications

Many nanostructures, such as the hollow gold nanocage, have been adapted for use in both diagnosis and treatment of cancer. The ability of LSPR active nanoparticles to absorb light at the tissue transparent NIR window, as well as their high extinction cross section which is often as much as five times greater than conventional organic dyes[59] , have made such structures an active area of research in biomedicine. As depicted in **Figure 14**, theranostic nanostructures offer multiple functions, such as photo acoustic imaging, drug delivery, and cancer diagnosis.[58,59] These therapies benefit from dynamic and multiplexed nanoscale platforms, and are a primary driver behind the demand for complex anisotropic and multifunctional nanostructures. The primary challenge however, is in the process of combining properties into a single particle, maintaining the desired properties such as maximum LSPR absorption, shape of nanostructure, surface chemistry, or magnetic character. New synthetic tools are desired, as improving the ability to produce progressively complex heteronanostructures will improve their multifunctional utility.
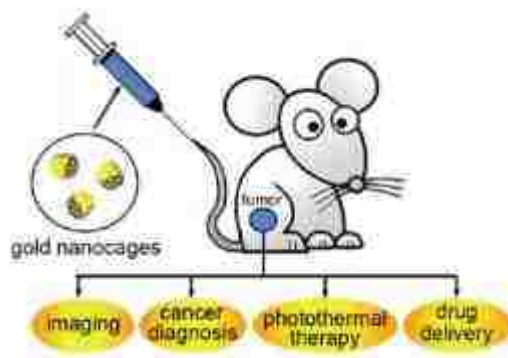
Figure 14: Illustration of multifunctional nanostructures for theranostics. (Reproduced by permission from reference 59. Copyright © 2011 American Chemical Society)

1.3 Objectives

Metal and metal hybrid nanostructures offer exciting prospects for spectroscopy, catalysis, and biology, among other applications. Wet chemical techniques offer a convenient and scalable route to producing nanoparticles; introducing fine control of materials on the nanoscale using these techniques is an active area with many pay offs for further improvement. In the following chapters, facile techniques for producing segmented nanostructures, novel $Cu-SiO_2$ structures, and metal core-metal oxide shell hybrid nanostructures are reported.

The following chapters are organized according to previously published articles or as soon to be published. **Chapter 2** encompasses the mask assisted seeded growth (MASG) of noble metal nanostructures to rapidly and easily produce segmented heteronanostructures. **Chapter 3** is focused on progress towards oxidation resistant Cu nanostructures stabilized with thin silica shells in water. **Chapter 4** includes a general approach to coat preformed metal nanostructures with transition metal oxides, and investigates their optical properties resulting from the procedure and the metal oxide shell. This strategy can be used to produce plasmonically active nanorods with superparamagnetic character. **Chapter 5** serves as a conclusion.

REFERENCES

(1)   O'Brien, S.; Brus, L.; Murray, C. B. Synthesis of Monodisperse Nanoparticles of Barium Titanate: Toward a Generalized Strategy of Oxide Nanoparticle Synthesis. *Journal of the American Chemical Society* **2001**, *123*, 12085.

(2)   Hochella Jr, M. F. There's plenty of room at the bottom: nanoscience in geochemistry. *Geochimica et Cosmochimica Acta* **2002**, *66*, 735.

(3)   Whitesides, G. M. The 'right' size in nanobiotechnology. *Nat Biotech* **2003**, *21*, 1161.

(4)   Kwok, S.; Zhang, Y. Mixed aromatic–aliphatic organic nanoparticles as carriers of unidentified infrared emission features. *Nature* **2011**, *479*, 80.

(5)   Vukusic, P.; Sambles, J. R. Photonic structures in biology. *Nature* **2003**, *424*, 852.

(6)   *No Ordinary Genius: The Illustrated Richard Feynman*; Sykes, C., Ed.; Norton and Company, New York, 1994.

(7)   Song, W.-S.; Yang, H. Efficient White-Light-Emitting Diodes Fabricated from Highly Fluorescent Copper Indium Sulfide Core/Shell Quantum Dots *Chemistry of Materials* **2012**, *24*, 1961.

(8)   Shi, L.; De Paoli, V.; Rosenzweig, N.; Rosenzweig, Z. Synthesis and Application of Quantum Dots FRET-Based Protease Sensors .*Journal of the American Chemical Society* **2006**, *128*, 10378.

(9)   Kenichi, I.; Yoshihiro, S.; Yoshiaki, N.; Shunichi, M.; Naoki, Y. New Optical Memory Structure Using Self-Assembled InAs Quantum Dots. *Japanese Journal of Applied Physics* **1995**, *34*, L1445.

(10)   Jain, P. K.; El-Sayed, I. H.; El-Sayed, M. A. Au nanoparticles target cancer. *Nano Today* **2007**, *2*, 18.

(11)   Nie, S.; Emory, S. R. Probing Single Molecules and Single Nanoparticles by Surface-Enhanced Raman Scattering. *Science* **1997**, *275*, 1102.

(12)   Resch-Genger, U.; Grabolle, M.; Cavaliere-Jaricot, S.; Nitschke, R.; Nann, T. Quantum dots versus organic dyes as fluorescent labels. *Nat Meth* **2008**, *5*, 763.

(13)   Sondi, I.; Salopek-Sondi, B. Silver nanoparticles as antimicrobial agent: a case study on E. coli as a model for Gram-negative bacteria. *Journal of Colloid and Interface Science* **2004**, *275*, 177.

(14)   Leyong, Z.; Di, W.; Ruifen, Z.; Tianxiang, C.; Jinchao, Z.; Aiguo, W. Paramagnetic and Superparamagnetic Inorganic Nanoparticles for T1-Weighted Magnetic Resonance Imaging. *Current Medicinal Chemistry* **2017**, *24*, 1.

(15)   Wilczewska, A. Z.; Niemirowicz, K.; Markiewicz, K. H.; Car, H. Nanoparticles as drug delivery systems. *Pharmacological Reports* **2012**, *64*, 1020.

(16)   Chen, S.; Zhao, X.; Chen, J.; Chen, J.; Kuznetsova, L.; Wong, S. S.; Ojima, I. Mechanism-Based Tumor-Targeting Drug Delivery System. Validation of Efficient Vitamin Receptor-Mediated Endocytosis and Drug Release. *Bioconjugate Chemistry* **2010**, *21*, 979.

(17)   Bell, A. T. The Impact of Nanoscience on Heterogeneous Catalysis. *Science* **2003**, *299*, 1688.

(18)   Gasteiger, H. A.; Kocha, S. S.; Sompalli, B.; Wagner, F. T. Activity benchmarks and requirements for Pt, Pt-alloy, and non-Pt oxygen reduction catalysts for PEMFCs. *Applied Catalysis B: Environmental* **2005**, *56*, 9.

(19)   Crabtree, G. W.; Sarrao, J. L. Opportunities for mesoscale science. *MRS Bulletin* **2012**, *37*, 1079.

(20)   Murphy, C. J.; Gole, A. M.; Hunyadi, S. E.; Stone, J. W.; Sisco, P. N.; Alkilany, A.; Kinard, B. E.; Hankins, P. Chemical sensing and imaging with metallic nanorods. *Chemical Communications* **2008**, 544.

(21)   Kelly, K. L.; Coronado, E.; Zhao, L. L.; Schatz, G. C. The Optical Properties of Metal Nanoparticles: The Influence of Size, Shape, and Dielectric Environment. *The Journal of Physical Chemistry B* **2003**, *107*, 668.

(22)   Lisiecki, I.; Billoudet, F.; Pileni, M. P. Control of the Shape and the Size of   Copper Metallic Particles. *The Journal of Physical Chemistry* **1996**, *100*, 4160.

(23)   Chan, G. H.; Zhao, J.; Hicks, E. M.; Schatz, G. C.; Van Duyne, R. P. Plasmonic Properties of Copper Nanoparticles Fabricated by Nanosphere Lithography. *Nano Letters* **2007**, *7*, 1947.

(24)   Jain, P. K.; Lee, K. S.; El-Sayed, I. H.; El-Sayed, M. A. Calculated Absorption and Scattering Properties of Gold Nanoparticles of Different Size, Shape, and Composition: Applications in Biological Imaging and Biomedicine. *The Journal of Physical Chemistry B* **2006**, *110*, 7238.

(25)   Wiley, B. J.; Im, S. H.; Li, Z.-Y.; McLellan, J.; Siekkinen, A.; Xia, Y. Maneuvering the Surface Plasmon Resonance of Silver Nanostructures through Shape-Controlled Synthesis. *The Journal of Physical Chemistry B* **2006**, *110*, 15666.

(26)   Tong, L.; Wei, Q.; Wei, A.; Cheng, J.-X. Gold Nanorods as Contrast Agents for Biological Imaging: Optical Properties, Surface Conjugation and Photothermal Effects. *Photochemistry and Photobiology* **2009**, *85*, 21.

(27)   Grand, J.; de la Chapelle, M. L.; Bijeon, J. L.; Adam, P. M.; Vial, A.; Royer, P. Role of localized surface plasmons in surface-enhanced Raman scattering of shape-controlled metallic particles in regular arrays. *Physical Review B* **2005**, *72*, 033407.

(28)   Cheng, J. Y.; Ross, C. A.; Smith, H. I.; Thomas, E. L. Templated Self-Assembly of Block Copolymers: Top-Down Helps Bottom-Up. *Advanced Materials* **2006**, *18*, 2505.

(29)   Li, S.; Yan, W.; Zhang, W.-x. *Green Chemistry* **2009**, *11*, 1618.

(30)   Murray C. B.; Kagan C. R.; Bawendi M. G. Synthesis and Characterization of Monodisperse Nanocrystals and Close-Packed Nanocrystal Assemblies. *Annual Review of Materials Science*, **2000**, *30,* 545.

(31)   Shevchenko, E. V.; Talapin, D. V.; Kotov, N. A.; O'Brien, S.; Murray, C. B. Structural diversity in binary nanoparticle superlattices. *Nature* **2006**, *439*, 55.

(32)   Laaksonen, A.; Hamed, A.; Joutsensaari, J.; Hiltunen, L.; Cavalli, F.; Junkermann, W.; Asmi, A.; Fuzzi, S.; Facchini, M. C. Cloud condensation nucleus production from nucleation events at a highly polluted region. *Geophysical Research Letters* **2005**, *32*, n/a.

(33)   Fievet, F.; Lagier, J. P.; Blin, B.; Beaudoin, B.; Figlarz, M. Homogeneous and heterogeneous nucleations in the polyol process for the preparation of micron and submicron size metal particles. *Solid State Ionics* **1989**, *32*, 198.

(34)   Weiner, R. G.; Skrabalak, S. E. Seed-Mediated Co-reduction as a Route To Shape-Controlled Trimetallic Nanocrystals. *Chemistry of Materials* **2016**, *28*, 4139.

(35)   Lim, B.; Jiang, M.; Tao, J.; Camargo, P. H. C.; Zhu, Y.; Xia, Y. Shape-Controlled Synthesis of Pd Nanocrystals in Aqueous Solutions. *Advanced Functional Materials* **2009**, *19*, 189.

(36)   Pileni, M. P. Control of the Size and Shape of Inorganic Nanocrystals at Various Scales from Nano to Macrodomains. *The Journal of Physical Chemistry C* **2007**, *111*, 9019.

(37)   Wiley, B. J.; Xiong, Y.; Li, Z.-Y.; Yin, Y.; Xia, Y. Right Bipyramids of Silver: A New Shape Derived from Single Twinned Seeds. *Nano Letters* **2006**, *6*, 765.

(38)   Xia, Y.; Xiong, Y.; Lim, B.; Skrabalak, S. E. hape-Controlled Synthesis of Metal Nanocrystals: Simple Chemistry Meets Complex Physics?. *Angewandte Chemie International Edition* **2009**, *48*, 60.

(39)   Elechiguerra, J. L.; Reyes-Gasga, J.; Yacaman, M. J. The role of twinning in shape evolution of anisotropic noble metal nanostructures. *Journal of Materials Chemistry* **2006**, *16*, 3906.

(40)   Chen, S.; Jenkins, S. V.; Tao, J.; Zhu, Y.; Chen, J. Anisotropic Seeded Growth of Cu–M (M = Au, Pt, or Pd) Bimetallic Nanorods with Tunable Optical and Catalytic Properties. *The Journal of Physical Chemistry C* **2013**, *117*, 8924.

(41)   DeSantis, C. J.; Sue, A. C.; Bower, M. M.; Skrabalak, S. E. Seed-Mediated Co-reduction: A Versatile Route to Architecturally Controlled Bimetallic Nanostructures. *ACS Nano* **2012**, *6*, 2617.

(42)   Nel, A. E.; Madler, L.; Velegol, D.; Xia, T.; Hoek, E. M. V.; Somasundaran, P.; Klaessig, F.; Castranova, V.; Thompson, M. Understanding biophysicochemical interactions at the nano-bio interface. *Nat Mater* **2009**, *8*, 543.

(43)   Selvan, S. T.; Tan, T. T.; Ying, J. Y. Robust, Non-Cytotoxic, Silica-Coated CdSe Quantum Dots with Efficient Photoluminescence. *Advanced Materials* **2005**, *17*, 1620.

(44)   Deng, Y.; Qi, D.; Deng, C.; Zhang, X.; Zhao, D. Superparamagnetic High-Magnetization Microspheres with an Fe3O4@SiO2 Core and Perpendicularly Aligned Mesoporous SiO2 Shell for Removal of Microcystins. *Journal of the American Chemical Society* **2008**, *130*, 28.

(45)   Baida, H.; Billaud, P.; Marhaba, S.; Christofilos, D.; Cottancin, E.; Crut, A.; Lermé, J.; Maioli, P.; Pellarin, M.; Broyer, M.; Del Fatti, N.; Vallée, F.; Sánchez-Iglesias, A.; Pastoriza-Santos, I.; Liz-Marzán, L. M. Quantitative Determination of the Size Dependence of Surface Plasmon Resonance Damping in Single Ag@SiO2 Nanoparticles. *Nano Letters* **2009**, *9*, 3463.

(46)   Schick, I.; Lorenz, S.; Gehrig, D.; Tenzer, S.; Storck, W.; Fischer, K.; Strand, D.; Laquai, F.; Tremel, W. Inorganic Janus particles for biomedical applications. *Beilstein Journal of Nanotechnology* **2014**, *5*, 2346.

(47)   Buck, M. R.; Schaak, R. E. Emerging Strategies for the Total Synthesis of Inorganic Nanostructures. *Angewandte Chemie International Edition* **2013**, *52*, 6154.

(48)   Zheng, H.; Li, Y.; Liu, H.; Yin, X.; Li, Y. Construction of heterostructure materials toward functionality. *Chemical Society Reviews* **2011**, *40*, 4506.

(49)   Yan, J.-M.; Zhang, X.-B.; Akita, T.; Haruta, M.; Xu, Q. One-Step Seeding Growth of Magnetically Recyclable Au@Co Core−Shell Nanoparticles: Highly Efficient Catalyst for Hydrolytic Dehydrogenation of Ammonia Borane. *Journal of the American Chemical Society* **2010**, *132*, 5326.

(50)   Alayoglu, S.; Nilekar, A. U.; Mavrikakis, M.; Eichhorn, B. Ru-Pt core-shell nanoparticles for preferential oxidation of carbon monoxide in hydrogen. *Nat Mater* **2008**, *7*, 333.

(51)   Ferrando, R.; Jellinek, J.; Johnston, R. L. Nanoalloys: From Theory to Applications of Alloy Clusters and Nanoparticles. *Chemical Reviews* **2008**, *108*, 845.

(52)   Sunghyun Uhm; Lee, H. J.; Lee, a. J. Understanding underlying processes in formic acid fuel cells. *Physical Chemistry Chemical Physics* **2009**, *11*, 9326.

(53)   Watanabe, M.; Motoo, S. Electrocatalysis by ad-atoms: Part II. Enhancement of the oxidation of methanol on platinum by ruthenium ad-atoms. *Journal of Electroanalytical Chemistry and Interfacial Electrochemistry* **1975**, *60*, 267.

(54)   Babu, P. K.; Kim, H. S.; Chung, J. H.; Oldfield, E.; Wieckowski, A. Bonding and Motional Aspects of CO Adsorbed on the Surface of Pt Nanoparticles Decorated with Pd. *The Journal of Physical Chemistry B* **2004**, *108*, 20228.

(55)   Tang, L.; Han, B.; Persson, K.; Friesen, C.; He, T.; Sieradzki, K.; Ceder, G. Electrochemical Stability of Nanometer-Scale Pt Particles in Acidic Environments. *Journal of the American Chemical Society* **2009**, *132*, 596.

(56)   Lu, A.-H.; Salabas, E. L.; Schüth, F. Magnetic Nanoparticles: Synthesis, Protection, Functionalization, and Application. *Angewandte Chemie International Edition* **2007**, *46*, 1222.

(57)   Sun, C.; Lee, J. S. H.; Zhang, M. Magnetic nanoparticles in MR imaging and drug delivery *Advanced Drug Delivery Reviews* **2008**, *60*, 1252.

(58)   Kim, D. K.; Zhang, Y.; Voit, W.; Rao, K. V.; Muhammed, M. Synthesis and characterization of surfactant-coated superparamagnetic monodispersed iron oxide nanoparticles. *Journal of Magnetism and Magnetic Materials* **2001**, *225*, 30.

(59)   Xia, Y.; Li, W.; Cobley, C. M.; Chen, J.; Xia, X.; Zhang, Q.; Yang, M.; Cho, E. C.; Brown, P. K. Gold Nanocages: From Synthesis to Theranostic Applications. *Accounts of Chemical Research* **2011**, *44*, 914.

Chapter II. Mask-Assisted Seeded Growth of Segmented Metallic Heteronanostructures*

Abstract

Controlling the deposition of exotic metals in the seeded growth of multi-metal nanostructures is challenging. This work describes a seeded growth method assisted by a mask for synthesis of segmented binary or ternary metal nanostructures. Silica is used as a mask to partially block the surface of a seed and a second metal is subsequently deposited on the exposed area, forming a bimetallic heterodimer. The initial demonstration was carried out on a Au seed, followed by deposition of Pd or Pt on the seed. It was found that Pd tends to spread out laterally on the seed while Pt inclines to grow vertically into branched topology on Au. Without removal of the SiO_2 mask, Pt could be further deposited on the unblocked Pd of the Pd-Au dimer to form a Pt-Pd-Au trimer. The mask-assisted seeded growth provides a general strategy to construct segmented metallic nanoarchitectures.

Introduction

Heterostructures of two or more metals with interfaces at the nanoscale is of particular significance because they exhibit unique properties and multi-functions distinctly different from the individual components.[1-4] The diverse surface chemistry of these heteronanostructures enables new applications that are not possible with each component alone. For example, multi-segmented metal nanorods have been demonstrated for applications in synergistic heterogeneous catalysis,[5-6] self-electrophoretic nanomotors/ nanobatteries,[7-8] multifunctional biomedicine,[9-10] and multiplexed detections.[11-12] To fabricate the heteronanostructures, sequential electrochemical deposition of metal ions into templates is the most common method since the 1990s.[13-14] In this approach, commercially-available alumina or polycarbonate membranes with uniform pores are often used as templates, yielding segmented metal rods.[15] This method could be further extended to selective growth of additional metals within the templates in solution after the initial electrochemical deposition of rod-shaped seeds.[16-17] To generate heterostructures with other configurations, it is usually required to involve cost-intensive and time-consuming lithography techniques.[18] In this work, a site-selective seeded growth method, termed mask-assisted seeded growth (MASG), is developed to expand the library of metal heterostructures with complex nanoarchitectures.

Seeded growth has emerged as a compelling method to create a wide variety of novel metal nanostructures.[19-24] Conditions that yield heteronanostructures depend on a number of factors such as the structural characteristics of constituent components, the reduction kinetics of metal precursors, and the capping agents. For example, a high degree of lattice mismatch between the seed and the second metal prevents conformal growth of core@shell structures and yields heteronanostructures of Au on $CoPt_3$,[25] Au rods on Pt cubes,[21] and Cu on Au.[24] Controlling the

reduction kinetics can selectively direct the nucleation and subsequent growth of the second metal on the seed to form dimers of Au on Pd[26] or other non-conformal structures such as Ag/Au on Pd cubes[27-28] and Ag on Au nanorods.[29] On the other hand, blocking specific facets of the seeds by capping agents could lead to the growth of Rh on Pd heterostructures.[30] Despite these advances, optimization of the growth conditions is largely material specific and it is beneficial to develop a general approach for the synthesis of multi-component heteronanostructures.

In this work, the MASG method uses SiO_2 as a mask in seeded growth to partially block the surface of the seed and thus direct the deposition of exotic metals on the exposed surface of the seed, forming heteronanostructures. The asymmetric coating of SiO_2 was demonstrated in the classical Stöber synthesis by using a polymeric ligand to partially block the diffusion of the sol-gel precursor to reach the surface of the nanoparticle.[31] However, this method is only suitable for water-soluble nanoparticles. To overcome this limitation, the water-in-oil (W/O) microemulsion method is used to form the SiO_2 mask. Unlike the classical Stöber synthesis of SiO_2 coating,[31-34] the W/O microemulsion confines the sol-gel condensation within the water droplets in bulk oil, particularly useful for the formation of SiO_2 coating on nanoparticles suspended in hydrophobic solvents.[35] By reducing the concentration of sol-gel precursor in the W/O microemulsion, phase separation between the surface ligand and hydrolyzed precursor is created on the particle surface, leading to partial condensation of SiO_2 on individual Au nanospheres to yield Au-SiO_2 dumbbell structures. Sequential reduction of Pd and Pt precursors on these dumbbell structures generates heterodimers of Pd-Au and Pt-Au, and more complex Pt-Pd-Au heterotrimmers. The reaction mechanisms of the microemulsion for preparation of Au-SiO_2 dumbbells and their subsequent use for synthesis of heteronanostructures are elucidated. These heteronanostructures exhibit tunable optical properties in the visible markedly different from the individual components.

Methods

Chemicals. Hydrogen tetrachloroaurate trihydrate ($HAuCl_4 \cdot 3H_2O$, 99.99%), potassium tetrachloroplatinate (K_2PtCl_4, 99.9%), potassium tetrachloropalladate (K_2PdCl_4, 99.9%), and ammonium hydroxide (28-30% $NH_3 \cdot H_2O$) were purchased from Alfa Aesar. Tetradecylamine (TDA, >95%) was purchased from TCI. Tetraethoxysilane (TEOS, 98%), poly(oxyethylene) nonylphenyl ether (Igepal CO-520), and polyvinylpyrrolidone (PVP, M.W. = 55,000) were purchased from Sigma-Aldrich. Cyclohexane (ACS grade) was purchased from EMD. All chemicals were used as received unless specified otherwise.

Synthesis of Au-SiO$_2$ Dumbbells. The Au-SiO$_2$ dumbbells were synthesized by controlling the hydrolysis and condensation of the SiO$_2$ precursor during the coating process using W/O microemulsions. Initially, 10-nm Au nanoparticles were prepared by reducing $HAuCl_4 \cdot 3H_2O$ (19.7 mg, 0.05 mmol) in 5 g of TDA at 160 $^{\circ}$C for 20 min under argon. After the reaction, the product was cooled to 100 $^{\circ}$C and purified with toluene and ethanol to remove unreacted precursor and excess TDA. The Au nanoparticles were then dispersed in cyclohexane for silica coating in W/O microemulsions. In a typical procedure, 1 mL of 200 nM Au nanoparticles was added to the mixture of 0.14 M Igepal CO-520 in 40 mL cyclohexane in a round-bottom flask equipped with a magnetic stirring bar. Various amounts of TEOS (20-200 mL) were added to the reaction mixture and allowed to mix for 30 min before the addition of 0.280 mL of $NH_3 \cdot H_2O$. The Au-SiO$_2$ dumbbell structures were formed when less than 50 mL of TEOS was used. The reaction was allowed to proceed for 48 h and stopped by adding ethanol to interrupt the emulsion. The product was washed by ethanol and dispersed in 18 MΩ H$_2$O for future use.

Synthesis of Pd-Au Dimers. The Pd-Au dimers were synthesized by reducing the Pd precursor in the presence of Au-SiO$_2$ dumbbells using ascorbic acid. In a typical procedure, 8

mL of K_2PdCl_4 was added, at a rate of 0.1 mL/min, to a 5 ml aqueous solution containing Au-SiO_2 dumbbells (~15 pmol) and PVP (1 mg/mL) at room temperature. Final concentrations of K_2PdCl_4 (0.06, 0.2, and 0.35 mM) in the reactions were used to yield Pd depositions with different thickness of ~4, ~7, and ~10 nm, respectively. The molar ratio of ascorbic acid to K_2PdCl_4 was kept at 10 to 1 for all three reactions. The product was washed by ethanol and dispersed in 18 MΩ H_2O. The SiO_2 component was then dissolved by mixing the Pd-Au-SiO_2 particles overnight in an aqueous solution containing excess NaOH and PVP (10 mg/mL). The product was washed with water and dispersed in 18 MΩ H_2O.

The thickness (x_{Pd}) of Pd deposition was estimated using a crude model which approximates the Pd layer is a semi-spherical shell interfacing with a spherical Au core. The radius of the semi-shell (r_{Pd}) can be derived from the average volume of Pd (nm^3 per particle):

$$V_{Pd} = \frac{1}{2}\left(\frac{4}{3}\pi r_{Pd}^3 - \frac{4}{3}\pi r_{Au}^3\right),$$ where r_{Au} is the radius of the Au core that can be measured from the

transmission electron microscopy (TEM) image. The V_{Pd} was obtained from $\frac{V_{Pd}}{V_{Au}} = \frac{C_{Pd}a_{Pd}^3}{C_{Au}a_{Au}^3}$,

where V_{Au} is the average volume of Au (nm^3 per particle) assuming spherical shape ($V_{Au} = \frac{4}{3}\pi r_{Au}^3$

); C_{Pd} and C_{Au} are the concentration of Pd and Au (mol/L), respectively, which can be measured from the bulk sample; a_{Pd} and a_{Au} are the lattice constant of Pd and Au (nm), respectively. The difference of the r_{Pd} and r_{Au} gives the thickness of the Pd semi-shell: $x_{Pd} = r_{Pd} - r_{Au}$.

Synthesis of Pt-Au Dimers. The procedure for Pt-Au dimers was the same as that for Pd-Au dimers described above, with the exception that K_2PtCl_4 was used as the Pt precursor and final concentration of Pt in the reaction solution is 2.4mM.

Synthesis of Pt-Pd-Au Trimers. The Pt-Pd-Au trimmers were synthesized using a similar procedure as that for Pt-Au dimers except that the Au-SiO$_2$ was replaced by the pre-synthesized Pd-Au-SiO$_2$ described above.

RESULTS

The MASG method has been demonstrated to synthesize bimetallic and trimetallic heteronanostructures. **Figure 1A** illustrates the general strategy of the MASG method using a Au seed and a second metal Pd as an example to create heterodimers. This method involves SiO$_2$ to mask one side of a spherical nanoparticle and expose the other side for deposition of successive metals. After deposition, the SiO$_2$ mask can be removed to yield heterodimers, trimers, or oligomers depending on the number of repeating depositions performed during the seeded growth. As an initial demonstration, Au and Pd were used as the seed and the second metal, respectively. The Au seeds prepared by reducing chloroauric acid in tetradecylamine were spherical nanoparticles with diameter of 9.7±1.3 nm (**Fig. 1B**). High resolution TEM (HRTEM) analysis shows that the Au seeds adopted decahedral geometry consisting of five tetrahedral subunits (**Fig. S1**). The subunits were bounded by {111} crystal faces, arranging along a five-fold rotation axis along the [110] zone.[36] Silica was subsequently condensed on these seeds using a modified W/O microemulsion method to form Au-SiO$_2$ dumbbells (**Fig. 1C**). The yield of dumbbells was close to 90% with half of the seed surface covered by SiO$_2$. These SiO$_2$-masked seeds were used for the deposition of Pd. Upon reducing Pd precursors with ascorbic acid, Pd was selectively deposited on the unblocked Au surface of these dumbbells to generate heterostructures of Pd-Au-SiO$_2$ (**Fig. 1D**). Removal of the SiO$_2$ mask yielded Pd-Au heterodimers (**Fig. 1E**).
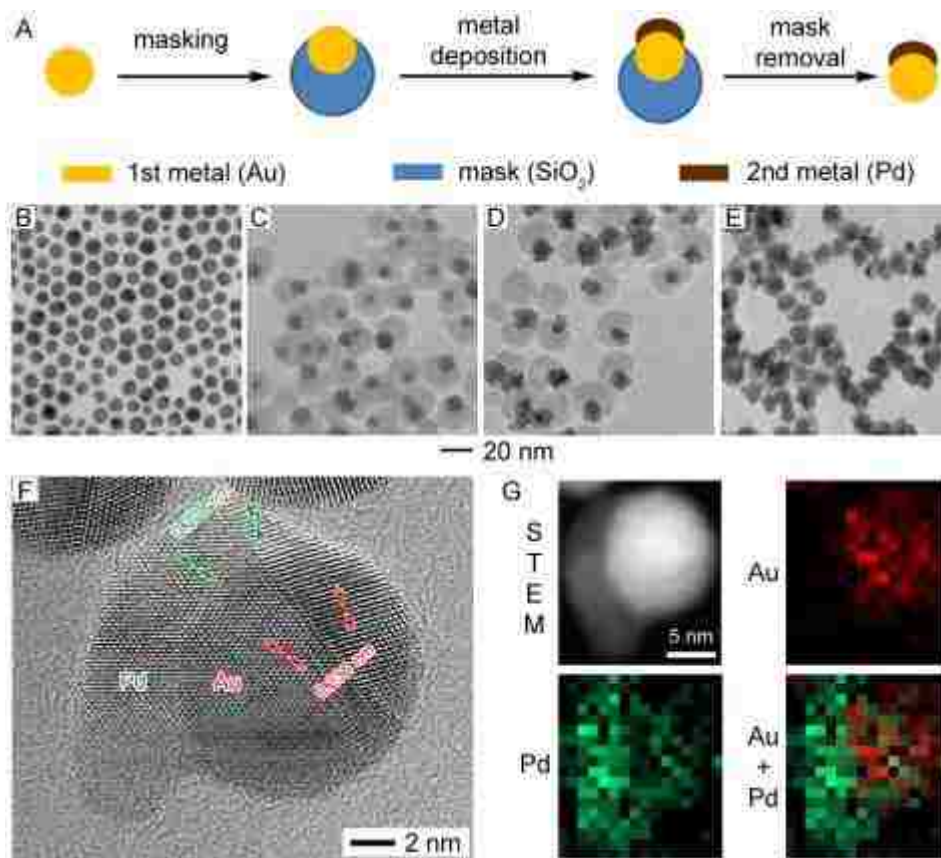
Figure 1. (A) Schematic illustration of the MASG method for synthesis of metallic heteronanostructures. TEM characterization of products from each step in the process using Pd-Au as a demonstration: (B) Au spherical nanoparticles with a mean diameter of 9.7±1.3 nm; (C) Au-SiO$_2$ dumbbell nanoparticles; (D) Pd-Au-SiO$_2$ nanoparticles; and (E) Pd-Au heterodimers. TEM characterization of an individual Pd-Au heterodimer: (F) HRTEM image and (G) HAADF-STEM image and EDX elemental mapping.

The Pd-Au dimers were further characterized by HRTEM, high angle annular dark field scanning transmission electron microscopy (HAADF-STEM), and energy-dispersive X-ray spectroscopy (EDX). The HRTEM image of individual Pd-Au dimers clearly shows that the two components were assembled into heterostructures (**Fig. 1F**). The Z-contrast HAADF-STEM image and EDX mapping indicate that the dimers adopted a mushroom configuration with a Au spherical stem and a Pd cap (**Fig. 1G**). Further analysis of the HRTEM image shows the continuation of lattice fringes from Au to Pd. The lattice spacing was measured to be 0.236 and 0.228 nm corresponding to the spacing of {111} planes of Au and Pd, respectively. This result suggests an epitaxial growth of Pd on the {111} facets of decahedral five-fold twinned Au nanoparticles, in agreed with the previous *in situ* TEM observations.[37] Without the SiO_2 mask, no Au-Pd dumbbells were found in the product under identical conditions (**Fig. S2**).

The growth of Pd on Au-SiO_2 dumbbells could be manipulated by varying the amount of Pd precursor introduced during the deposition onto the Au-SiO_2 seeds. The amount of Au-SiO_2 seeds was kept constant and the concentration of Au-SiO_2 was estimated using the extinction coefficient at 520 nm ($\varepsilon_{Au} = (1.55 \pm 0.01) \times 10^8\,M^{-1} \cdot cm^{-1}$, **Fig. S3**). To maintain the same reaction volume, different concentrations of K_2PdCl_4 were added to the reaction containing 15 *p*mol of Au-SiO_2 at a rate of 0.1 mL/min. Because the underpotential deposition of Pd on Au favors heterogeneous nucleation of Pd on Au over Pd on Pd,[38-39] Pd preferentially nucleates laterally on the Au surface to cover the entire area of the exposed Au prior to the growth on newly-deposited Pd. Increased concentration of K_2PdCl_4 from 0.06, to 0.20 and 0.35 mM resulted in thicker deposition of Pd, as shown in **Figure 2A**, **1D**, and **2B**, respectively. A crude model was established to calculate the deposition thickness of Pd by approximating the Pd layer as a semi-spherical shell interfacing with a spherical core of Au as described in the experimental

section. The deposition thickness of Pd was estimated to be 4, 7, 10 nm for the three samples, denoted as sPd-Au-SiO$_2$, mPd-Au-SiO$_2$, lPd-Au-SiO$_2$, respectively.

Careful control of the reduction rate of the second metal is important to ensure heterogeneous nucleation and subsequent growth. A mild reduction of Pd was maintained for the deposition of Pd on Au using ascorbic acid as a reducing agent. The correlation between the amount of Pd formed and the amount of Pd precursor added was plotted in **Figure 2C**. In this study, the amount of ascorbic acid was in excess, 10:1 equivalent to the Pd precursor. The amount of deposited Pd on Au was linearly proportional to the amount of Pd precursor added to the reaction in the range of molar ratios of Pd to Au less than 10. The slope of the linear fitting curve was 0.90±0.04, suggesting that nearly all the Pd precursor was reduced under these reaction conditions. The XRD results also show an increase of the Pd-to-Au ratio from sPd-Au-SiO$_2$, to mPd-Au-SiO$_2$ and lPd-Au-SiO$_2$ by comparing the ratio of (111) peaks of Pd to Au in **Figure 2D**. Diffusion between the two metals at the interface may occur,[40] however, the rate could be rather slow at room temperature.[41-42]
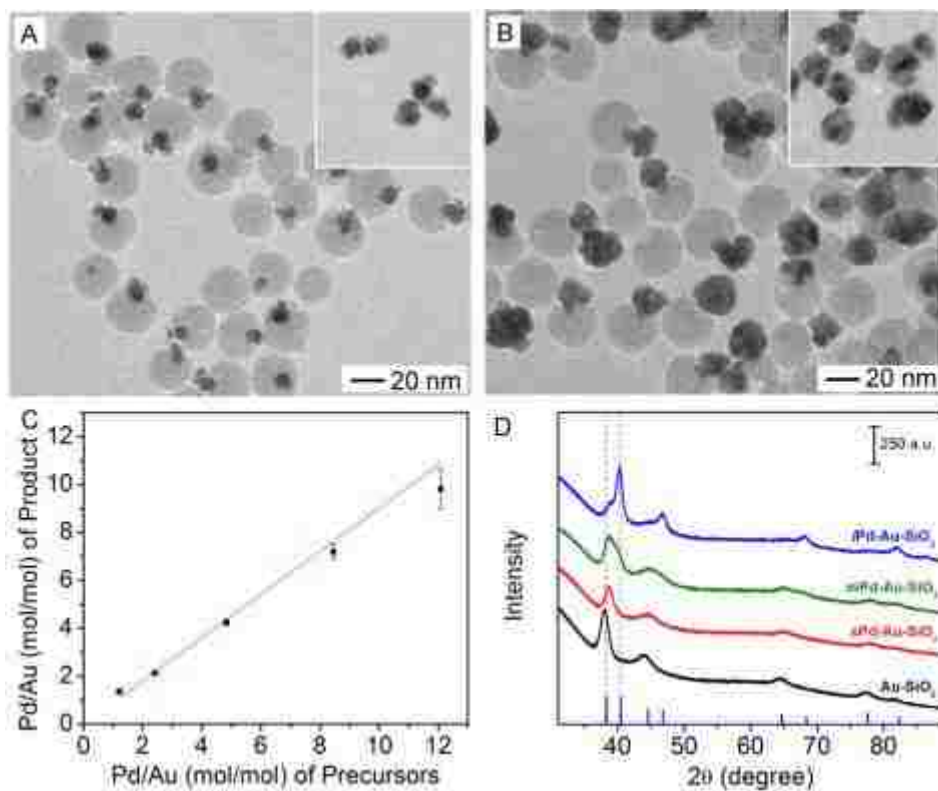
Figure 2. TEM characterization of Pd-Au-SiO$_2$ heteronanostructures with different thickness of Pd deposition: (A) 4; and (B) 10 nm. The insets show the corresponding TEM images of Pd-Au heterodimers after the removal of silica. (C) Plot of the relative quantities of Pd in the dimers versus that in the precursor. (D) XRD patterns of the Au-SiO$_2$ dumbbell nanoparticles (Au-SiO$_2$) and Pd-Au-SiO$_2$ heteronanostructures with Pd deposition thickness of 4, 7, and 10 nm, denoted as sPd-Au-SiO$_2$, mPd-Au-SiO$_2$, lPd-Au-SiO$_2$, respectively.

The deposition of Pd on Au could be monitored by the change of the optical properties of the resultant heteronanostructures. **Figure 3A** shows the UV-Vis spectra of *s*Pd-Au-SiO$_2$, *m*Pd-Au-SiO$_2$ and *l*Pd-Au-SiO$_2$. Due to the damping effects of Pd on the surface plasmon resonance of Au,[43] the extinction peak of Au nanoparticles at 520 nm was gradually flattened out as the deposition volume of Pd increased The optical spectra were further simulated using the discrete dipole approximation (DDA) method,[44] based on our crudely modelled geometry shown in the insets of **Figure 3, B-D**. Due to small size of the particles, light absorption dominated over scattering for their surface plasmon resonances. The simulated spectra matched well with the empirical extinction spectra, showing a decrease in extinction efficiency of Au at 520 nm after deposition of Pd, from 0.652 (**Fig. S4**) to 0.420 (**Fig. 3B**), by about one third. As the size of Pd increases from a x_{Pd} of 4 nm to 7 nm and 10 nm, the extinction efficiency at 520 nm slightly increases from 0.420, to 0.470 and 0.550, respectively. The corresponding extinction cross sections of individual dimers increase from 0.75×10^{-16}, to 1.40×10^{-16} and 2.50×10^{-16} m^2. The optical spectra of another possible model of the Au-Pd dimer containing the same amount of Au and Pd by volume were also calculated. In this second model, the Au sphere is covered by a partial ellipsoid, as shown in **Figure S5**. The calculated spectra of the second model are very similar to the semi-spherical Pd shell model, suggesting that the optical spectra of the Au-Pd dimer are insensitive to certain details of the configuration such as the flat cutoff of a half-shell versus the curvature of an ellipsoid. By observing the change in the spectral shapes and intensity at 520 nm, the colorimetric method provides a simple and convenient means to track the deposition thickness of Pd *in situ*.
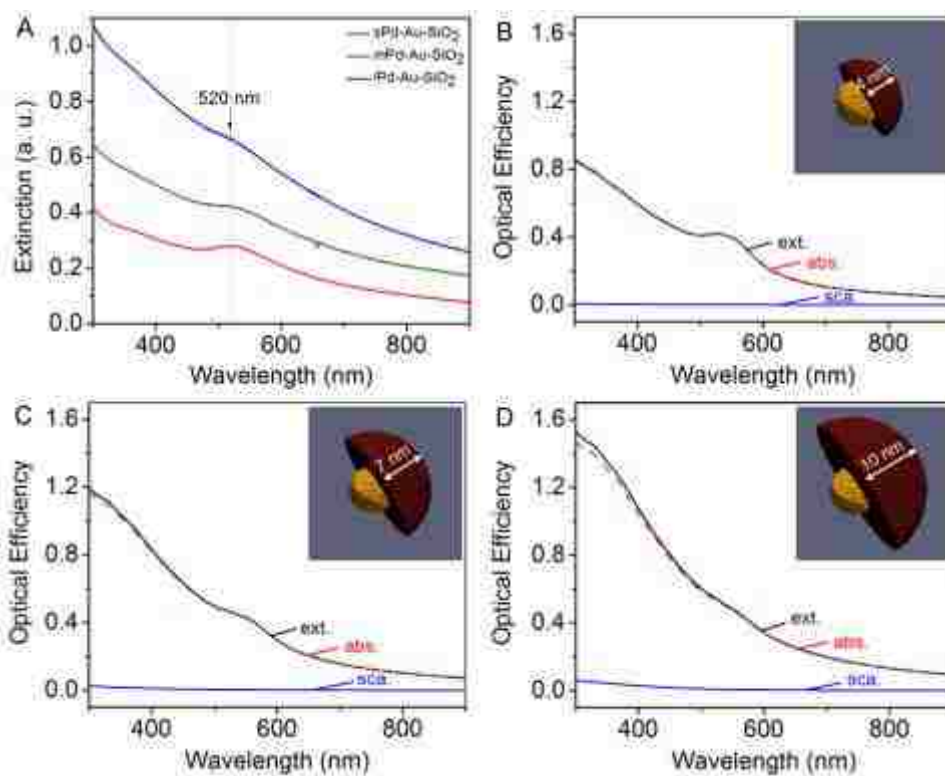
Figure 3. UV-Vis spectra of the Pd-Au-SiO$_2$ heteronanostructures with a Pd deposition thickness of 4, 7, and 10 nm on Au nanoparticles with a diameter of 9.7±1.3 nm, denoted as sPd-Au-SiO$_2$, mPd-Au-SiO$_2$, and lPd-Au-SiO$_2$, respectively. DDA simulation of the optical spectra of Pd-Au heterodimers with a Pd thick deposition of 4, 7, and 10 nm on a Au nanosphere with a diameter of 10 nm, denoted as sPd-Au (B), mPd-Au (C), lPd-Au (D), respectively. The insets show the geometries of the Pd-Au heterodimers used for the simulation.

To further evaluate the versatility of the MASG method, Pt was examined as a second metal for deposition on the Au-SiO$_2$ dumbbells. Interestingly, Pt was deposited on Au as a dendritic configuration branching out vertically as opposed to the lateral growth of Pd on Au (**Fig. 4**). Further analysis of HRTEM images shows the lattice spacing was measured to be 0.236 and 0.228 nm corresponding to the spacing of {111} planes of Au and Pt, respectively. It is suggested that Pt clusters could be deposited on Au seeds through either direct reduction or oriented attachment on the {111} facets of decahedral five-fold twinned Au nanoparticles.[45-46] After the initial epitaxial growth of Pt on Au, growth of Pt on Pt is more favorable than that on Au possibly due to the overpotential of Pt deposition on the Au surface. The slow reduction kinetics promotes the growth of Pt along the <111> direction into branched structures.[47] The HAADF-STEM image and EDX elemental mapping verified the composition of Au and Pt heterodimer structures.
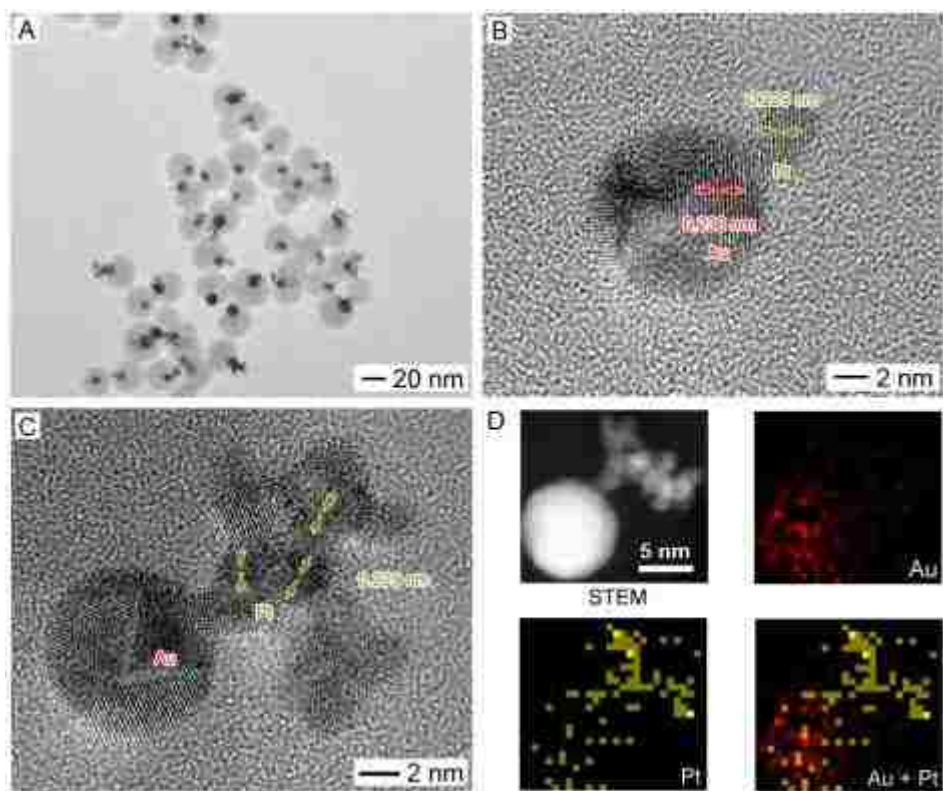
Figure 4. TEM characterization of Pt-Au-SiO$_2$ heterostructures: (A) overview image; (B, C) HRTEM of individual particles; and (D) HAADF-STEM image and EDX elemental mapping.

The MASG method can be further extended to grow an additional component at a designated site of the heterodimers using the SiO_2 masking strategy. As a demonstration, Pt was added with ascorbic acid to the suspension of Pd-Au-SiO_2 heterostructures with Au protected by the SiO_2 coating. Dendritic Pt caps were formed on the Pd side of the Pd-Au dimers as shown in **Figure 5**, in contrast to equal deposition on both Pd and Au, which was observed on the unprotected dimers (**Fig. S6**). It is hard to differentiate Pd and Pt by comparing the lattice spacing of {111} facets because their lattice constant are almost identical (0.389 nm for Pd versus 0.392 for Pt).[48] However, the vertical growth pattern of Pt is distinctly different from the lateral one of Pd. From the HRTEM analysis, it was found that epitaxial growth was extended from Pd on Au {111} faces to Pt on Pd {111} faces of Pd-Au. The composition of Au, Pd, and Pt of individual heterotrimers was further confirmed by the HAADF-STEM image and EDX elemental mapping.
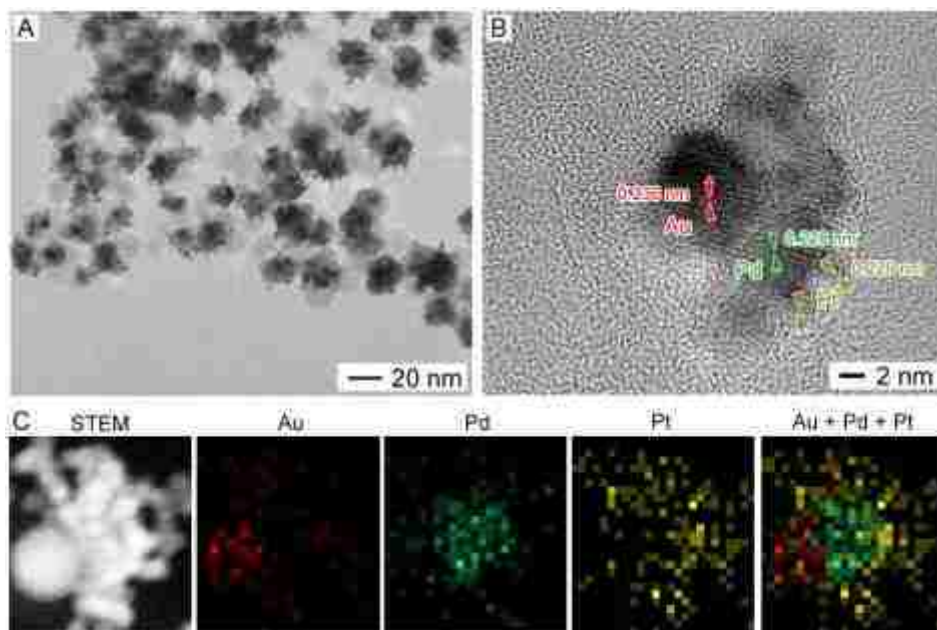
Figure 5. TEM characterization of Pt-Pd-Au-SiO$_2$ heteronanostructures: (A) overview image; (B) HRTEM of an individual particle; (C) HAADF-STEM image and EDX elemental mapping.

Discussion

The formation of metal-SiO$_2$ dumbbell nanoparticles is the key to the success of the MASG method. A high yield of Au-SiO$_2$ dumbbells was accomplished by a modified W/O microemulsion method. In a typical W/O microemulsion, the silica coating on a nanoparticle is formed by hydrolysis and condensation of TEOS within a micrometer- or nanometer-sized droplet that is generated in a homogeneous mixture of water, organic solvent (oil), and surfactant. The conventional method often results in core@shell structures with minimal inhomogeneity in the coating.[35] The modified W/O microemulsion was carried out by hydrolysis and condensation of TEOS on TDA-coated Au nanoparticles using ammonia in the presence of surfactant (Igepal CO-520) and organic solvent (cyclohexane). To increase the yield of Au-SiO$_2$ dumbbells, the concentration of TEOS was reduced to create phase separation between TDA and hydrolyzed TEOS on the surface of Au nanoparticles.
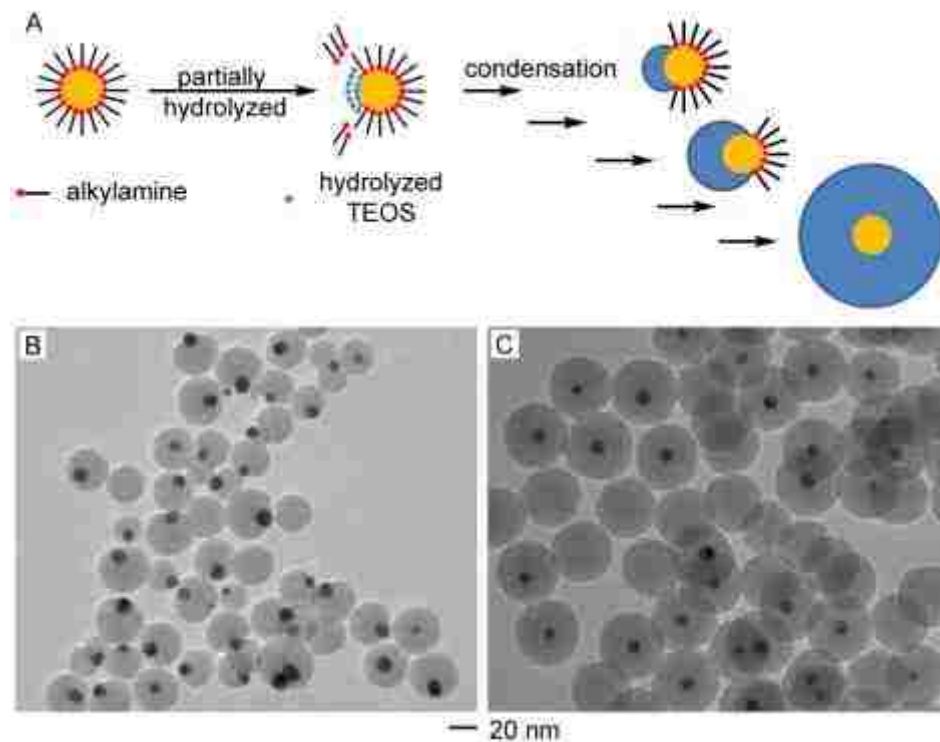
Figure 6. (A) Schematic illustration of the mechanism of silica coating via a micro-emulsion process. TEM characterization of the corresponding samples in the proposed mechanism using two different concentrations of TEOS under identical reaction conditions: (B) at low concentration (3.4 mM); and (C) at high concentration (22.4 mM).

The mechanism based on phase separation in the W/O microemulsion was illustrated in **Figure 6A**. Initially, TDA ligands on the nanoparticles were partially replaced by the hydrolyzed TEOS, resulting in phase segregation of hydrophobic oleylamine and hydrophilic TEOS.[49] Further condensation of TEOS was limited to the hydrophilic portion of the particle surface, yielding dumbbell structures of Au-SiO_2 (**Fig. 6B**). As the concentration of TEOS increases, more TDA ligands are substituted by the hydrolyzed TEOS, leading to a gradual expansion of TEOS to encompass the entire surface of the Au nanoparticles and thus further condensation to form complete SiO_2 shell (**Fig. 6C**). The resultant SiO_2 is porous, allowing small molecules to diffuse in and out more easily as compared to crystalline materials. For example, water can diffuse through the pores of SiO_2 to reach the surface of Au nanoparticles, resulting in a SiO_2 shell filled with water. Assuming that a simple mathematic average can be used to estimate the dielectric constant of a two-component mixture, the refractive index of porous SiO_2 surrounding Au nanoparticles can be shown to be very similar to that of toluene. This was confirmed by measuring the extinction spectra of Au nanoparticles in toluene and Au-SiO_2 in water. The spectra are very similar and consistent with our approximation (**Fig. S7**). Despite of its porous nature, the SiO_2 mask can act as a protecting group and effectively reduce the surface accessibility of reactant molecules in a chemical reaction. To verify the protecting function of SiO_2, the reactivity of Au in the dumbbells and the core@shell structures was compared using two model reactions: an etching experiment using excess KCN and the reduction of *p*-nitrophenol by excess $NaBH_4$.

The reactivity of the Au cores in the dumbbells is markedly different from that of core-shell structures because SiO_2 coating largely blocks the diffusion of reactants. The etching of Au involves the use of KCN in aqueous solution as follows: $4Au + 8CN^- + O_2 + 2H_2O \rightarrow$

$4[Au(CN)_2]^- + 4OH^-$. The rate of the reaction is mainly limited by the diffusion of CN^- through the pores of SiO_2 because the dissolved O_2 and water molecules have covered the surface of Au. As the size of Au nanoparticles decreases during the etching process, the extinction efficiency reduces linearly while cross-section decreases exponentially (**Fig. S6**). The dissolution of Au could then be monitored by the diminished rate of extinction at 520 nm (**Fig. 7A**). It was found that the etching rate of Au in the dumbbell particles was faster than that in the core@shell structures. In the case of core@shell structures, the etching rate was further slowed down after 10 min, possibly because the slower diffusion rate of the larger $[Au(CN)_2]^-$ anions further slows down the etching rate of Au. After dissolution of Au, the dumbbell particles yielded half shells of silica while complete silica shells were found as the product for core@shell particles (**Fig. 7, B and C**). The slight change of SiO_2 morphology after etching could be possibly due to the structure reconstruction in the basic solution during etching process.[50]
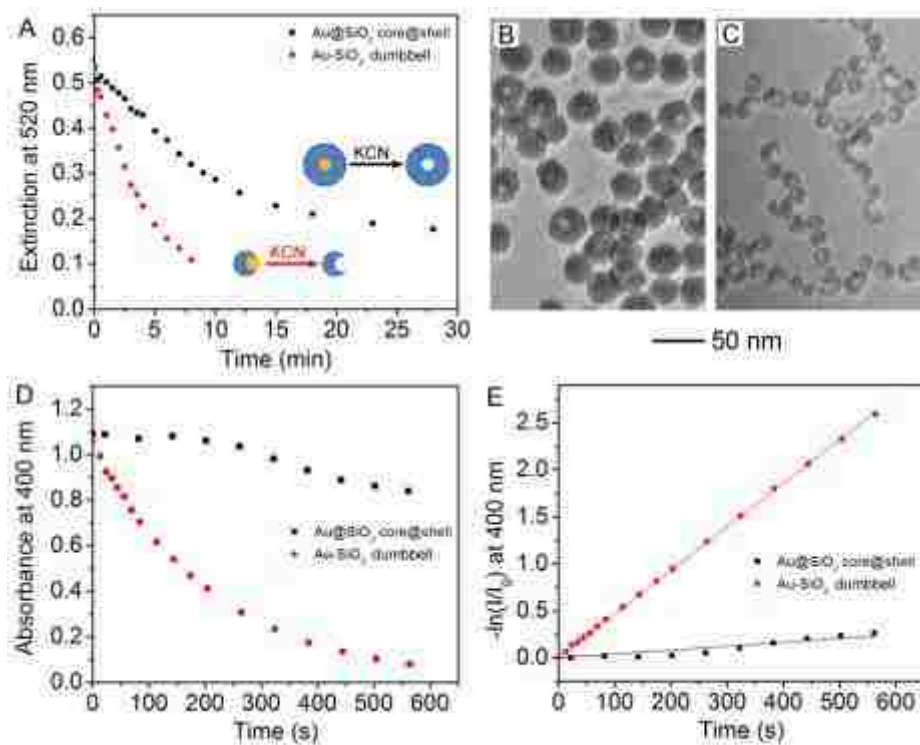
Figure 7. Etching process of Au nanoparticles: (A) Plot of extinction at 520 nm as a function of etching time; TEM images of Au@SiO$_2$ core@shell structures (B) and Au-SiO$_2$ dimers (C) after etching. Kinetic study of 4-nitrophenol reduction on Au-SiO$_2$ nanostructures: (D) plot of normalized absorbance (I/I$_0$) of p-nitrophenolate ion at 400 nm as a function of time for different catalysts; and (E) plot of –ln(I/I$_0$) as a function of time for different catalysts. The solid lines are the linear fits of the data and the slope gives k$_{app}$ of the reaction.

The accessibility of SiO_2-masked surface is much more difficult for the deposition of additional metals because the reduction typically involves two reactants: a relatively-large anion of transition metal complex and ascorbic acid. The assumption was examined by a model reaction involving two reactants, the reduction of *p*-nitrophenol by excess $NaBH_4$. The same amounts of dumbbell particles and core@shell particles were used to catalyze the *p*-nitrophenol reduction. The reaction was monitored by decreased intensity of absorbance at 400 nm corresponding to the disappearance of *p*-nitrophenol (**Fig. 7D**). The reduction could be treated as a pseudo first order reaction when $NaBH_4$ was in large excess.[51] The data were then plotted as first order with respect to *p*-nitrophenol (**Fig. 7E**). The rate constant of *p*-nitrophenol reduction on the dumbbell particles was found to be $(4.64\pm0.01)\times10^{-3}$ s^{-1}, more than 10 fold faster compare to the core@shell structures $(4.11\pm0.32)\times10^{-4}$ s^{-1}). In fact, the *p*-nitrophenol reduction on the core@shell particles deviates from the first order kinetics, suggesting that the concentration of $NaBH_4$ is insufficient to assume pseudo first order reaction. This result, in turn, implies that the diffusion rates of reactants are significantly reduced. Both the etching reaction of Au and the *p*-nitrophenol reduction have demonstrated that the SiO_2 coating indeed serve as a mask to block chemical reactions.

Conclusion

The MASG method has been developed using SiO_2 as a mask to partially protect the surface of seeds from further reaction and subsequently applied to synthesize Pd-Au and Pt-Au heterodimers and Pt-Pd-Au heterotrimers. The initial Au-SiO_2 dumbbell structures could be readily synthesized by a modified W/O microemulsion due to the phase separation of hydrophobic surface ligands and hydrophilic hydrolyzed TEOS. Further epitaxial growth of Pd and Pt on Au was observed. Interestingly, Pd is apt to laterally grow on Au by capping the

unblocked Au surface while Pt prefers to grow vertically into branched structures after initial deposition on Au. Replacing the noble metal with a *3d* transition metal as the second metal, the active metal could subsequently be oxidized or sulfurized to oxide or sulfide.[52-53] Therefore, the MASG method is potentially a versatile strategy to generate hybrid heteronanostructures with multi-components for improving the existing applications and finding new uses in many areas related to energy conversion and human health.

Supplemental Information

Experimental details, TEM characterization of Au nanoparticles and Pt-Pd-Au heteronanostructures synthesized without protection of SiO_2, UV-Vis spectra of Au nanoparticles and Au-SiO_2 dumbbells, as well as DDA simulation of optical spectra of individual Au nanospheres with different diameters.

Acknowledgement

References:

(1)   Ferrando, R.; Jellinek, J.; Johnston, R. L. Nanoalloys: From Theory to Applications of Alloy Clusters and Nanoparticles. *Chem. Rev.* **2008,** *108*, 845-910.

(2)   Zheng, H.; Li, Y.; Liu, H.; Yin, X.; Li, Y. Construction of Heterostructure Materials toward Functionality. *Chem. Soc. Rev.* **2011,** *40*, 4506-4524.

(3)   Walther, A.; Müller, A. H. E. Janus Particles: Synthesis, Self-Assembly, Physical Properties, and Applications. *Chem. Rev.* **2013,** *113*, 5194-5261.

(4)   Buck, M. R.; Schaak, R. E. Emerging Strategies for the Total Synthesis of Inorganic Nanostructures. *Angew. Chem. Int. Ed.* **2013,** *52*, 6154-6178.

(5)   Liu, F.; Lee, J. Y.; Zhou, W. Template Preparation of Multisegment PtNi Nanorods as Methanol Electro-Oxidation Catalysts with Adjustable Bimetallic Pair Sites. *J. Phys. Chem. B* **2004,** *108*, 17959-17963.

(6)   Liu, F.; Lee, J. Y.; Zhou, W. J. Multisegment PtRu Nanorods: Electrocatalysts with Adjustable Bimetallic Pair Sites. *Adv. Funct. Mater.* **2005,** *15*, 1459-1464.

(7)   Paxton, W. F.; Kistler, K. C.; Olmeda, C. C.; Sen, A.; St. Angelo, S. K.; Cao, Y.; Mallouk, T. E.; Lammert, P. E.; Crespi, V. H. Catalytic Nanomotors: Autonomous Movement of Striped Nanorods. *J. Am. Chem. Soc.* **2004,** *126*, 13424-13431.

(8)   Liu, R.; Sen, A. Autonomous Nanomotor Based on Copper–Platinum Segmented Nanobattery. *J. Am. Chem. Soc.* **2011,** *133*, 20064-20067.

(9)   Salem, A. K.; Searson, P. C.; Leong, K. W. Multifunctional Nanorods for Gene Delivery. *Nat. Mater.* **2003,** *2*, 668-671.

(10)   Park, S.; Son, Y. J.; Leong, K. W.; Yoo, H. S. Therapeutic Nanorods with Metallic Multi-Segments: Thermally Inducible Encapsulation of Doxorubicin for Anti-cancer Therapy. *Nano Today* **2012,** *7*, 76-84.

(11)   Nicewarner-Peña, S. R.; Freeman, R. G.; Reiss, B. D.; He, L.; Peña, D. J.; Walton, I. D.; Cromer, R.; Keating, C. D.; Natan, M. J. Submicrometer Metallic Barcodes. *Science* **2001,** *294*, 137-141.

(12)   Walton, I. D.; Norton, S. M.; Balasingham, A.; He, L.; Oviso, D. F.; Gupta, D.; Raju, P. A.; Natan, M. J.; Freeman, R. G. Particles for Multiplexed Analysis in Solution: Detection and Identification of Striped Metallic Particles Using Optical Microscopy. *Anal. Chem.* **2002,** *74*, 2240-2247.

(13)   Al-Mawlawi, D.; Liu, C.; Moskovits, M. Nanowires Formed in Anodic Oxide Nanotemplates. *J. Mater. Res.* **1994,** *9*, 1014-1018.

(14)   Hulteen, J. A General Template-based Method for the Preparation of Nanomaterials. *J. Mater. Chem.* **1997,** *7*, 1075-1087.

(15)   Martin, B. R.; Dermody, D. J.; Reiss, B. D.; Fang, M.; Lyon, L. A.; Natan, M. J.; Mallouk, T. E. Orthogonal Self-Assembly on Colloidal Gold-Platinum Nanorods. *Adv. Mater.* **1999,** *11*, 1021-1025.

(16)   Anderson, M. E.; Buck, M. R.; Sines, I. T.; Oyler, K. D.; Schaak, R. E. On-Wire Conversion Chemistry: Engineering Solid-State Complexity into Striped Metal Nanowires using Solution Chemistry Reactions. *J. Am. Chem. Soc.* **2008,** *130*, 14042-14043.

(17)   Leonard, B. M.; Anderson, M. E.; Oyler, K. D.; Phan, T.-H.; Schaak, R. E. Orthogonal Reactivity of Metal and Multimetal Nanostructures for Selective, Stepwise, and Spatially-Controlled Solid-State Modification. *ACS Nano* **2009,** *3*, 940-948.

(18)   Savas, T.; Schattenburg, M.; Carter, J.; Smith, H. I. Large-area Achromatic Interferometric Lithography for 100 nm Period Gratings and Grids. *J. Vac. Sci. & Tech. B* **1996,** *14*, 4167-4170.

(19)   Nikoobakht, B.; El-Sayed, M. A. Preparation and Growth Mechanism of Gold Nanorods (NRs) Using Seed-Mediated Growth Method. *Chem. Mater.* **2003,** *15*, 1957-1962.

(20)   Gole, A.; Murphy, C. J. Seed-Mediated Synthesis of Gold Nanorods: Role of the Size and Nature of the Seed. *Chem. Mater.* **2004,** *16*, 3633-3640.

(21)   Habas, S. E.; Lee, H.; Radmilovic, V.; Somorjai, G. A.; Yang, P. Shaping Binary Metal Nanocrystals through Epitaxial Seeded Growth. *Nat. Mater.* **2007,** *6*, 692-697.

(22)   Lim, B.; Jiang, M.; Camargo, P. H.; Cho, E. C.; Tao, J.; Lu, X.; Zhu, Y.; Xia, Y. Pd-Pt Bimetallic Nanodendrites with High Activity for Oxygen Reduction. *Science* **2009,** *324*, 1302-1305.

(23)   DeSantis, C. J.; Sue, A. C.; Bower, M. M.; Skrabalak, S. E. Seed-Mediated Co-reduction: A Versatile Route to Architecturally Controlled Bimetallic Nanostructures. *ACS Nano* **2012,** *6*, 2617-2628.

(24)   Chen, S.; Jenkins, S. V.; Tao, J.; Zhu, Y.; Chen, J. Anisotropic Seeded Growth of Cu–M (M= Au, Pt, or Pd) Bimetallic Nanorods with Tunable Optical and Catalytic Properties. *J. Phys. Chem. C* **2013,** *117*, 8924-8932.

(25)   Pellegrino, T.; Fiore, A.; Carlino, E.; Giannini, C.; Cozzoli, P. D.; Ciccarella, G.; Respaud, M.; Palmirotta, L.; Cingolani, R.; Manna, L. Heterodimers Based on $CoPt_3-Au$ Nanocrystals with Tunable Domain Size. *J. Am. Chem. Soc.* **2006,** *128*, 6690-6698.

(26) Lim, B.; Kobayashi, H.; Yu, T.; Wang, J.; Kim, M. J.; Li, Z.-Y.; Rycenga, M.; Xia, Y. Synthesis of Pd−Au Bimetallic Nanocrystals via Controlled Overgrowth. *J. Am. Chem. Soc.* **2010,** *132*, 2506-2507.

(27) Zeng, J.; Zhu, C.; Tao, J.; Jin, M.; Zhang, H.; Li, Z. Y.; Zhu, Y.; Xia, Y. Controlling the Nucleation and Growth of Silver on Palladium Nanocubes by Manipulating the Reaction Kinetics. *Angew. Chem. Int. Ed.* **2012,** *51*, 2354-2358.

(28) Zhu, C.; Zeng, J.; Tao, J.; Johnson, M. C.; Schmidt-Krey, I.; Blubaugh, L.; Zhu, Y.; Gu, Z.; Xia, Y. Kinetically Controlled Overgrowth of Ag or Au on Pd Nanocrystal Seeds: From Hybrid Dimers to Nonconcentric and Concentric Bimetallic Nanocrystals. *J. Am. Chem. Soc.* **2012,** *134*, 15822-15831.

(29) Yang, Y.; Wang, W.; Li, X.; Chen, W.; Fan, N.; Zou, C.; Chen, X.; Xu, X.; Zhang, L.; Huang, S. Controlled Growth of Ag/Au Bimetallic Nanorods through Kinetics Control. *Chem. Mater.* **2012,** *25*, 34-41.

(30) Xie, S.; Peng, H.-C.; Lu, N.; Wang, J.; Kim, M. J.; Xie, Z.; Xia, Y. Confining the Nucleation and Overgrowth of Rh to the {111} Facets of Pd Nanocrystal Seeds: The Roles of Capping Agent and Surface Diffusion. *J. Am. Chem. Soc.* **2013,** *135*, 16658-16667.

(31) Chen, T.; Chen, G.; Xing, S.; Wu, T.; Chen, H. Scalable Routes to Janus Au−SiO$_2$ and Ternary Ag−Au−SiO$_2$ Nanoparticles. *Chem. Mater.* **2010,** *22*, 3826-3828.

(32) Ohmori, M.; Matijević, E. Preparation and Properties of Uniform Coated Inorganic Colloidal Particles: 8. Silica on Iron. *J. Colloid Interface Sci.* **1993,** *160*, 288-292.

(33) Liz-Marzán, L. M.; Philipse, A. P. Synthesis and Optical Properties of Gold-Labeled Silica Particles. *J. Colloid Interface Sci.* **1995,** *176*, 459-466.

(34) Roca, M.; Haes, A. J. Silica−Void−Gold Nanoparticles: Temporally Stable Surface-Enhanced Raman Scattering Substrates. *J. Am. Chem. Soc.* **2008,** *130*, 14273-14279.

(35) Guerrero-Martínez, A.; Pérez-Juste, J.; Liz-Marzán, L. M. Recent Progress on Silica Coating of Nanoparticles and Related Nanomaterials. *Adv. Mater.* **2010,** *22*, 1182-1195.

(36) Johnson, C. L.; Snoeck, E.; Ezcurdia, M.; Rodriguez-Gonzalez, B.; Pastoriza-Santos, I.; Liz-Marzan, L. M.; Hytch, M. J. Effects of Elastic Anisotropy on Strain Distributions in Decahedral Gold Nanoparticles. *Nat. Mater.* **2008,** *7*, 120-124.

(37) Jungjohann, K. L.; Bliznakov, S.; Sutter, P. W.; Stach, E. A.; Sutter, E. A. In Situ Liquid Cell Electron Microscopy of the Solution Growth of Au–Pd Core–Shell Nanostructures. *Nano Lett.* **2013,** *13*, 2964-2970.

(38)   Kibler, L. A.; Kleinert, M.; Randler, R.; Kolb, D. M. Initial Stages of Pd Deposition on Au(hkl) Part I: Pd on Au(111). *Surf. Sci.* **1999,** *443*, 19-30.

(39)   Naohara, H.; Ye, S.; Uosaki, K. Electrochemical Layer-by-Layer Growth of Palladium on an Au(111) Electrode Surface: Evidence for Important Role of Adsorbed Pd Complex. *The Journal of Physical Chemistry B* **1998,** *102*, 4366-4373.

(40)   Ding, Y.; Fan, F.; Tian, Z.; Wang, Z. L. Atomic Structure of Au−Pd Bimetallic Alloyed Nanoparticles. *J. Am. Chem. Soc.* **2010,** *132*, 12480-12486.

(41)   Koel, B. E.; Sellidj, A.; Paffett, M. T. Ultrathin Films of Pd on Au(111): Evidence for Surface Alloy Formation. *Phys. Rev. B* **1992,** *46*, 7846-7856.

(42)   Shibata, T.; Bunker, B. A.; Zhang, Z.; Meisel, D.; Vardeman, C. F.; Gezelter, J. D. Size-Dependent Spontaneous Alloying of Au−Ag Nanoparticles. *J. Am. Chem. Soc.* **2002,** *124*, 11989-11996.

(43)   Langhammer, C.; Yuan, Z.; Zoric, I.; Kasemo, B. Plasmonic Properties of Supported Pt and Pd Nanostructures. *Nano Lett.* **2006,** *6*, 833-838.

(44)   Draine, B. T.; Flatau, P. J. Discrete-Dipole Approximation for Scattering Calculations. *J. Opt. Soc. Am. A* **1994,** *11*, 1491-1499.

(45)   Liao, H.-G.; Cui, L.; Whitelam, S.; Zheng, H. Real-time Imaging of Pt_3Fe Nanorod Growth in Solution. *Science* **2012,** *336*, 1011-1014.

(46)   Li, D.; Nielsen, M. H.; Lee, J. R.; Frandsen, C.; Banfield, J. F.; De Yoreo, J. J. Direction-specific Interactions Control Crystal Growth by Oriented Attachment. *Science* **2012,** *336*, 1014-1018.

(47)   Waibel, H.-F.; Kleinert, M.; Kibler, L.; Kolb, D. Initial Stages of Pt Deposition on Au (111) and Au (100). *Electrochim. Acta* **2002,** *47*, 1461-1467.

(48)   Sanchez, S. I.; Small, M. W.; Zuo, J.-m.; Nuzzo, R. G. Structural Characterization of Pt−Pd and Pd−Pt Core−Shell Nanoclusters at Atomic Resolution. *J. Am. Chem. Soc.* **2009,** *131*, 8683-8689.

(49)   Koole, R.; van Schooneveld, M. M.; Hilhorst, J.; de Mello Donegá, C.; Hart, D. C. '.; van Blaaderen, A.; Vanmaekelbergh, D.; Meijerink, A. On the Incorporation Mechanism of Hydrophobic Quantum Dots in Silica Spheres by a Reverse Microemulsion Method. *Chem. Mater.* **2008,** *20*, 2503-2512.

(50)   Park, S.-J.; Kim, Y.-J.; Park, S.-J. Size-Dependent Shape Evolution of Silica Nanoparticles into Hollow Structures. *Langmuir* **2008,** *24*, 12134-12137.

(51)   Herves, P.; Pérez-Lorenzo, M.; Liz-Marzán, L. M.; Dzubiella, J.; Lu, Y.; Ballauff, M. Catalysis by Metallic Nanoparticles in Aqueous Solution: Model Reactions. *Chem. Soc. Rev.* **2012,** *41*, 5577-5587.

(52)   Hung, L.-I.; Tsung, C.-K.; Huang, W.; Yang, P. Room-Temperature Formation of Hollow Cu_2O Nanoparticles. *Adv. Mater.* **2010,** *22*, 1910-1914.

(53)   Motl, N. E.; Bondi, J. F.; Schaak, R. E. Synthesis of Colloidal Au–Cu_2S Heterodimers via Chemically Triggered Phase Segregation of AuCu Nanoparticles. *Chem. Mater.* **2012,** *24*, 1552-1554.

Appendix A: Supplemental Information

Experimental Details:

Chemicals. Hydrogen tetrachloroaurate trihydrate ($HAuCl_4 \cdot 3H_2O$, 99.99%), potassium tetrachloroplatinate (K_2PtCl_4, 99.9%), potassium tetrachloropalladate (K_2PdCl_4, 99.9%), and ammonium hydroxide (28-30% $NH_3 \cdot H_2O$) were purchased from Alfa Aesar. Tetradecylamine (TDA, >95%) was purchased from TCI. Tetraethoxysilane (TEOS, 98%), poly(oxyethylene) nonylphenyl ether (Igepal CO-520), and polyvinylpyrrolidone (PVP, M.W. = 55,000) were purchased from Sigma-Aldrich. Cyclohexane (ACS grade) was purchased from EMD. All chemicals were used as received unless specified otherwise.

Synthesis of Au-SiO₂ Dumbbells. The Au-SiO_2 dumbbells were synthesized by controlling the hydrolysis and condensation of the SiO_2 precursor during the coating process using W/O microemulsions. Initially, 10-nm Au nanoparticles were prepared by reducing $HAuCl_4 \cdot 3H_2O$ (19.7 mg, 0.05 mmol) in 5 g of TDA at 160 $^{\circ}$C for 20 min under argon. After the reaction, the product was cooled to 100 $^{\circ}$C and purified with toluene and ethanol to remove unreacted precursor and excess TDA. The Au nanoparticles were then dispersed in cyclohexane for silica coating in W/O microemulsions. In a typical procedure, 1 mL of 200 nM Au nanoparticles was added to the mixture of 0.14 M Igepal CO-520 in 40 mL cyclohexane in a round-bottom flask equipped with a magnetic stirring bar. Various amounts of TEOS (20-200 mL) were added to the reaction mixture and allowed to mix for 30 min before the addition of 0.280 mL of $NH_3 \cdot H_2O$. The Au-SiO_2 dumbbell structures were formed when less than 50 mL of TEOS was used. The reaction was allowed to proceed for 48 h and stopped by adding ethanol to interrupt the emulsion. The product was washed by ethanol and dispersed in 18 MΩ H_2O for future use.

Synthesis of Pd-Au Dimers. The Pd-Au dimers were synthesized by reducing the Pd precursor in the presence of Au-SiO$_2$ dumbbells using ascorbic acid. In a typical procedure, 8 mL of K$_2$PdCl$_4$ was added, at a rate of 0.1 mL/min, to a 5 ml aqueous solution containing Au-SiO$_2$ dumbbells (~15 pmol) and PVP (1 mg/mL) at room temperature. Final concentrations of K$_2$PdCl$_4$ (0.06, 0.2, and 0.35 mM) in the reactions were used to yield Pd depositions with different thickness of ~4, ~7, and ~10 nm, respectively. The molar ratio of ascorbic acid to K$_2$PdCl$_4$ was kept at 10 to 1 for all three reactions. The product was washed by ethanol and dispersed in 18 MΩ H$_2$O. The SiO$_2$ component was then dissolved by mixing the Pd-Au-SiO$_2$ particles overnight in an aqueous solution containing excess NaOH and PVP (10 mg/mL). The product was washed with water and dispersed in 18 MΩ H$_2$O.

The thickness (x_{Pd}) of Pd deposition was estimated using a crude model which approximates the Pd layer is a semi-spherical shell interfacing with a spherical Au core. The radius of the semi-shell (r_{Pd}) can be derived from the average volume of Pd (nm^3 per particle):

$V_{Pd} = \dfrac{1}{2}\left(\dfrac{4}{3}\pi r_{Pd}^3 - \dfrac{4}{3}\pi r_{Au}^3\right)$, where r_{Au} is the radius of the Au core that can be measured from the

transmission electron microscopy (TEM) image. The V$_{Pd}$ was obtained from $\dfrac{V_{Pd}}{V_{Au}} = \dfrac{C_{Pd}\,a_{Pd}^3}{C_{Au}\,a_{Au}^3}$,

where V_{Au} is the average volume of Au (nm^3 per particle) assuming spherical shape ($V_{Au} = \dfrac{4}{3}\pi r_{Au}^3$

); C_{Pd} and C_{Au} are the concentration of Pd and Au (mol/L), respectively, which can be measured from the bulk sample; a_{Pd} and a_{Au} are the lattice constant of Pd and Au (nm), respectively. The difference of the r_{Pd} and r_{Au} gives the thickness of the Pd semi-shell: $x_{Pd} = r_{Pd} - r_{Au}$.

To examine the sensitivity of the optical spectra to the geometrical details of the model, a second plausible model of the Au-Pd dimer was constructed. In this model, the semi-spherical Pd

shell was replaced by an ellipsoidal shell with the same volume. The ellipsoidal Pd shell was constructed by carving an oblate ellipsoid to cover the Au sphere at the equator. The center of the ellipsoid was displaced from the center of Au sphere by a distance d, along the short axis of the oblate ellipsoid. It can be shown that the thickness of the ellipsoid when measure along the short-axis can be calculated with the equation,

$$x_{Pd} = c_{Pd} + d - r_{Au},$$ (1)

where c_{Pd} is the length of the short axis of the oblate ellipsoid

$$\frac{x^2}{a_{Pd}^2} + \frac{y^2}{a_{Pd}^2} + \frac{z^2}{c_{Pd}^2} = 1.$$

In order to have the same thickness x_{Pd} and V_{Pd}, the long and short axes for the partial ellipsoidal shells have to be 8.7 nm and 4.95 nm, 11.7 nm and 6.4 nm and 14.8 nm and 7.7 nm for the thickness of 4 nm, 7 nm, 10 nm models, respectively.

Synthesis of Pt-Au Dimers. The procedure for Pt-Au dimers was the same as that for Pd-Au dimers described above, with the exception that K_2PtCl_4 was used as the Pt precursor and final concentration of Pt in the reaction solution is 2.4mM.

Synthesis of Pt-Pd-Au Trimers. The Pt-Pd-Au trimmers were synthesized using a similar procedure as that for Pt-Au dimers except that the Au-SiO$_2$ was replaced by the pre-synthesized Pd-Au-SiO$_2$ described above.

Etching of Au from Au-SiO$_2$ Nanostructures. The Au nanoparticles were etched from the Au-SiO$_2$ nanostructures by the KCN. Typically, KCN was added to a solution of Au-SiO$_2$ nanostructures at a molar ratio of 1:5 Au to KCN. The solution was allowed to etch overnight until a colorless product remained.

Catalytic Reaction on Au-SiO₂ Nanostructures. Reduction of 4-nitrophenol on Au-SiO$_2$ nanostructures were carried out to mimic the reduction of second metal occurring on the surface of the seeds. In a typical measurement, aqueous solutions of *p*-nitrophenol (1.4 mM) and NaBH$_4$ (0.41 M) were freshly prepared as separate stock solutions. Deionized water (8.0 mL) was mixed with 1.0 mL of *p*-nitrophenol stock solution. The color of the solution changed from colorless to yellow as soon as 1.0 mL of NaBH$_4$ stock solution was added. Then, 7.0 mL of catalysts was added into the system with a final concentration of 7.6×10^9 particles/mL. Immediately after mixing, 2.0 mL of the reaction solution was quickly transferred into a quartz cuvette and the absorbance spectra were recorded using UV-vis spectrometer over a certain period of time.

Calculation of Optical Properties. The optical properties were calculated according to the discrete dipole approximation (DDA) using the DDSCAT 7.3 program. In this formalism, the particles are represented by an array of dipole moments residing within the volume of the nanoparticles. The nanoparticles were represented as a dielectric continuum with the complex dielectric response function of the respective metals in water. The optical efficiency, Q, was reported as the ratio of the respective optical cross section to $\pi \cdot a_{eff}^2$, where the effective radius, a_{eff}, is defined as the radius of a sphere whose volume is equal to that of the nanoparticle. The optical cross sections were averaged over two orthogonal polarization directions of the incident light.

Characterization. Transmission electron microscopy (TEM) images were captured using a JEOL 100cx microscope with an accelerating voltage of 100 kV. High angle annular dark field scanning transmission electron microscopy (HAADF-STEM) images, high-resolution TEM (HRTEM) images, and energy-dispersive X-ray (EDX) mapping were obtained using a double Cs-corrected JEOL JEM-ARM200F microscope. X-ray diffraction (XRD) patterns were acquired

using a Rigaku MiniFlex X-ray diffractometer equipped with Cu K⬜ radiation source operated at 30 kV/15 mA. The concentrations of metals were determined using a GBC 932 atomic absorption (AA) spectrometer. UV-vis spectra were taken on an HP 8453 UV-visible spectrophotometer.
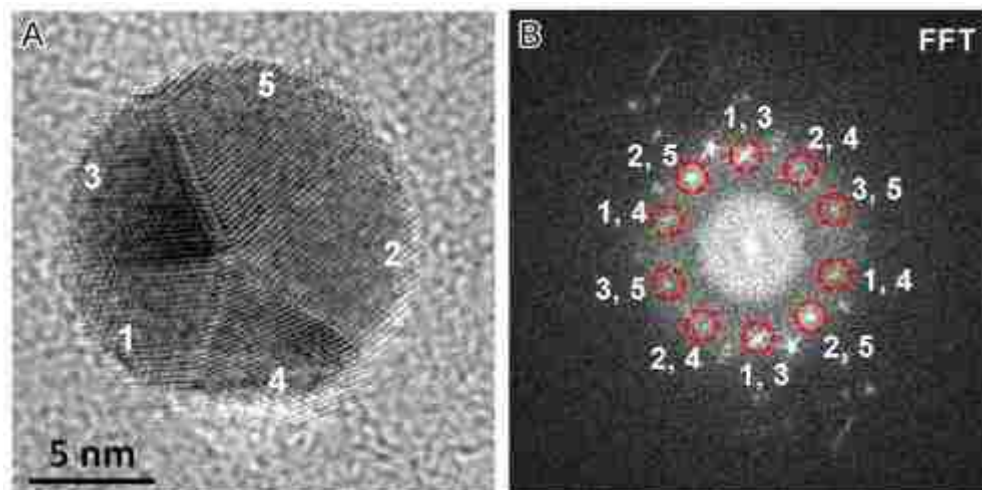
Figure S1. HRTEM analysis of individual Au nanoparticles synthesized by reducing chloroauric acid using TDA as capping ligands: (A) HRTEM image; and (B) Fourier fast transform (FFT) of (A). The indexes in (B) are corresponding to the domains in (A). Each crystal domain is at an orientation close to the [110] zone and contribute to four {111} reflections in pattern of the FFT circled in the red, suggesting a decahedral five-fold twined structure of the Au nanoparticle.
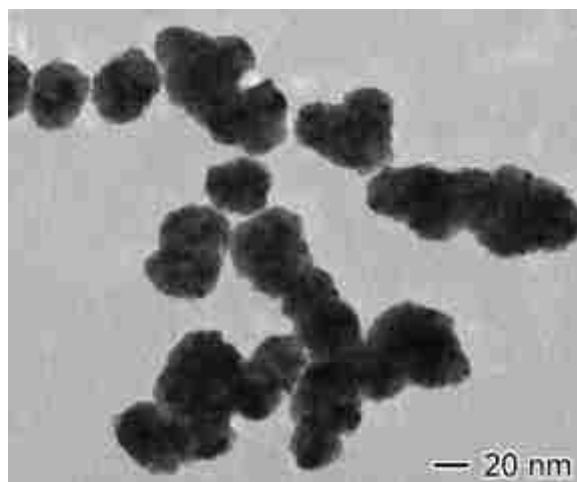
Figure S2. TEM image of Au-Pd nanoparticles synthesized using the identical conditions as Au-Pd dumbbells except that the Au cores were unprotected by SiO_2.
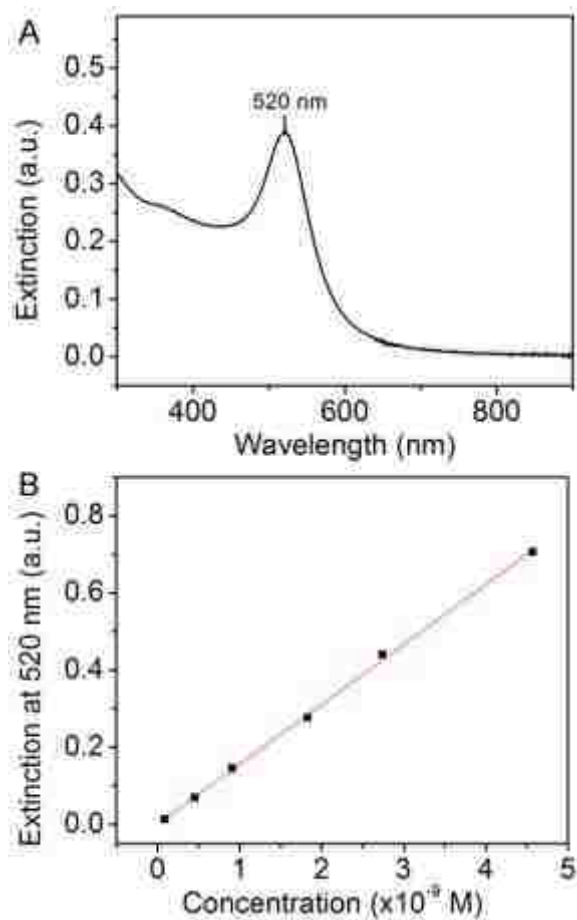
Figure S3. (A) UV-Vis spectrum of the Au nanoparticles suspended in toluene. (B) Plot of extinction at 520 nm as a function of particle concentration. The red line is the linear fitting of the data: $y = (1.55 \pm 0.01) \times 10^8 x; R = 0.9996$. The extinction coefficient (ε_{Au}) of the Au nanoparticle suspension at 520 nm is $(1.55 \pm 0.01) \times 10^8 \, \text{M}^{-1} \cdot \text{cm}^{-1}$.
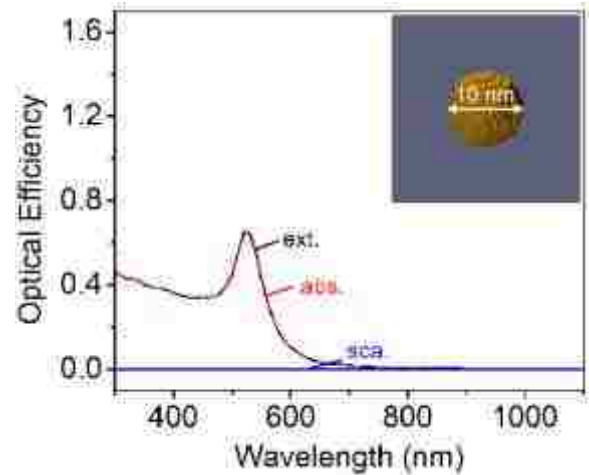
Figure S4. DDA simulation of the optical spectra of a Au nanoparticle with a diameter of 10 nm in water. The inset shows the geometry of the Au nanoparticle.
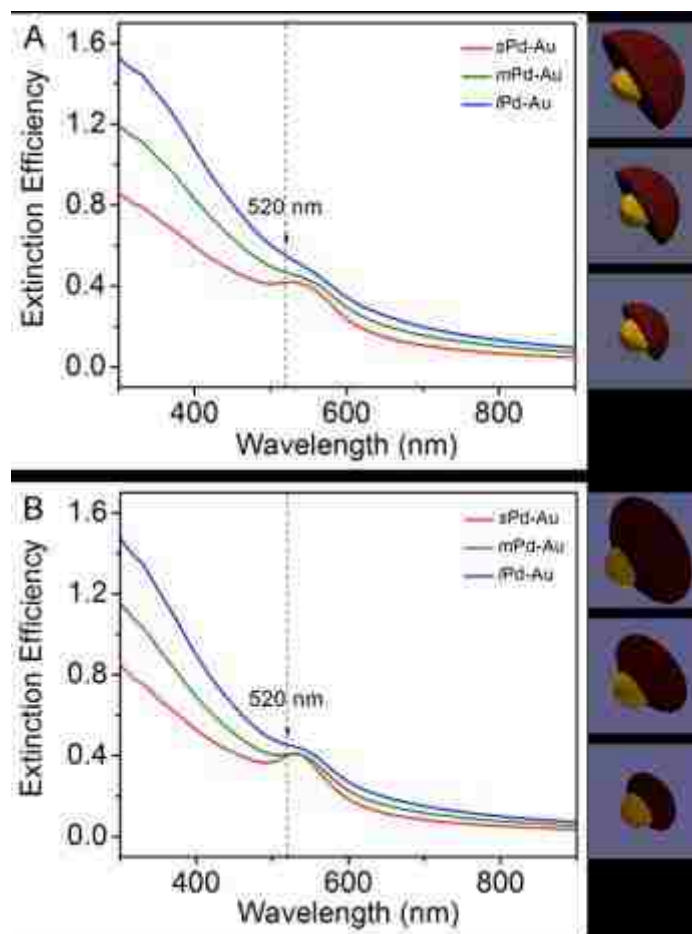
Figure S5. DDA simulation of the optical spectra of Pd-Au heterodimers with a Pd thick deposition of 4, 7, and 10 nm on a Au nanosphere with a diameter of 10 nm, denoted as *s*Pd-Au, *m*Pd-Au, *l*Pd-Au, respectively, using two models: (A) a semispherical Pd shell interfacing with a spherical Au core; and (B) an ellipsoidal Pd shell carving on a spherical Au core. The right panel shows the corresponding geometries used for the simulation.
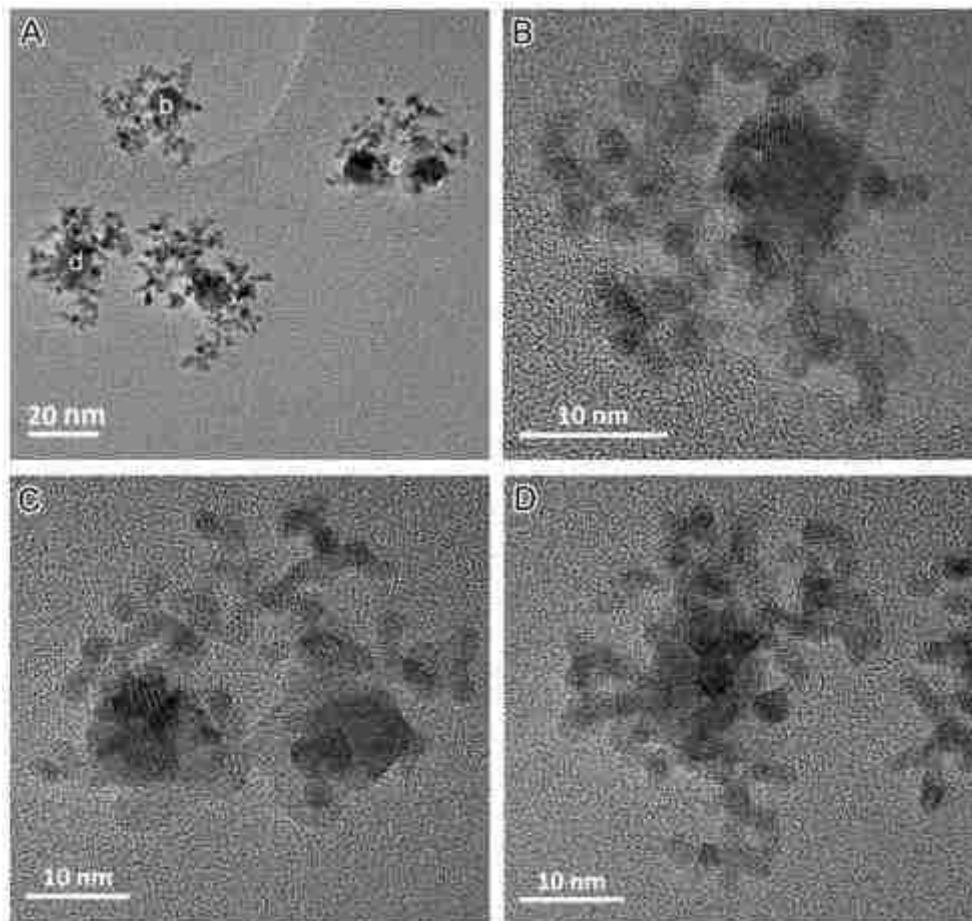
Figure S6. TEM characterization of Pt-Pd-Au heterostructures synthesized by reducing Pt precursor on Pd-Au heterodimers after silica coating was removed under basic condition: (A) overview and (B-D) HRTEM of individual particles corresponding to a, b, and c in (A). Pt was found to grow on both Pd and Au of the dimers.
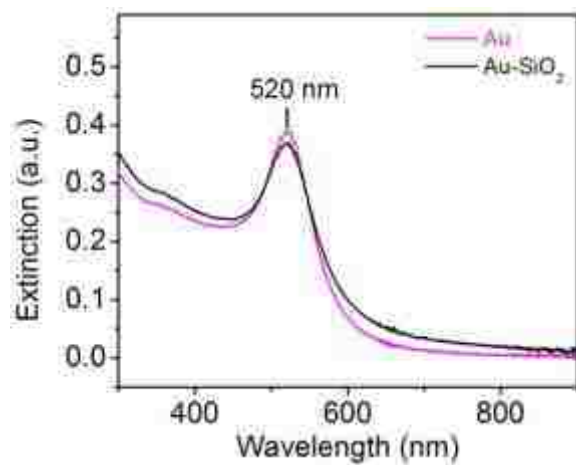
Figure S7. UV-Vis spectra of Au nanoparticles suspended in toluene and Au-SiO$_2$ dumbbell nanoparticles suspended in water.
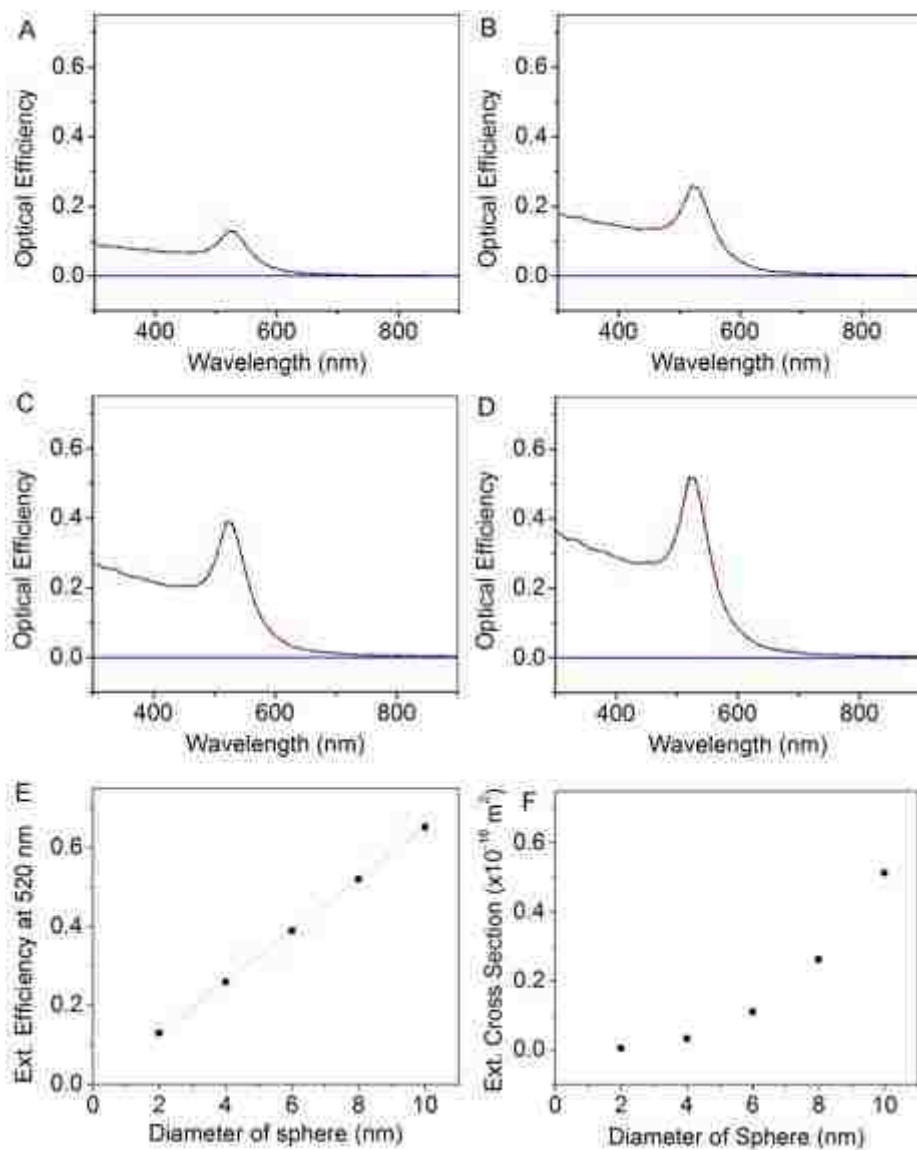
Figure S8. DDA simulation of optical spectra of individual Au nanospheres with different diameters: (A) 2 nm; (B) 4 nm; (C) 6 nm; and (D) 8 nm. (E) Plot of extinction efficiency at 520 nm as a function of the diameter of a Au nanosphere. (F) Plot of extinction cross section at 520 nm as a function of the diameter of a Au nanosphere.

Chapter III. Synthesis of Copper-Silica Core-Shell Nanostructures with Sharp and Stable Localized Surface Plasmon Resonance*

Abstract

Copper nanoparticles exhibit intense and sharp localized surface plasmon resonance (LSPR) in the visible region; however, the LSPR peaks become weak and broad when exposed to air due to the oxidation of Cu. In this work, the Cu nanoparticles are successfully encapsulated in SiO_2 by employing trioctyl-n-phosphine (TOP) capped Cu nanoparticles for the sol-gel reaction, yielding an aqueous $Cu-SiO_2$ core-shell suspension with stable and well-preserved LSPR properties of the Cu cores. With the TOP capping, the oxidation of the Cu cores in the microemulsion was significantly reduced, thus allowing the Cu cores to sustain the sol-gel process used for coating the SiO_2 protection layer. It was found that the self-assembled TOP-capped Cu nanoparticles were spontaneously disassembled during the sol-gel reaction, thus recovering the LSPR of individual particles. During the disassembling progress, the extinction spectrum of the nanocube agglomerates evolved from a broad extinction profile to a narrow and sharp peak. For a mixture of nanocubes and nanorods, the spectra evolved to two distinct peaks during the dissembling process. The observed spectra match well with the numerical simulations. These $Cu-SiO_2$ core-shell nanoparticles with sharp and stable LSPR may greatly expand the utilization of Cu nanoparticles in aqueous environments.

Introduction

Plasmonic metal nanostructures have attracted considerable interests because of their superior ability to manipulate light at the nanoscale, which make them particularly useful for sensing, optical waveguiding, telecommunication, biomedicine, and plasmon-enhanced photocatalysis.[1-8] Several metals, such as Ag, Au, and Cu, exhibit plasmonic resonances in the visible region.[9] Compared to Ag and Au, Cu is more earth abundant, thus particularly appealing as a low-cost plasmonic metal for practical applications. While much effort has been devoted to the nanostructures made of noble metals Ag and Au,[1] only limited success has been met with Cu. For example, Cu nanoparticles made by lithography on a substrate could display an intense localized surface plasmon resonance (LSPR) peak with a narrow band-width comparable to that of Ag and Au.[10] By varying the geometry, the plasmonic resonance of Cu nanoshells can be tuned away from the interband transitions of Cu to the near infrared (NIR) region similar to that of the Au nanoshells.[11] Similar to the Ag one-dimensional (1-D) array, a 1-D Cu array has been demonstrated to propagate surface plasmons at the Cu-silicon interface at infrared (IR) wavelengths which could offer a promising plasmonic interconnection in silicon-based integrated circuits.[12] Moreover, Cu nanoparticles supported on graphene could excite energetic electrons under visible irradiation to enable a photocatalytic route for the production of azo compounds.[13] Despite these exciting applications of Cu, the superior plasmonic properties of Cu nanoparticles are often compromised by surface oxidation. Being a much more reactive metal than Au or Ag, when exposed to air, the oxidation significantly broadens the LSPR peak and decreases the peak intensity of Cu nanoparticles. The surface oxidation to form oxides (i.e., Cu_2O, CuO, and $CuO_{0.67}$) is difficult to prevent by the use of surface ligands, especially for long periods of

time.[10, 14] The oxidation issue is a major challenge that has yet to be overcome for practical applications involving Cu nanostructures.

Several strategies have been used to address the oxidation issue of Cu nanoparticles. One approach was to remove oxides post facto from the Cu nanostructures by oxide removal agents (e.g. acetic acid).[10, 15] Alternatively, reducing agents (e.g. N_2H_4 or ascorbic acid) could be used to slow the formation of oxides during synthesis;[15-16] however, the agents used with either approach could change the surface morphology of the nanostructures, especially for smaller particles, which may result in the change of their optical properties. Another commonly-used method relied on the choice of stabilizers during chemical synthesis. For example, polyvinylpyrrolidone (PVP) was used as a capping agent for Cu nanoparticles to limit oxidation.[17-19] XRD results showed that these PVP-capped Cu nanoparticles were stable in a vial for fairly long time (e.g. 20 days) under ambient conditions;[17] however, large amount of PVP were required to reduce the oxidation rate.[19] In oil-based synthesis, trioctylphosphine (TOP) was demonstrated as a good capping ligand that can prevent the oxidation of Cu nanostructures.[20] A similar method that employed TOP during particle growth has been shown to yield stable and uniform cubic Cu nanoparticles; however, the particles had to be suspended in organic solvents.[21] It remains very challenging to synthesize stable Cu nanoparticles with controllable optical properties in aqueous solutions. Herein, we develop a SiO_2 coating method to transfer TOP-capped Cu nanoparticles to aqueous solution and demonstrate that the LSPR properties of these Cu-SiO_2 nanoparticles can be preserved for a long period of time.

SiO_2 has been widely used as an excellent protective material against corrosion.[22] Many efforts have been made to coat metal nanoparticles with silica shells with controllable thickness; however, these studies were limited to noble metals (i.e., Au and Ag) using the modified Stöber

method. For example, Stöber growth of the silica shell mediated by a silane primer was developed to coat silica on citrate-coated Au nanoparticles or Ag colloids.[23-24] A layer-by-layer technique was employed to form an intermediate layer prior to the Stöber method for coating silica on CTAB-stabilized Au nanorods.[25] Methods were also developed to coat Au or Ag nanoparticles in one step without involving the primers.[26-27] Combination of reduction and encapsulation of Cu in a one-pot synthesis has been demonstrated to produce ultrafine Cu nanoparticles inside thick SiO_2 shells.[28] Despite this progress, applying a Stöber approach to active metals was proven to be nontrivial due to their high reactivity with oxygen and ammonia.[24, 27] To the best of our knowledge, no reports were found to successfully coat silica on the active metal Cu nanoparticles while still maintaining their optical properties, although thermal annealing of Cu nanoparticles in glass[29] or in SiO_2 matrices[30-31] was demonstrated to embed small Cu nanoparticles in bulk SiO_2 for optical measurements. The challenge in coating Cu nanoparticles with SiO_2 shells arises from the high instability of Cu nanoparticles in the sol-gel reactions. This work for the first time successfully overcomes the instability challenge of Cu nanoparticles in the sol-gel reactions and demonstrates the successful synthesis of stable Cu-SiO_2 core-shell nanoparticles with sharp and intense LSPR. It is accomplished by introducing the TOP-passivated Cu nanoparticles with controllable size and shape for the synthesis of Cu-SiO_2 core-shell structures using a sol-gel process in a water/oil (W/O) microemulsion. The use of TOP dramatically improves the stability of Cu nanoparticles in the sol-gel process, thereby preserving the optical properties of Cu nanoparticles after the synthesis. The thickness of the SiO_2 shell increases with increased reaction time, but the shell remains accessible to solvent molecules such as water. Furthermore, the self-assembled TOP-capped nanoparticles suspended in toluene could be effectively disassembled during the sol-gel reaction to recover their optical properties of

individual nanoparticles in aqueous solution. This process was monitored by the optical spectra during the reaction and the results are compared with numerical simulations. This method may enable further use of plasmonic Cu nanoparticles in aqueous solution for biological and catalytic applications.

Methods

Chemicals. Copper (II) 2,4-pentanedionate (Cu(acac)$_2$, 98%), 1-octadecene (ODE, 90%), tetraethoxysilane (TEOS, 98%), tri-n-octylphosphine (TOP, 90%), and sodium hydroxide (NaOH, 98%) were purchased from Alfa Aesar. Oleylamine (OLAM, 70%) and poly-(oxyethylene) nonylphenyl ether (Igepal CO-520) were purchased from Sigma-Aldrich. Hexanes (ACS grade) and formic acid (99%) were purchased from EMD. Sulfuric acid (ACS grade, 98%) was purchased from BDH. All experiments were performed using 18 MΩ H$_2$O unless specified otherwise. All chemicals were used as received.

Synthesis of Copper Nanoparticles. Cu nanoparticles were synthesized by reducing Cu precursor in a mixture of ODE and OLAM in the presence of CO and formic acid vapor. Typically, Cu(acac)$_2$ (52.4 mg, 0.2 mmol) was added in the mixture of 4 mL ODE and 1 mL OLAM in a 25-mL 3-neck round bottom flask equipped with magnetic stirring and connected to a water-cooled condenser. Ar was used to displace air and protect the mixture in the reaction flask prior to the addition of 1 mL TOP. While maintaining the Ar protection, the reaction mixture was heated to 220 $^{\circ}$C. To produce cubes, a small amount of CO (~15 mL) generated from the dehydration of formic acid by sulfuric acid was flown over the hot reaction solution at 200 $^{\circ}$C. To produce mixtures of cubes and rods, CO was introduced by flowing the vapor over the reaction at 140 $^{\circ}$C. After the reaction proceeded at 220 $^{\circ}$C for another 20 min, the reaction

was quenched by removal of the heating mantle and was allowed to cool to room temperature. Ethanol/toluene at a 4:1 ratio (25 mL) was added to the reaction mixture prior to centrifugation at 7800 rcf for 5 min to remove excess Cu precursor and surfactants. After discarding the supernatant, the pellet was dispersed in toluene for future use.

Synthesis of Cu-SiO₂ Core-Shell Nanostructures. The Cu-SiO$_2$ core-shell nanostructures were synthesized by modifying our established W/O microemulsion method.[32] Typically, 1.2 mL Igepal CO-520 was added to 20 mL hexane in a 50-mL round bottom flask, followed by addition of Cu nanoparticles (~8 pmol or ~1 mg) and 30 mL TEOS. The sol-gel reaction was catalyzed by adding 140 ml of 20 mM NaOH. The reaction was then allowed to precede either ~24 h to produce thin silica shells or > 48 h for thicker silica shells. After the reaction completed, equal volume of ethanol was added the reaction mixture, followed by centrifuging at 12,000 rcf for 30 min to collect the product. The product was further purified with 30 mL ethanol twice, and collected by centrifuging at 12,000 rcf for 30 min or until a solid pellet was formed. The pellet was dispersed in water for further use.

Characterization. Transmission electron microscopy (TEM) images were captured using a transmission electron microscope (JEOL JEM-1011) with an accelerating voltage of 100 kV. X-ray powder diffraction (XRD) was performed using a bench-top x-ray diffractometer (Rigaku Miniflex II). The hydrodynamic diameters of the products were measured using a dynamic light scattering (DLS) instrument (Brookhaven ZetaPALS). The concentration of Cu was determined using a flame atomic absorption (AA) spectrometer (GBC 932). UV-vis spectra were taken on a UV-vis spectrophotometer (Agilent Cary 50).

Simulation. The optical properties were calculated according to the discrete dipole approximation (DDA) using the DDSCAT 7.3 program.[33-34] In this formalism, the structure is

represented by an array of dipole moments residing within its volume. Each volume element is represented as a dielectric continuum with the complex dielectric response function of bulk Cu.[35] The optical cross sections were averaged over the two orthogonal polarization directions of the incident light. The optical efficiency, Q, is reported as the ratio of the respective optical cross section to $\pi \cdot a_{eff}^2$, where the effective radius, a_{eff}, is defined as the radius of a sphere whose volume is equal to that of the structure. Optical spectra including extinction, absorption, and scattering were simulated for each structure in water.

Results and Discussion

The Cu cores were synthesized by reducing the Cu precursor, Cu(acac)$_2$, in ODE at 220 ^{o}C in presence of TOP and OLAM. To improve the uniformity of the cores, a vapor of CO was generated *in situ* from the dehydration of formic acid by sulfuric acid and added to the reaction at 200 ^{o}C. The vapor also contained formic acid due to its high vapor pressure. **Figure 1A** shows a representative TEM image of the cubic Cu cores. The size distribution of the nanocubes was plotted in the histogram (**Fig. 1B**), indicating an average edge length of 28±3 nm. The inset and **Figure S1** shows the HRTEM of an individual nanoparticle with the lattice spacing corresponding to the *d* spacing of the {200} planes of the face-centered cubic (*fcc*) structure of Cu. To clarify the role of CO and formic acid in the synthesis, we performed the reaction under four different conditions: 1) no CO and formic acid, 2) CO alone, 3) formic acid vapor alone, and 4) both CO and formic acid vapor present. TEM characterization of the products from these reactions clearly shows that the presence of both CO and formic acid is important to improve the yield of cubic shape nanoparticles (**Fig. S2**). The reaction kinetics was followed by UV-vis spectroscopy based on the extinction peak at ~580 nm, which is due to the formation of Cu

nanoparticles turning the solution slightly red. (**Fig. S3**). The rate and extent of this color change from yellowish to red can be used to follow Cu nanoparticle formation at different reaction conditions. At 220 $^{\circ}$C, even without the addition of CO and formic acid, it takes approximately 10 minutes for the reaction to turn red, the introduction of either CO or formic acid or both do not appreciably change the kinetics. At 200 °C, compared to the flow of formic acid vapor, the flow of CO dramatically slows down the formation of Cu nanoparticles (**Fig. S4**). Although we could not completely rule out the possibility of the role of CO being a reducing agent, this result suggests that the reducing power of formic acid is far stronger than CO for Cu reduction. This is consistent with a previously published electrochemical study,[36] which showed that the reduction of Cu^{2+} to Cu^+ was very slow with CO under acidic conditions, indicating CO being a weak reducing agent for Cu synthesis, thus it may only serve as a capping agent[37].

The SiO_2 shells were then coated on the surface of the Cu cores by modifying our previously established W/O microemulsion method.[32] To prevent the dissolution of Cu nanoparticles during the sol-gel reaction, the catalyst NH_4OH used in our previous work was replaced by NaOH. The TOP capping is critical for passivating the surface of the Cu cores and protecting them from oxidation during the sol-gel process. The resulting core-shell nanostructures were imaged by TEM as shown in **Figure 1C**. The silica coating was uniform and the shell thickness was measured to be 4.6±0.8 nm. The optical spectra were measured before and after silica coating. Without the coating, the as-synthesized nanocubes were insoluble in water and therefore suspended in toluene, showing an LSPR peak at 581 nm with a shoulder at ~680 nm (**Fig. 1D, black line**). The shoulder could be attributed to the aggregation of the nanoparticles in toluene. In contrast, the optical spectrum of the core-shell nanoparticles suspended in aqueous solution

displays a sharp LSPR peak at 587 nm with no shoulder (**Fig. 1D, red line**), indicating the core-shell nanoparticles are well dispersed in aqueous solution.

The LSPR of the Cu-SiO$_2$ core-shell structures were further quantified by fitting to the Beer-Lambert Law. The optical spectra of the core-shell structure aqueous suspensions were taken at a series of dilutions as shown in **Figure 2A**. The absorbance at the LSPR maximum (587 nm) was plotted as a function of particle concentration (the inset of **Fig. 2A**). Based on the Beer-Lambert Law, the extinction coefficient of the suspension was determined to be 4.77×10^9 M^{-1}cm^{-1} from the linear fit of the plot. From the extinction coefficient and the average size of the nanocubes (i.e. edge length of 28 nm), the extinction cross section of an individual nanocube was estimated to be 7.92×10^{-16} m^2. To further analyze the optical properties, we calculated the optical spectra for individual nanoparticles suspended in water using the DDA method. Initially, the DDA simulation was performed using two geometries with the same volume: a cube with edge length of 30 nm and a sphere with diameter of 37 nm (**Fig. 2, B and C**). The cube exhibits an extinction peak at 600 nm while the sphere shows an extinction maximum at 560 nm. In both cases, the extinction spectra were dominated by the absorption component. Optical efficiency of the cube is approximately twice as high as the sphere with the simulated extinction cross section being 3.06×10^{-15} m^2 and 1.38×10^{-15} m^2, for the cube and sphere, respectively. Although there is a small difference between the experimental and simulated peak position and cross section, the differences can be explained by the slightly different sizes, shape, and the approximate nature of the experimental concentration measurement.
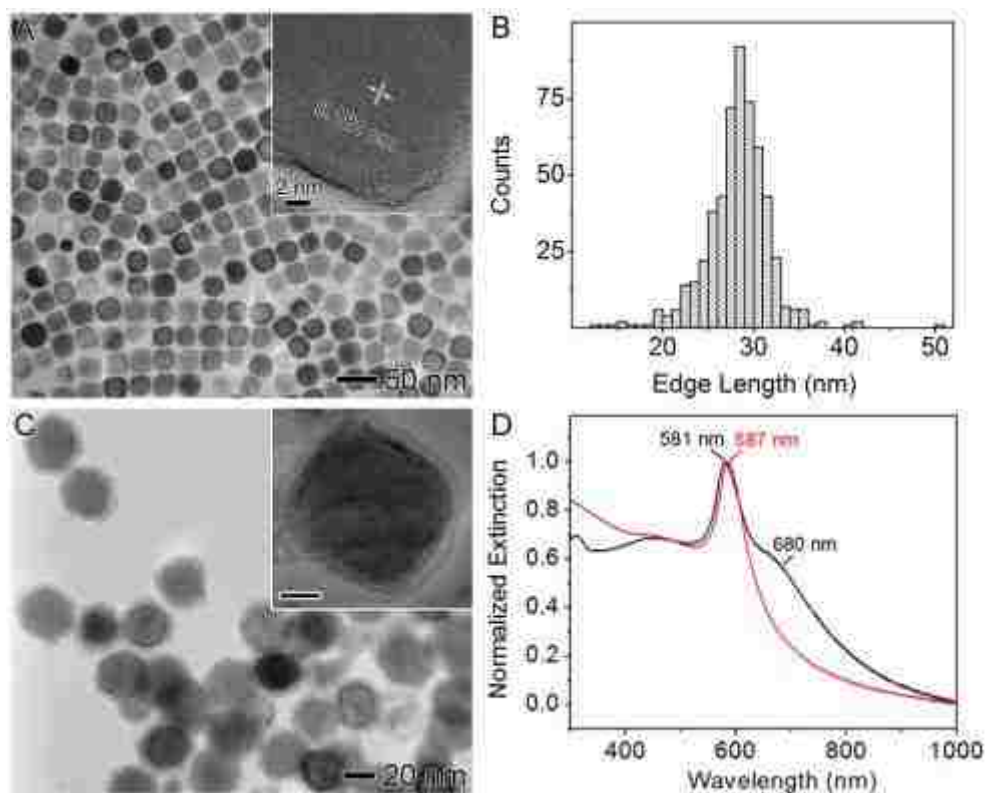
Figure 1. (A) TEM image of Cu nanocubes with edge length of 28±3 nm. The inset is the HRTEM of an individual nanocube taken from the [100] zone axis. (B) Histogram of size distribution of the sample in (A). The average edge length is 28±3 nm. (C) TEM image of SiO_2 coated Cu nanoparticles with coating thickness of 4.6±0.8 nm. The inset is the HRTEM image of an individual particle with the scale bar of 10 nm. (D) UV-vis spectra of sample (A) Cu nanocubes in toluene (black line) and sample (C) Cu-SiO_2 core-shell nanoparticles in aqueous solution (red line).

We anticipate that the shape deviations of the synthesized nanocube from a perfect cube with sharp corners have a large influence on both peak position and intensity. According to TEM characterization (**Fig. 1C**), the synthesized nanocubes lost part of their mass from the corner regions, and thus do not have sharp corners as in a perfect cube. We performed DDA simulations also on rounded cubic targets by removing up to 2 % of the total mass from a perfect cube at the corner regions. The spectra of the rounded cubes are shown in **Figure 2D**. It can be seen the peak position shifted by 14 nm by removing the sharp corners. The rounded cube has an extinction maximum close to 586 nm and is thus in perfect agreement with experiments (**Fig. 2A**). The simulation result indicates that the plasmon peak red shifts for nanocubes of the same volume when compared to corresponding nanospheres. The same shape effects on the plasmon maxima were observed for Au and Ag in the simulated spectra as shown in **Figure S5**. These simulation results are in agreement of the previous experimental study showing that shapes of similar sizes but with sharp corners and edges tend to have red shifted plasmon resonance[38]. For Cu, the shape induced red shift associated with the nanocubes thus shifting the plasmon resonance away from the interband transition of Cu material, leading to sharper plasmon bands.
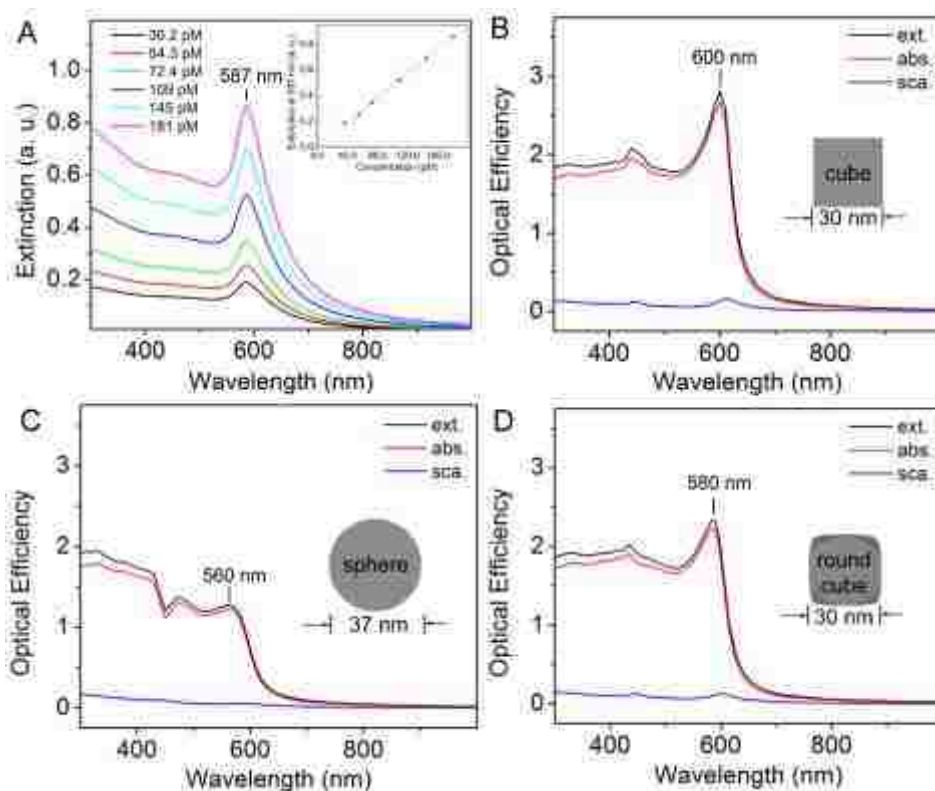
Figure 2. (A) UV-vis spectra of the Cu-SiO$_2$ core-shell nanoparticles at different concentrations. The inset is the plot of the extinction at LSPR maxima as a function of concentration. The red line is the linear fit of the data ($y = 4.77 \times 10^9 \, x$, $R^2 = 0.9998$). (B) DDA simulated spectra of an isolated Cu nanocube with an edge length of 30 nm. The inset is the schematic drawing of the cross section of the nanocube. (C) DDA simulated spectra of an isolated Cu nanosphere with the same volume as the nanocube in (B). The inset is the schematic drawing of the cross section of the nanosphere. (D) DDA simulated spectra of a rounded Cu nanocube with ~2% of the total mass of the nanocube in (B) removed from the corners. The inset shows the schematic drawing of the rounded nanocube viewed from the front. All simulated spectra were calculated using water as the medium.

80

We further examined the stability of the core-shell nanostructures in aqueous solution. The stability was assessed by both structural analysis using XRD and optical spectra using UV-vis. We obtained the XRD patterns of the core-shell nanoparticles before and after being stored for one month in aqueous solution as samples (a) and (b), respectively (**Fig. 3A**). The peaks at 43.3, 50.4, and 74.0 degree were indexed to {111}, {200}, and {220} planes of the face-centered cubic (*fcc*) Cu, confirming that the core-shell nanostructures contain pure Cu. There is no change in the XRD patterns in sample (b) when compared to sample (a), suggesting that no obvious oxidation occurred in the core-shell nanostructures during the one month storage. The UV-vis spectra showed a sharp LSPR peak of Cu at 585 nm and remained unchanged before and after storage (**Fig. 3B**). These results indicate that the Cu cores are well protected by the SiO_2 shell from oxidation and agglomeration.
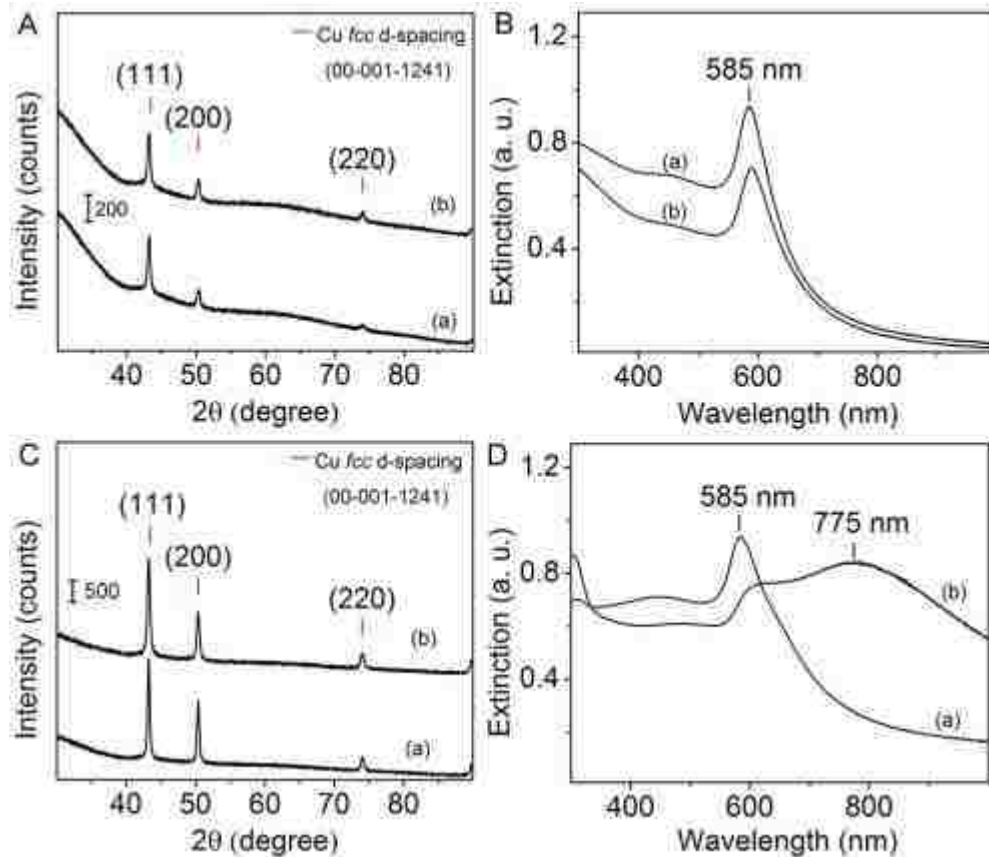
Figure 3. (A, B) Characterization of the Cu-SiO$_2$ core-shell nanostructures suspended in aqueous solution: (A) XRD patterns; and (B) UV-vis spectra. (C, D) Characterization of TOP-capped Cu nanocubes suspended in toluene: (C) XRD patterns; and (D) UV-vis spectra. In all panels, (a) and (b) represent the samples before and after 1-month storage, respectively.

The use of TOP-capped Cu nanoparticles is critically important for the successful synthesis of well-dispersed Cu-SiO$_2$ core-shell nanoparticles with sharp and stable LSPR. TOP serves as a capping agent to protect Cu nanoparticles from oxidation during the sol-gel reactions. We examined the stability of TOP-capped nanoparticles of Cu by the XRD and UV-vis analysis before and after storage for a month in toluene. The XRD patterns before and after the storage were essentially the same, indexed to *fcc* Cu, showing no peaks from oxides (**Fig. 3C**). We also performed the XRD analysis on the solid sample after storage for six months. Compared to the XRD result prior to the storage, the XRD pattern essentially has no changes, indicating that no obvious oxidation after the solid sample has been stored for six months (**Fig. S6**). However, significant changes were found in the optical spectra of TOP-capped nanoparticles in toluene between before and after storage as shown in **Figure 3D**. The initial sharp extinction peak at 585 nm red-shifted to ~600 nm with reduced intensity and a broad shoulder centered at 775 nm arose in the optical spectrum after the TOP-capped nanoparticles were stored for a month. Since the XRD results showed no sign of oxidation, the spectral change is likely due to the particle agglomeration in solution.

It is known that the agglomeration of TOP-capped nanoparticles is much more severe without sonication. We monitored the spectral changes of TOP-capped nanoparticles in toluene over 15 min at a 100-fold dilution (~100 pM) compared to the typical concentration for storage (**Fig. 4A**). Two peaks, 595 and 700 nm, were observed in the initial spectrum, which was taken 1 h after the reaction was completed. The 590-nm peak can be attributed to individual nanoparticles while the 700-nm peak belongs to the nanoparticle agglomerates. Over the course of 15 min after dilution, the 700-nm peak became broader and shifted to the red to ~800 nm, suggesting the increased numbers of agglomerates. These results were verified by the DLS

measurements on the corresponding time course samples (**Fig. 4, B-D**). Two populations with different hydrodynamic diameters (HD) were observed: the one with HD <100 nm assigned to individual nanoparticles and the other with HD between 300-500 nm assigned to nanoparticle agglomerates. By comparing **Figure 4, B-D**, the relative percentage of nanoparticle agglomerates increased over time. The nanoparticle agglomeration was further confirmed by TEM as shown in the inset of **Figure 4D**. Each particle cluster seen in the TEM images contains about 10-20 TOP-capped nanoparticles. The agglomeration of TOP-capped nanoparticles stems from the hydrophobic interaction among long carbon chains of the TOP molecules attached to the particle surface in toluene.[20]
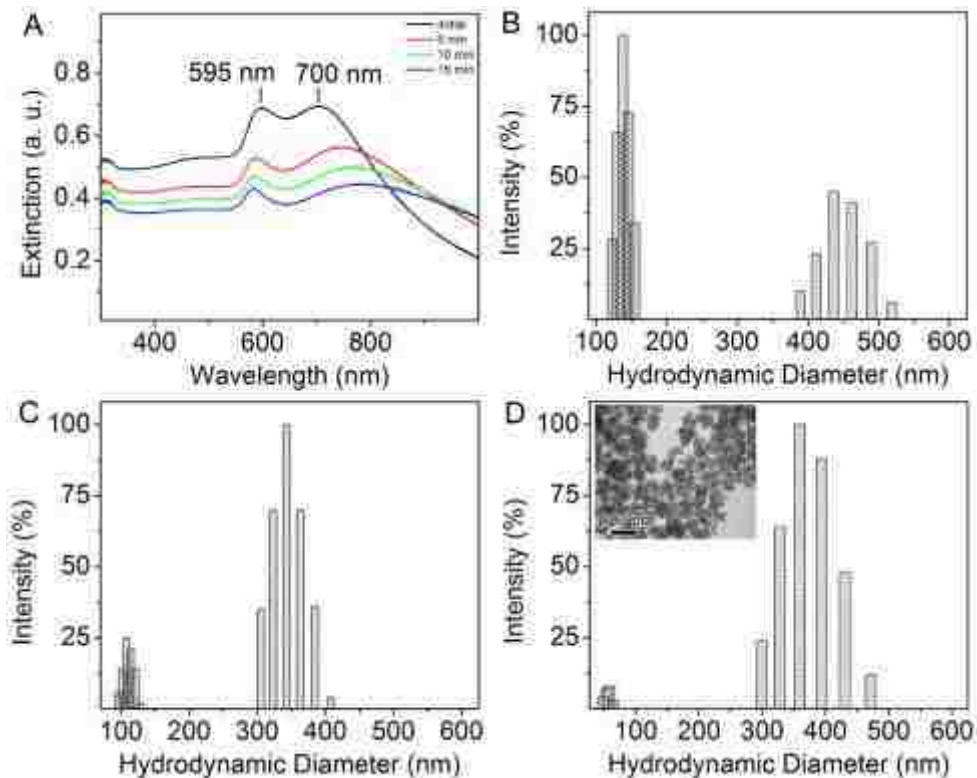

Figure 4. (A) Optical spectra of diluted Cu nanoparticles in toluene over time; and (B-D) DLS data of the corresponding sample in (A) measured at the time of initial, 5 min, and 15 min.

Although TOP can protect the capped Cu nanoparticles from oxidation, the TOP-capped nanoparticles tend to agglomerate in toluene. Once the agglomerates form in toluene, it is difficult to separate them into individual nanoparticles using mechanical methods, such as sonication. This tendency led us to investigate the effect of agglomeration on the formation of the core-shell nanostructures. The SiO_2 coating process of the TOP-capped nanoparticle agglomerates was monitored over time using UV-vis spectroscopy. **Figure 5** shows the extinction spectra of the aliquots taken from the reaction mixture during the sol-gel reaction. During the SiO_2 coating, the broad peak at ~800 nm indicative of particle agglomeration gradually decreased and eventually disappeared as the reaction progresses to completion. The peak at 580 nm increased in intensity and became prominent as the reaction proceeded. This spectral evolution suggests that the agglomerates could be completely disassembled into individual particles and coated with SiO_2 during the sol-gel process in microemulsion. As a control experiment, we have performed the microemulsion in the absence of sol-gel precursor TEOS and found individual particles along with aggregates in the microemulsion as shown in the TEM images (**Fig. S7**) and DLS measurements (**Fig. S8**). With the silica precursors, the individual particles are coated and prevented from joining the aggregates, thus shifting the equilibrium.
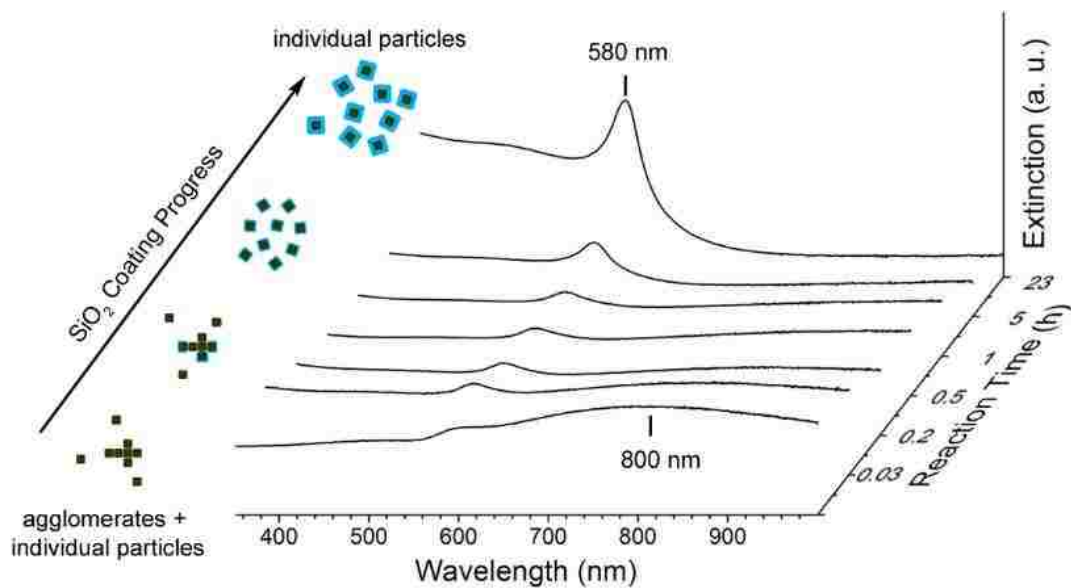
Figure 5. Spectral evolution of the time-course study on the SiO$_2$ coating process of the Cu nanoparticles.

Our study shows that the TOP-mediated sol-gel process in a W/O microemulsion can be used to break apart particle assemblies and allow good dispersity of individual nanoparticles in aqueous solution, using the SiO_2 coating as a physical barrier. The TOP-capped nanostructure samples often display a broad LPSR band between 600-900 nm which could be attributed to nanoparticle agglomeration or the size distribution (i.e. possibly containing rods). This silica coating method could be used to recover the spectral signatures of different nanostructures thus qualitatively determining composition of shapes (i.e. nanoparticle versus nanorod) in the sample without costly TEM imaging. It can provide us a rapid screening method of the product for shape-controlled synthesis. To demonstrate the feasibility, we applied the microemulsion method to coat SiO_2 on a mixture sample containing nanorods. A mixture of Cu nanocubes and nanorods was synthesized when in situ generated CO from the dehydration of formic acid by sulfuric acid was added to the reaction at a lower temperature. Based on the previous report by Murphy and co-workers[39], rod growth is promoted in a relatively-weaker reducing environment. In our case, the slower reduction kinetics at lower temperature compared to that used for the cube synthesis increases the yield of nanorods. **Figure 6A** shows the TEM image of the mixture sample with the histogram plots in **Figure S9**, indicating a composition of ~80% nanocubes with an average edge length of ~40 nm and ~20% nanorods with an average of 2.5 aspect ratio (~36 × 90 nm). The UV-vis spectrum shows a broad peak at 615 nm with a shoulder at 700 nm (**Fig. 6B**) which is similar to the spectrum of nanoparticle agglomerates (**Fig. 4A**). This particle suspension was then added into hexane, followed by the addition of Igepal CO-520, TEOS, and NaOH solution to create a microemulsion environment for the sol-gel process. After the sol-gel process, the nanostructures were coated by SiO_2 as seen in the TEM image (**Fig. 6C and S10**) with a mostly uniform shell and the sample is well-dispersed in aqueous solution. As predicted, the UV-vis

spectrum of the sample in water exhibits two distinct peaks at 578 nm and 700 nm (**Fig. 6D**), corresponding to the rounded nanocubes and nanorods, respectively. When the reaction is monitored by UV-vis spectroscopy (**Fig. 6E**), the extinction peaks of the nanocubes and nanorods clearly arise as the coating process proceeds. During the coating process, the peak at 700 nm was gradually recovered while the peak at 615 nm shifted to the blue, indicating that the nanostructure agglomerates were separated to yield individual nanostructures. After coating with SiO_2, the nanorods could potentially be separated from the nanoparticles based on their difference in mass using centrifugation.[40-41]
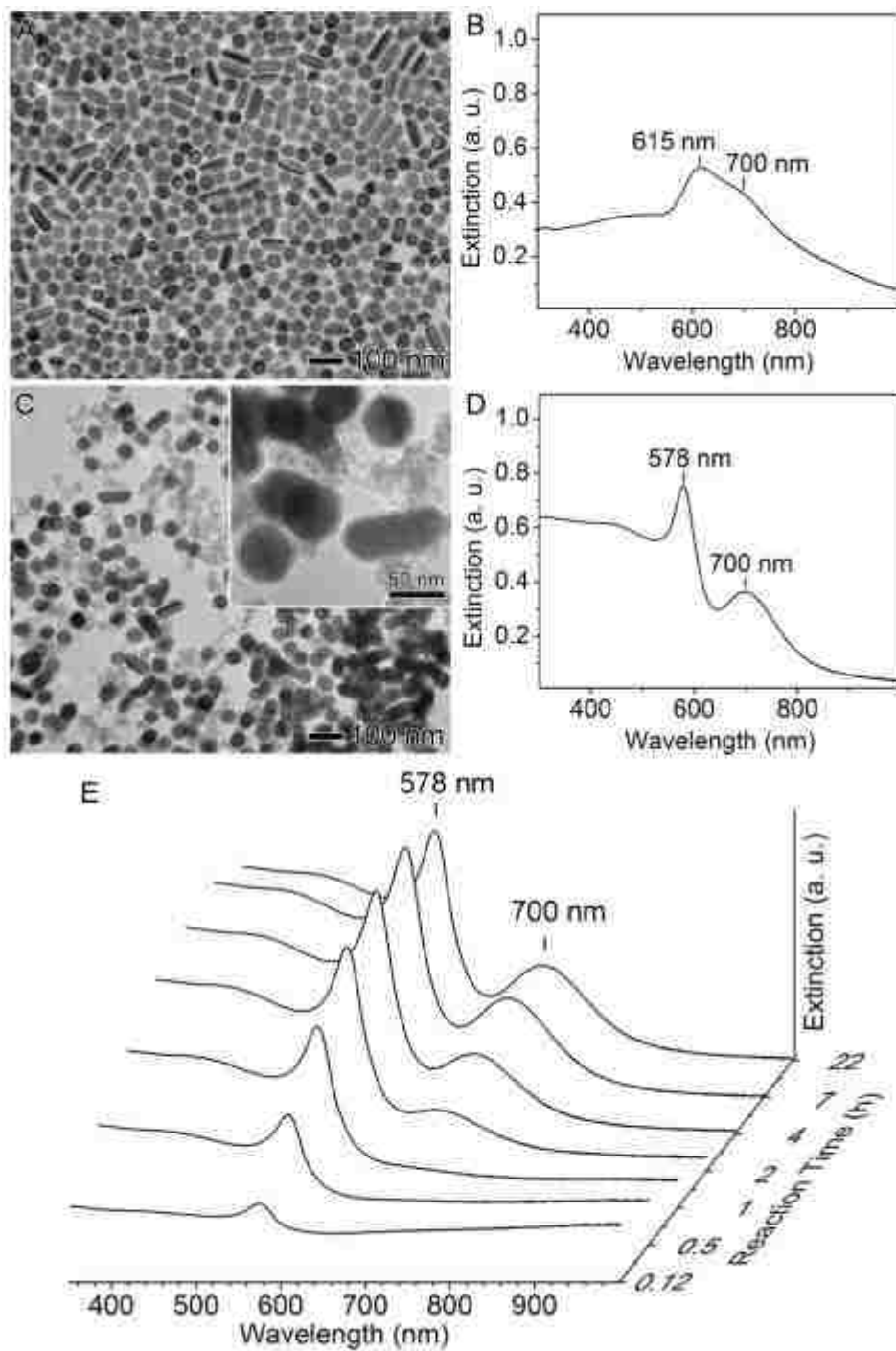
Figure 6. (A, B) Characterization of the as-synthesized mixture of Cu nanocubes and nanorods: (A) TEM image; and (B) UV-vis spectrum of the particle suspension in toluene. (C, D) Characterization of the mixture sample after silica coating process: (C) TEM image with a magnified view in the inset; and (D) UV-vis spectrum of the particle suspension in water. (E) Spectral evolution of the mixture over time during the silica coating process.

The spectral shifts due to the nanorods with different aspect ratios were further analyzed by DDA simulations. The simulations were performed on nanorods with a diameter of 37 nm. As shown in **Figure 7, A and B**, the nanorods with aspect ratios of 2:1 and 3:1 possesses extinction peaks at 640 nm and 770 nm, respectively. The relative ratio of absorption to scattering was compared based on the optical efficiency which is the ratio of the optical cross-section to the physical cross-section of a nanoparticle. The efficiency of absorption is twice that of scattering for the nanorod with aspect ratio of 2:1, but becomes comparable to the scattering efficiency for the nanorod with aspect ratio of 3:1. **Figure 7C** shows the extinction peaks of nanospheres (1:1) and nanorods with aspect ratios from 2:1 to 3:1 and 4:1 increase from 560 nm to 641, 773, and 931 nm. The extinction peaks of nanorods further increase to 1097 and 1263 nm for aspect ratios of 5:1 and 6:1, respectively. Similar to that of the Au and Cu_3Au nanorods,[42-43] the peak positions for the extinction spectra were proportional to aspect ratios of the nanorods, as plotted in **Figure 7D**. A linear least square fitting of the peak position and the aspect ratio gives a Pearson R^2 of 0.997 showing good linearity ($y = 313.8 + 156.8x$). Such a good fit allows the aspect ratio of the synthesized nanorods to be determined by examining the position of the LSPR maximum. Our UV-vis shows the sharp peak at 700 nm, which is consistent with an aspect ratio of 2.5:1. This result agreed well with the aspect ratio of 2.5 estimated from analyzing the TEM image.
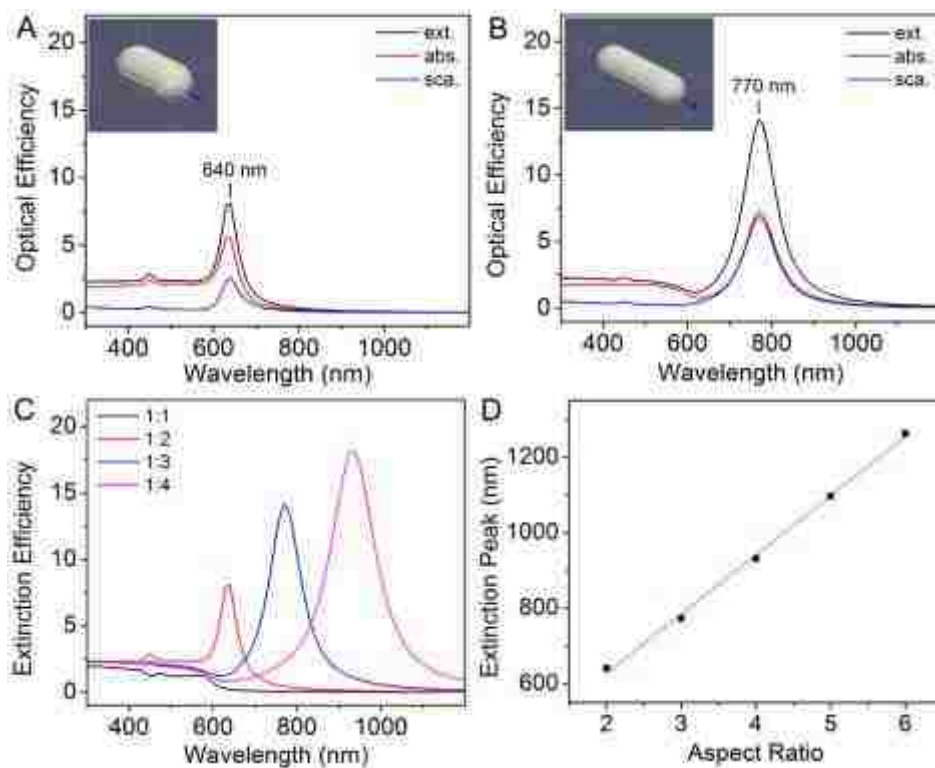
Figure 7. Simulated optical spectra of Cu nanorods with two different aspect ratios suspended in water: (A) 37 × 74 nm and (B) 37 × 112 nm. (C) Extinction spectra of Cu nanorods with a fixed width of 37 nm but different aspects: 1:1 (black), 2:1 (red), 3:1 (blue), and 4:1 (purple). (D) The position of the extinction peak as a function of the aspect ratio for the Cu nanorods shows excellent linearity. The red line ($y = 313.8 + 156.8x$, $R^2 = 0.997$) is a linear least square fit of the simulated peak positions.

The SiO$_2$ shell thickness could be varied by adjusting the reaction time of the sol-gel process. In our study, the sol-gel process is typically allowed to proceed for 24 h, yielding a shell thickness of ~5 nm. It is possible to coat the Cu cores with a shell thickness less than 5 nm; however, it would be difficult to image a thinner shell on the Cu core. Alternatively, the core-shell nanoparticles could be treated by 0.3 mM FeCl$_3$ for 10 min to etch the Cu cores, resulting in hollow SiO$_2$ shell for imaging (**Fig. S11**). Thicker shells could be generated by increasing the sol-gel reaction time, as shown in **Figure 8**. The shell thickness was ~5 nm at 24 h and increased to ~10 nm at 72 h. increased shell thickness does not show appreciable changes on the LSPR peak. The HRTEM images show that both the thinner shell (**inset of Fig. 8A**) and the thicker shell (**Fig. 8C**) are mostly uniform and discrete. We note with the increased thickness the amount of excess silica also increases. The UV-vis spectra of the samples in aqueous solution depicts extinction maximum at ~580 nm (**Fig. 8D**). Thus the insensitivity of the optical spectra with thickness indicates that the excess silica does not influence the optical properties and the different thickness also have negligible effect on the peak locations due to the porous nature of the silica coating. The amount of red shift is within the margin of error. As shown previously by Liz-Marzán and co-worker with silica coating on Au and Ag,[23, 26] it is indeed possible that a systematic red shift can be observed with even thicker coating which can be optimized for Cu in future studies. In this work, we demonstrate for the first time that Cu nanoparticles having superior optical properties can indeed be produced in aqueous solution.
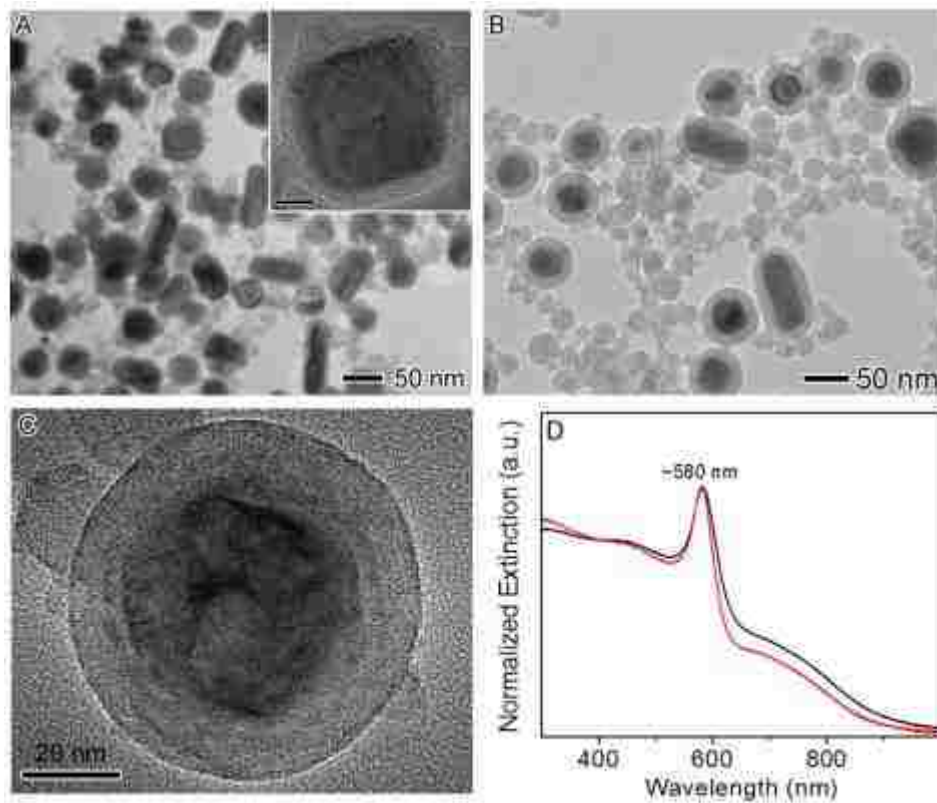
Figure 8. (A-C) TEM characterization of the SiO_2 coated Cu nanoparticles synthesized by different reaction time: (A) 24 h (HRTEM in the inset); (B) 72 h; and (C) HRTEM of an individual particle in the 72-h sample (B). (D) UV-vis spectra of the particles suspended in water corresponding to the sample (A) in black line and the sample (B) in red line.

Conclusions

A TOP-mediated, sol-gel process in a microemulsion was successfully developed to produce Cu-SiO$_2$ core-shell nanoparticles that were well dispersed in water. The SiO$_2$ coating acts as a protective layer to prevent oxidation of Cu, thus preserving the superior LSPR properties of Cu nanoparticles in aqueous solution. The cubic nanoparticles synthesized in this work exhibit a narrow and intense LSPR peak at ~590 nm while the nanorods possess an LSPR peak at 700 nm and aspect ratio of 2.5:1. Unlike spherical nanoparticles, the LSPR of the nanocubes and the longitudinal mode of nanorods are narrow and intense due to the shape effect red shifting of the LSPR from the interband transitions of Cu. These experimental results match well with the DDA numerical simulations. These aqueous Cu-SiO$_2$ core-shell nanostructures may find use in sensing, catalysis, and antimicrobial applications. The ligand-mediated microemulsion sol-gel method may provide a versatile approach to spontaneously disperse ligand-induced nanoparticle agglomerates and recover the individual particle dispersion for various applications in aqueous environments.

SUPPLEMENTAL INFORMATION

HRTEM image and analysis of the nanocubes; TEM images of the Cu nanoparticles synthesized at different conditions; UV-vis spectra and photographs of time course study for the Cu nanoparticle synthesis; DDA simulation of the extinction spectra of a cube, a rounded cube, and a sphere for Cu, Au, and Ag; XRD pattern of the solid TOP-capped nanoparticles; TEM images, DLS and UV-vis measurements of the time course study for the microemulsion without TEOS; Histograms of the size distribution of the mixture sample of nanocubes and nanorods; the close-up view of the core-shell nanostructures; and TEM image of the hollow SiO$_2$ shells.

ACKNOWLEDGEMENT

References

1. Hartland, G. V.; Schatz, G., Virtual Issue: Plasmon Resonances - A Physical Chemistry Perspective. *J. Phys. Chem. C* **2011,** *115* (31), 15121-15123.

2. Kelly, K. L.; Coronado, E.; Zhao, L. L.; Schatz, G. C., The Optical Properties of Metal Nanoparticles: The Influence of Size, Shape, and Dielectric Environment. *J. Phys. Chem. B* **2003,** *107* (3), 668-677.

3. Lal, S.; Link, S.; Halas, N. J., Nano-optics from sensing to waveguiding. *Nat. Photon.* **2007,** *1* (11), 641-648.

4. Willets, K. A.; Van Duyne, R. P., Localized surface plasmon resonance spectroscopy and sensing. *Annu. Rev. Phys. Chem.* **2007,** *58*, 267-297.

5. Schwartzberg, A. M.; Zhang, J. Z., Novel Optical Properties and Emerging Applications of Metal Nanostructures. *J. Phys. Chem. C* **2008,** *112* (28), 10323-10337.

6. Dreaden, E. C.; Alkilany, A. M.; Huang, X.; Murphy, C. J.; El-Sayed, M. A., The golden age: gold nanoparticles for biomedicine. *Chem. Soc. Rev.* **2012,** *41* (7), 2740-2779.

7. Yang, X.; Yang, M.; Pang, B.; Vara, M.; Xia, Y., Gold nanomaterials at work in biomedicine. *Chem. Rev.* **2015,** *115* (19), 10410-10488.

8. Linic, S.; Aslam, U.; Boerigter, C.; Morabito, M., Photochemical transformations on plasmonic metal nanoparticles. *Nat. Mater.* **2015,** *14* (6), 567-576.

9. Vollmer, M.; Kreibig, U., Optical properties of metal clusters. *Springer Ser. Mat. Sci* **1995,** *25*.

10. Chan, G. H.; Zhao, J.; Hicks, E. M.; Schatz, G. C.; Van Duyne, R. P., Plasmonic properties of copper nanoparticles fabricated by nanosphere lithography. *Nano Lett.* **2007,** *7* (7), 1947-1952.

11. Wang, H.; Tam, F.; Grady, N. K.; Halas, N. J., Cu nanoshells: effects of interband transitions on the nanoparticle plasmon resonance. *J. Phys. Chem. B* **2005,** *109* (39), 18218-18222.

12. Sundararajan, S. P.; Steele, J. M.; Halas, N. J., Propagation of surface plasmons on Ag and Cu extended one-dimensional arrays on silicon substrates. *Appl. Phys. Lett.* **2006,** *88* (6), 063115.

13. Guo, X.; Hao, C.; Jin, G.; Zhu, H. Y.; Guo, X. Y., Copper nanoparticles on graphene support: an efficient photocatalyst for coupling of nitroaromatics in visible light. *Angew. Chem. Int. Ed.* **2014,** *53* (7), 1973-1977.

14. Kanninen, P.; Johans, C.; Merta, J.; Kontturi, K., Influence of ligand structure on the stability and oxidation of copper nanoparticles. *J. Colloid Interface Sci.* **2008,** *318* (1), 88-95.

15. Meng, F.; Jin, S., The solution growth of copper nanowires and nanotubes is driven by screw dislocations. *Nano Lett.* **2011,** *12* (1), 234-239.

16. Pacioni, N. L.; Filippenko, V.; Presseau, N.; Scaiano, J., Oxidation of copper nanoparticles in water: mechanistic insights revealed by oxygen uptake and spectroscopic methods. *Dalton Trans.* **2013,** *42* (16), 5832-5838.

17. Lee, Y.; Choi, J.-r.; Lee, K. J.; Stott, N. E.; Kim, D., Large-scale synthesis of copper nanoparticles by chemically controlled reduction for applications of inkjet-printed electronics. *Nanotechnology* **2008,** *19* (41), 415604.

18. Jeong, S.; Woo, K.; Kim, D.; Lim, S.; Kim, J. S.; Shin, H.; Xia, Y.; Moon, J., Controlling the thickness of the surface oxide layer on Cu nanoparticles for the fabrication of conductive structures by ink-jet printing. *Adv. Funct. Mater.* **2008,** *18* (5), 679-686.

19. Hwang, H.-J.; Chung, W.-H.; Kim, H.-S., In situ monitoring of flash-light sintering of copper nanoparticle ink for printed electronics. *Nanotechnology* **2012,** *23* (48), 485205.

20. Ye, E.; Zhang, S. Y.; Liu, S.; Han, M. Y., Disproportionation for Growing Copper Nanowires and their Controlled Self-Assembly Facilitated by Ligand Exchange. *Chemistry– A European J.* **2011,** *17* (11), 3074-3077.

21. Yang, H.-J.; He, S.-Y.; Chen, H.-L.; Tuan, H.-Y., Monodisperse Copper Nanocubes: Synthesis, Self-Assembly, and Large-Area Dense-Packed Films. *Chem. Mater.* **2014,** *26* (5), 1785-1793.

22. Guerrero-Martínez, A.; Pérez-Juste, J.; Liz-Marzán, L. M., Recent progress on silica coating of nanoparticles and related nanomaterials. *Adv. Mater.* **2010,** *22* (11), 1182-1195.

23. Liz-Marzán, L. M.; Giersig, M.; Mulvaney, P., Synthesis of nanosized gold− silica core− shell particles. *Langmuir* **1996,** *12* (18), 4329-4335.

24. Ung, T.; Liz-Marzán, L. M.; Mulvaney, P., Controlled Method for Silica Coating of Silver Colloids. Influence of Coating on the Rate of Chemical Reactions. *Langmuir* **1998,** *14* (14), 3740-3748.

25. Mine, E.; Yamada, A.; Kobayashi, Y.; Konno, M.; Liz-Marzán, L. M., Direct coating of gold nanoparticles with silica by a seeded polymerization technique. *J. Colloid Interface Sci.* **2003,** *264* (2), 385-390.

26. Kobayashi, Y.; Katakami, H.; Mine, E.; Nagao, D.; Konno, M.; Liz-Marzán, L. M., Silica coating of silver nanoparticles using a modified Stöber method. *J. Colloid Interface Sci.* **2005,** *283* (2), 392-396.

27. Pastoriza-Santos, I.; Pérez-Juste, J.; Liz-Marzán, L. M., Silica-Coating and Hydrophobation of CTAB-Stabilized Gold Nanorods. *Chem. Mater.* **2006,** *18* (10), 2465-2467.

28. Yao, Q.; Lu, Z.-H.; Zhang, Z.; Chen, X.; Lan, Y., One-pot synthesis of core-shell Cu@ SiO2 nanospheres and their catalysis for hydrolytic dehydrogenation of ammonia borane and hydrazine borane. *Sci. Rep.* **2014,** *4*, 7597.

29. Doremus, R.; Kao, S.-C.; Garcia, R., Optical absorption of small copper particles and the optical properties of copper. *Appl. Optics* **1992,** *31* (27), 5773-5778.

30. Yeshchenko, O. A.; Dmitruk, I. M.; Dmytruk, A. M.; Alexeenko, A. A., Influence of annealing conditions on size and optical properties of copper nanoparticles embedded in silica matrix. *Mater. Sci. .Eng.: B* **2007,** *137* (1), 247-254.

31. Yeshchenko, O. A.; Dmitruk, I. M.; Alexeenko, A. A.; Dmytruk, A. M., Size-dependent melting of spherical copper nanoparticles embedded in a silica matrix. *Phys. Rev. B* **2007,** *75* (8), 085434.

32. Crane, C. C.; Tao, J.; Wang, F.; Zhu, Y.; Chen, J., Mask-assisted seeded growth of segmented metallic heteronanostructures. *J. Phys. Chem. C* **2014,** *118* (48), 28134-28142.

33. Draine, B. T.; Flatau, P. J., Discrete-dipole approximation for periodic targets: theory and tests. *JOSA A* **2008,** *25* (11), 2693-2703.

34. Draine, B. T.; Flatau, P. J., User guide for the discrete dipole approximation code DDSCAT 7.3. *arXiv preprint arXiv:1305.6497* **2013**.

35. Johnson, P. B.; Christy, R.-W., Optical constants of the noble metals. *Phys. Rev. B* **1972,** *6* (12), 4370.

36. Konnik, E., Electrochemical Oxidation of Carbon Monoxide in Aqueous Solutions. *Russian Chem. Rev.* **1973,** *42* (2), 111.

37. Vollmer, S.; Witte, G.; Wöll, C., Determination of site specific adsorption energies of CO on copper. *Catalysis Lett.* **2001,** *77* (1-3), 97-101.

38. Mock, J. J.; Barbic, M.; Smith, D. R.; Schultz, D. A.; Schultz, S., Shape effects in plasmon resonance of individual colloidal silver nanoparticles. *J. Chem. Phys.* **2002,** *116* (15), 6755-6759.

39. Orendorff, C. J.; Murphy, C. J., Quantitation of metal content in the silver-assisted growth of gold nanorods. *J. Phys. Chem. B* **2006,** *110* (9), 3990-3994.

40. Ibisate, M.; Zou, Z.; Xia, Y., Arresting, fixing, and separating dimers composed of uniform silica colloidal spheres. *Adv. Funct. Mater.* **2006,** *16* (12), 1627.

41. Sharma, V.; Park, K.; Srinivasarao, M., Shape separation of gold nanorods using centrifugation. *Proc. Nat. Acad. Sci.* **2009,** *106* (13), 4981-4985.

42. Link, S.; Mohamed, M.; El-Sayed, M., Simulation of the optical absorption spectra of gold nanorods as a function of their aspect ratio and the effect of the medium dielectric constant. *J. Phys. Chem. B* **1999,** *103* (16), 3073-3077.

43. Chen, S.; Jenkins, S. V.; Tao, J.; Zhu, Y.; Chen, J., Anisotropic seeded growth of Cu–M (M= Au, Pt, or Pd) bimetallic nanorods with tunable optical and catalytic properties. *J. Phys. Chem. C* **2013,** *117* (17), 8924-8932.
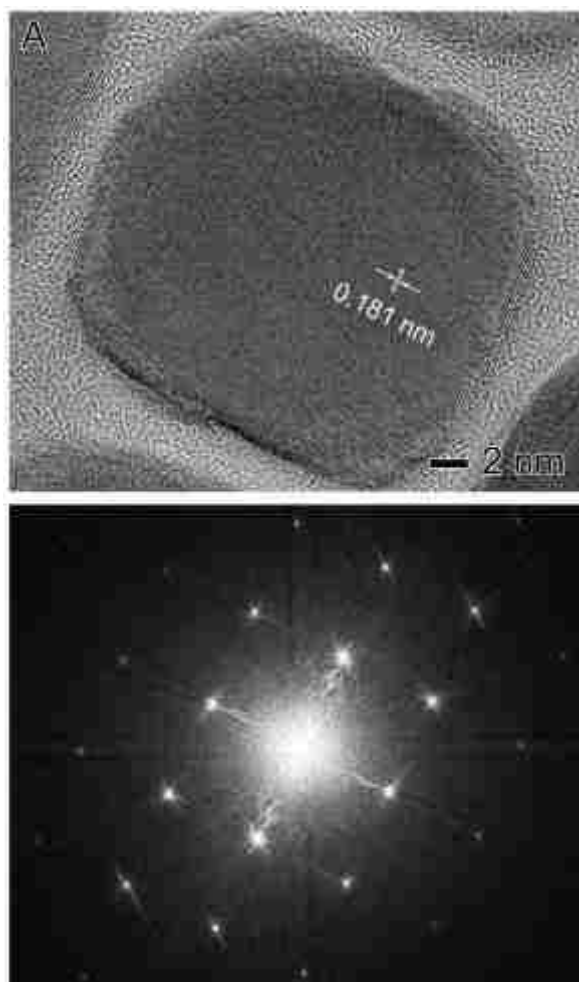
Figure S1. (A) HRTEM of a representative cubic nanoparticle; and (B) fast Fortier transform (FFT) of the HRTEM image in (A).

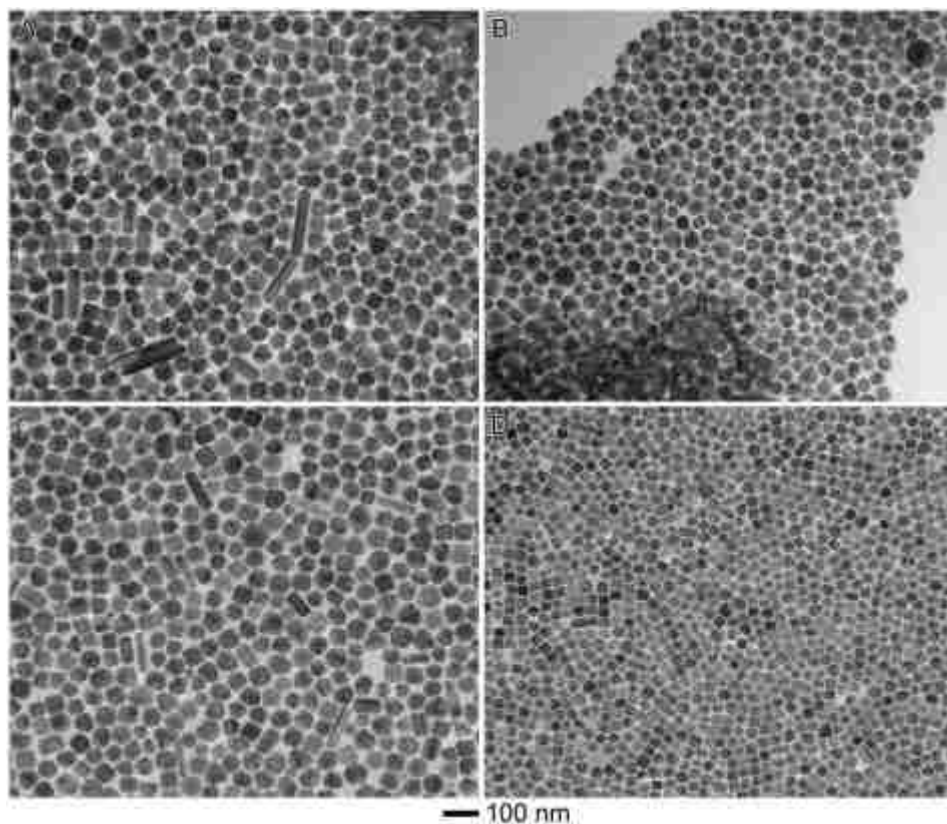**Figure S2.** TEM characterization of the Cu nanoparticles synthesized by reducing Cu(acac)$_2$ at 220 $^{\circ}$C at four different conditions: (A) no CO and formic acid; (B) CO alone (99.9% gas); (C) formic acid vapor alone (flown with Ar); (D) in the presence of both CO (99.9% gas) and formic acid vapor.
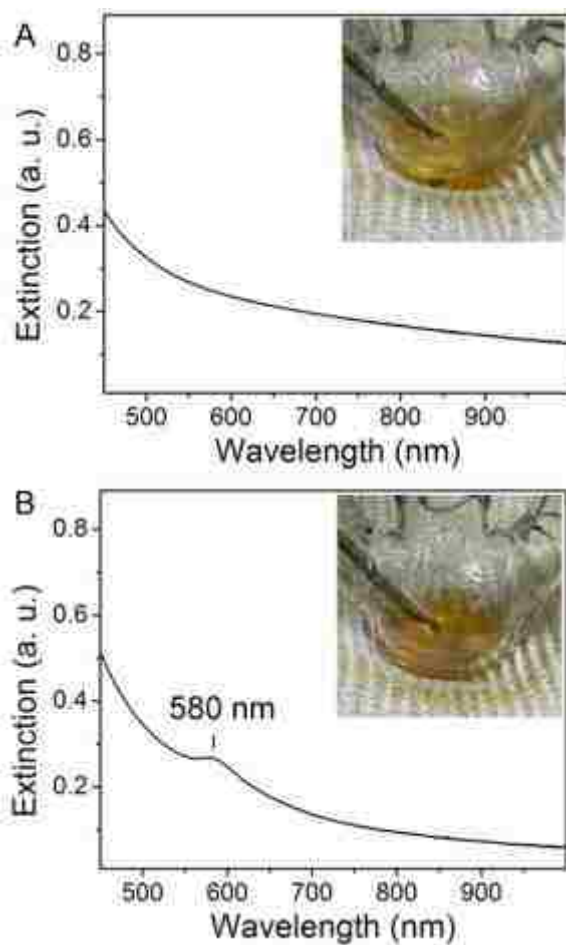
Figure S3. UV-vis spectra before (A) and after (B) Cu nanoparticles started to formed as indicating by the peak at ~580 nm corresponding to the LSPR of Cu nanoparticles. The insets show the color change of the reaction mixture from yellowish for the sample in (A) to slightly red for the sample in (B).
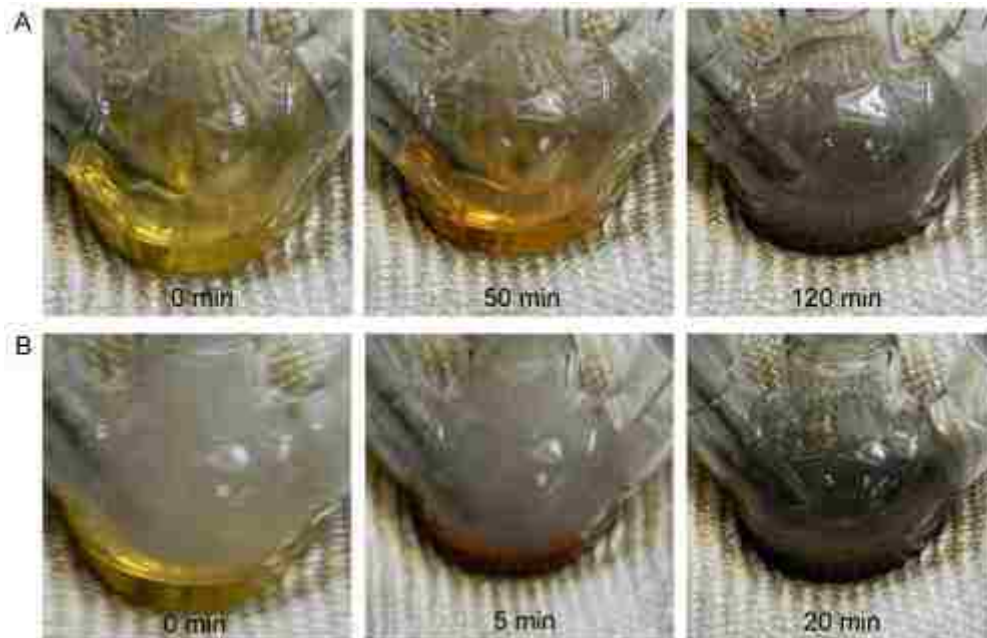
Figure S4. Photographs at different points for reactions of Cu nanoparticle synthesis at 200 $^\circ$C under different conditions: (A) under the flow of CO (99.9%); and (B) under the flow of formic acid vapor in Ar.
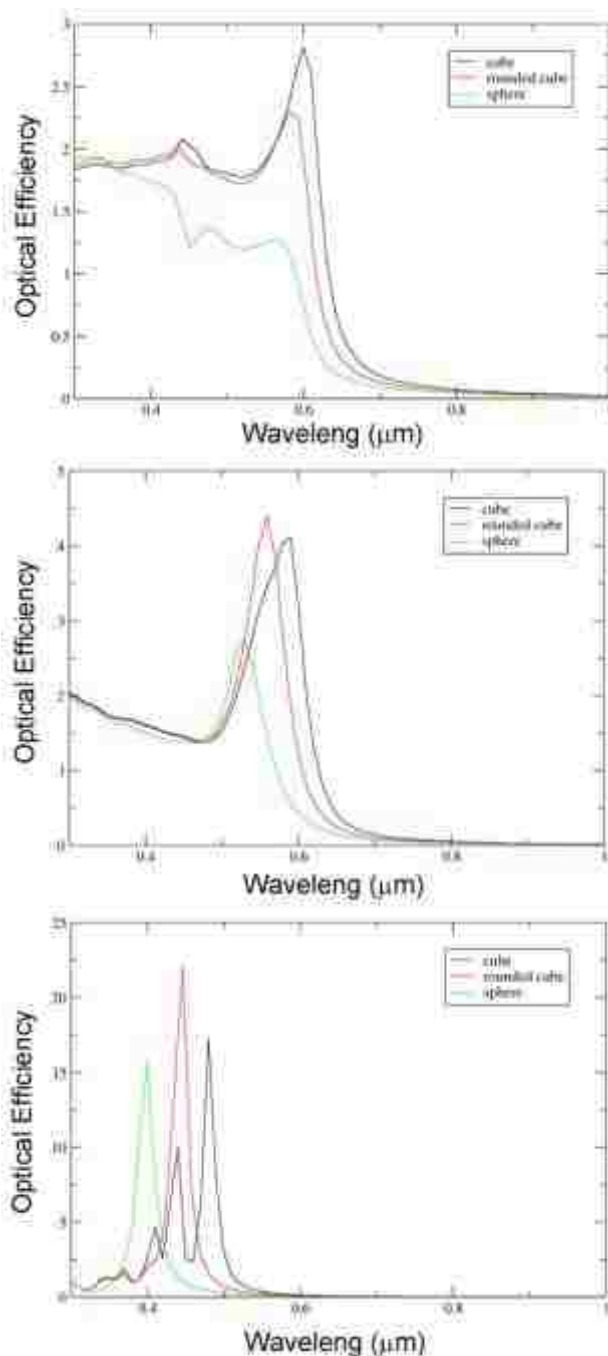
Figure S5. DDA simulation of the extinction spectra of a cube (black), a rounded cube (red), and a sphere (green) with the same volume for different materials: (A) Cu; (B) Au; and (C) Ag, indicating the red shifts of the main LSPR peak position as a sphere turns into a cube. For Cu, the peak shifts from ~560 nm (sphere), to ~585 nm (rounded cube) and ~600 nm (cube). For Au, the peak shifts from ~530 nm (sphere), to ~560 nm (rounded cube) and ~590 nm (cube). For Ag, the peak shifts from ~400 nm (sphere), to ~447 nm (rounded cube) and ~481 nm (cube).
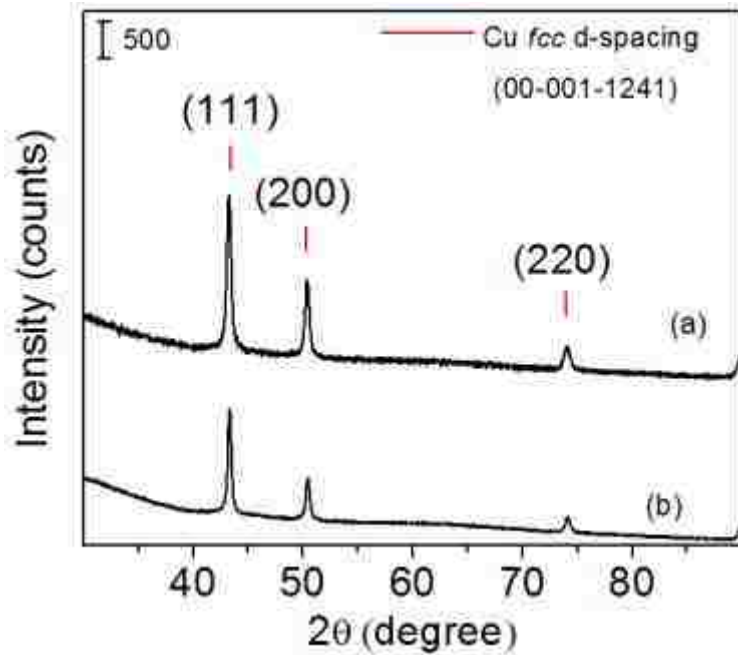
Figure S6. XRD patterns of the TOP-capped nanoparticle sample in Figure 3C in the solid state before (a) and after (b) storage of six months.
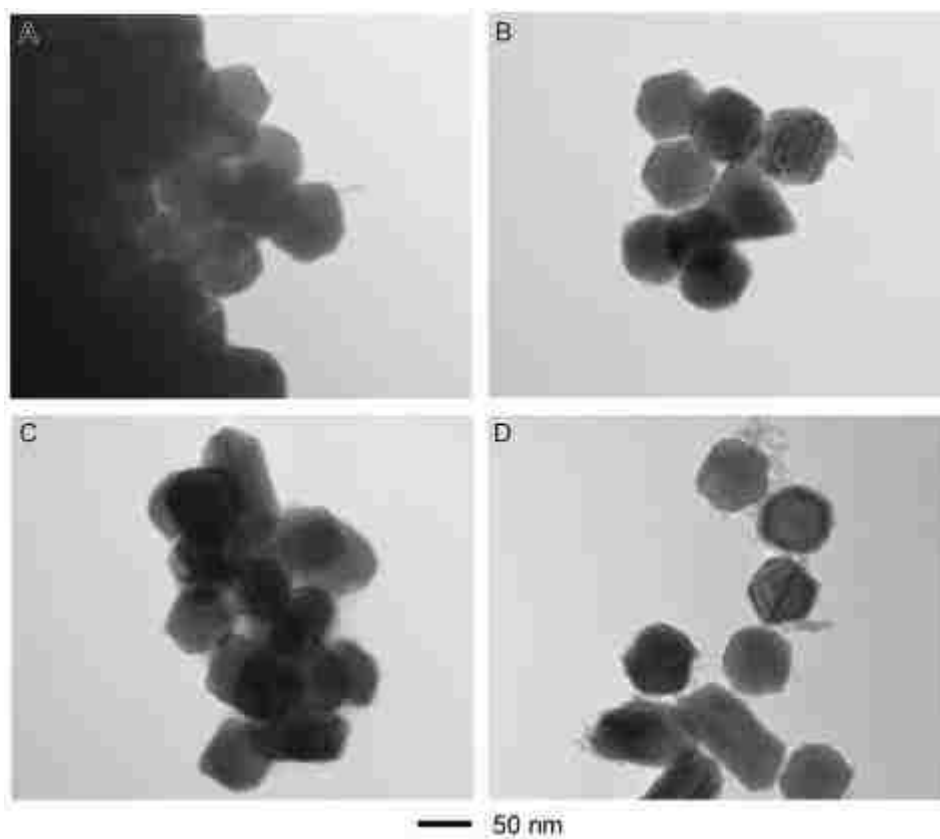
Figure S7. TEM images of the aliquots from the microemulsion in the absence of TEOS at different time points: (A) 6 h, (B) 15 h, (C) 24 h, and (D) 48 h.
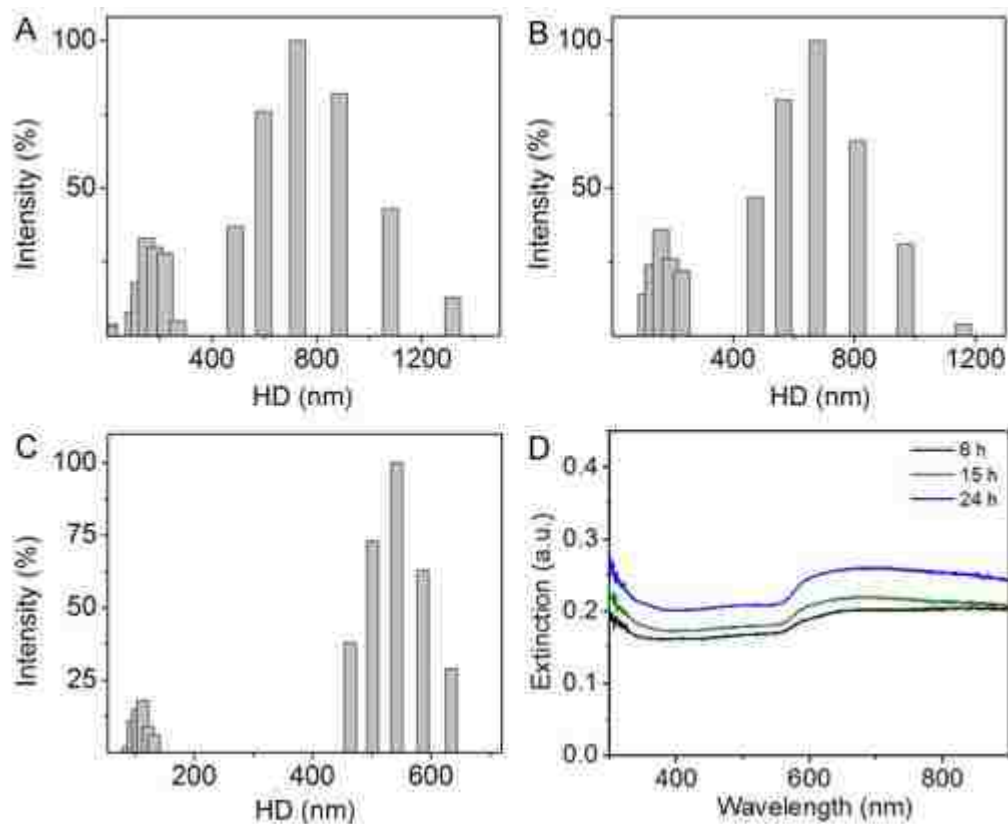
Figure S8. DLS measurement of the aliquots from the microemulsion in the absence of TEOS at different time points: (A) 6 h, (B) 15 h, and (C) 24 h. (D) UV-vis spectra of the corresponding samples in (A)-(C).
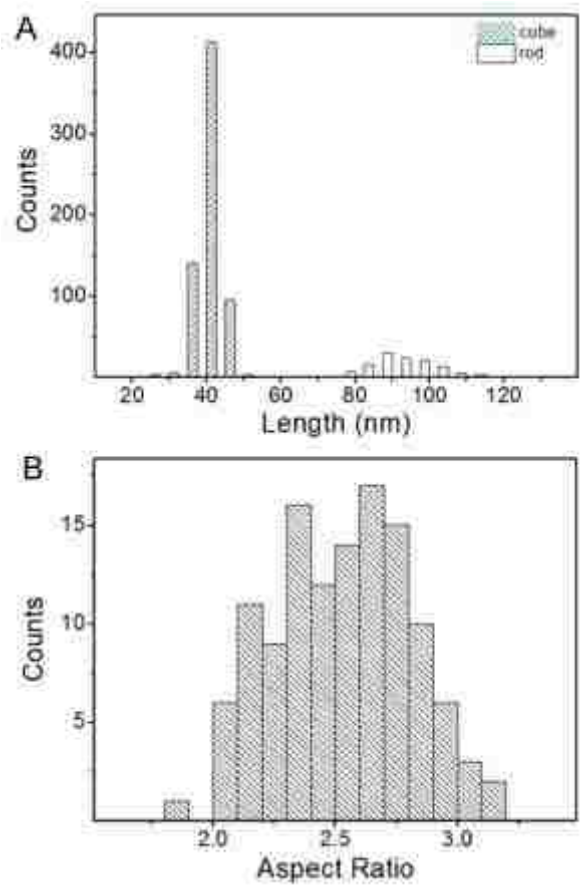
Figure S9. Size distribution analysis of the sample in Figure 6A: (A) histogram of the size distribution of Cu cubes and rods; and (B) histogram of the aspect ratios of the Cu rods.

Figure S10. TEM image of close-up view of the sample in Figure 6C, showing the silica coating is mostly uniform and discrete.

Figure S11. TEM image of the SiO_2 shell after the Cu cores of the Cu-SiO_2 core-shell structures were etched with 0.3 mM $FeCl_3$ for 10 min.
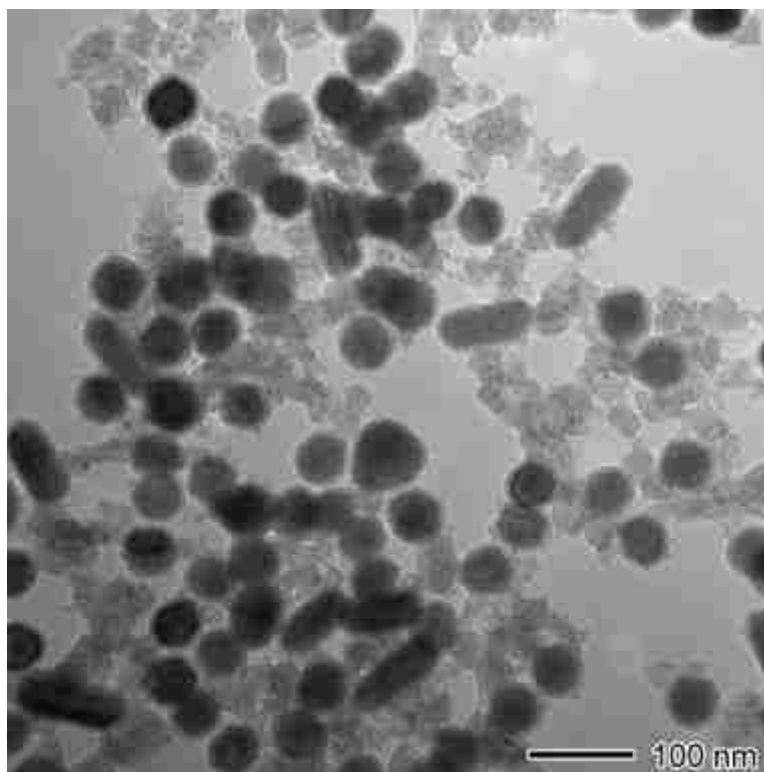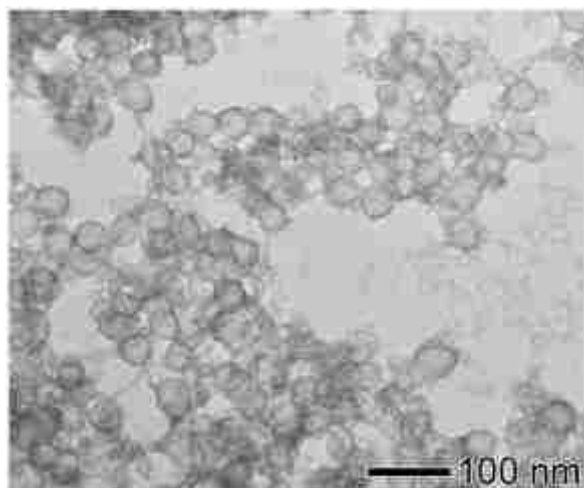
Chapter IV: Synthesis of Optical and Magnetic Bifunctional Core-Shell Nanostructures:

Controlled Growth of Metal Oxides on Metal Nanoparticle Surfaces

Abstract

Metal and metal oxide hybrid nanostructures that couple optical and magnetic properties in one single nanostructure show a lot of promise for their use in various applications. While most methods are limited to producing noble metal coupled to metal oxide type structures, the application of these same methods to non-noble metals is quite challenging. In this work, we report a general synthetic route where zero valence transition metal precursors are decomposed onto seed particles containing active metals to synthesize metal core-metal oxide shell structures. This approach was initially applied to $AuCu_3$ nanorod seeds to produce a Fe_3O_4 coating. The coating thickness is temperature-dependent within the limit that heterogeneous growth is dominant. At a relatively-low temperature, this approach could be extended to other metal oxides such as NiO and MnO and other metal seeds such as Cu. At this low temperature, it was found that the thickness of the metal oxide shell was thermodynamically limited, producing uniform thin shells, regardless the molar ratio of precursor to seed. By etching the core, these hybrid nanostructures were converted into hollow metal oxide structures. Both of these core-shell hybrid nanostructures retain properties from their initial nanoparticle seed, and the hollow metal oxides can find potential use in broader applications.

Introduction

Nanostructures with distinct optical and magnetic properties have attracted a lot of research attention due to their ability to manipulate light and their response to magnetic fields at the nanoscale for various applications. Metal nanostructures plasmonic properties can strongly absorb and/or scatter light and be used for optical sensing, biomedicine, and plasmon-enhanced photocatalysis.[1-3] The peak position and intensity of the localized surface plasmon resonance (LSPR) of metal nanostructures can be tuned by controlling the size, shape and composition of the nanocrystal.[4] On the other hand, nanoscale ferrimagnetic or ferromagnetic particles whose size are equal to or smaller than the magnetic grain size become superparamagnetic; this superparamagnetic behavior allows for dispersion in solution without spontaneous aggregation, making them ideal for contrast enhancement in magnetic resonance imaging (MRI), magnetic-guided drug delivery, magnetic separation and detection.[5-8] Furthermore, these magnetic metal oxide nanostructures are also of notable interest due to the high surface area and reactivity, showing promise for use in energy conversion and storage, catalysis, and micrelectronics.[9-11] In addition, the magnetic transition metal oxides, such as Fe_3O_4, NiO, and MnO, are of special interest for their use in supercapacitors and Li-ion batteries.[10,12,13] Combining plasmonic and magnetic properties into a single nanostructure can enable dual functionality which is important for a broad range of multiplexed applications; yet the synthesis of hybrid nanostructures remains to be a challenge.[5,14] Herein, this work develops a facile synthetic route to metal and metal oxide core-shell nanostructures through controlled deposition of the zero valence $3d$ transition metals on metal seeds, and thus fine control over the resulting optical properties and magnetic properties of the hybrid nanostructures.

A variety of methods have been developed for the synthesis of hybrid optical and magnetic nanoparticles. Depending on the combination of materials, plasmonic metals (e.g. Au and Ag) and magnetic metals (e.g. Ni, Fe, or Co) can form heterostructures with segmented/Janus configurations or alloys, while plasmonic metals and magnetic metal oxides can form core-shell/yolk-shell or dimers.[15-18] Some of these approaches may cause the loss of the plasmonic properties of the metal component due to the damping effects of the 3d transition metals in the process of incorporating the magnetic domain. For example, when Au alloys with Fe, the plasmonic characteristics of Au vanishes.[19] Since the 3d transition metal is very easy to be oxidized and the plasmonic properties are lost in the alloy structures, synthesis of Au and Fe_3O_4 hybrid nanostructures become a popular route to prepare the bi-functional materials with preserved plasmonic and magnetic properties. In general, there are two chemical routes to synthesize Au and Fe_3O_4 hybrid nanoparticles: one is to coat Au on the surface of the Fe_3O_4 or γ-Fe_2O_3 nanoparticles;[20] and the other is to thermally decompose metal oxide precursors on the Au nanoparticles.[17,18] Thermal decomposition to deposit Fe_3O_4 on premade Au nanoparticles allows for enhancement of the Fe_3O_4 nanoparticles, while also maintaining the small size for improved superparamagnetic properties. However, maintaining the shape of the nanocrystals at high temperature is very challenging. In this work, we develop a method with tight control over the reaction temperature during the deposition of metal oxide to synthesize metal-metal oxide core-shell structures. The initial demonstration was carried out using $AuCu_3$ nanorods as seeds for the deposition of Fe_3O_4. Thin and thick shells could be controlled by varying the reaction temperature between 200 to 280 ^{o}C. The optical and magnetic properties of these metal-metal oxide hybrid nanostructures were also studied. This approach could be extended to other metal oxide (i.e. NiO and MnO) and other seeds (i.e. Cu) to some extent. By using the active metal Cu

seeds, the core-shell structures could be hollowed out using ammonium hydroxide etching. These studies provide us a facile means to synthesize metal-metal oxide hybrid nanostructures with bi-functionality towards different applications.

Experimental Methods

Chemicals. Ttetradecylamine (TDA, >95%), was purchased from T.C.I, Hydrogen tetrachloroaurate trihydrate ($HAuCl_4 \cdot 3H_2O$), 1-octadecene (ODE, 90%), Bis(cyclooctadiene)nickel, dimanganese decacarbonyl ($Mn_2(CO)_{10}$), Ammonium hydroxide (28-30% NH_3 basis), and copper 2,4-pentanedionate ($Cu(acac)_2$) were purchased from Alfa Aeser. Oleylamine (OLAM, 70%) was purchased from Sigma-Aldrich. Iron(0) pentacarbonyl ($Fe(CO)_5$) was purchased from Acros Organics.

Synthesis of AuCu₃ nanorod seeds. AuCu$_3$ nanorods were synthesized using our previously reported procedure.[21] Briefly, tetradecylamine (20 mmol, 430 mg) and $HAuCl_4 \cdot 3H_2O$ (0.05 mmol, 19.7 mg) were added to a 25 mL three-neck flask equipped with a magnetic stir bar. Argon was blown over the reaction mixture for 10 min to remove O_2. The reaction mixture was heated directly to 160 °C and maintained for 20 min. Without separation, $Cu(acac)_2$ (0.2 mmol, 52.4 mg) in 1 mL of OLAM was injected to the reaction mixture, followed by heating the reaction directly to 210 °C and maintaining for another 20 min. After the reaction, the product was purified by adding toluene and centrifuging at 3300 rpm for 2 min to remove excess reactants and surfactants.

Synthesis of AuCu₃@Fe₃O₄ core-shell structures. A thermal decomposition method of Fe(0) complex on the AuCu$_3$ nanorods was applied to synthesize AuCu$_3$@Fe$_3$O$_4$ core-shell structures. In a typical procedure, AuCu$_3$ nanorods (1-10 mg) in toluene were dried under argon prior to

dispersing in 5 mL ODE and 0.2 mL OLAM *via* sonication. The $AuCu_3$ nanorod suspension was added to a 25 mL three-neck flask equipped with a magnetic stir bar. Argon was blown over the mixture for 20 min prior to the Fe_3O_4 encapsulation, and was used as a protective gas throughout the reaction. The temperature was raised directly to 110 ^{o}C and held for 10 min, followed by the addition of $Fe(CO)_5$ (0.148 mmol, 20 μL) and heating reaction mixture at a rate of <5 ^{o}C/min to 200 ^{o}C for thin shells (1-2 nm), or to 280 ^{o}C for thick shells (5-6 nm). The reaction temperature was then maintained for 60 min. To ensure conversion to Fe_3O_4, the particle suspension was exposed to the atmosphere at 130°C for an additional hour. After the reaction, the product was cooled to room temperature and purified by adding 25 mL of ethanol and centrifuging at 7800 rcf for 5 min, followed by dispersing in 20 mL toluene and 10 mL ethanol and centrifuging a second time at 3900 rcf to remove excess reactants, surfactants, and iron oxide nanoparticles.

Synthesis of $AuCu_3$@NiO core-shell structures. The Fe_3O_4 coating method was modified by replacing $Fe(CO)_5$ with bis(cyclooctadiene)nickel (0.148 mmol, 40 mg) dispersed in ODE. Only ~2nm thick shells was successfully produced.

Synthesis of $AuCu_3$@MnO core-shell structures. The Fe_3O_4 coating method was modified by replacing $Fe(CO)_5$ with ($Mn_2(CO)_{10}$) (0.148 mmol, 58 mg) dispersed in ODE. Only ~2nm thick shells was successfully produced.

Synthesis of Cu nanoparticles. Cu nanoparticles were produced by reducing $Cu(acac)_2$ in the presence of OLAM, TOP, in situ generated CO using our previously reported procedure.[22] Cu nanoparticles with a size of ~70 nm were produced by decreasing the volume of gas phase reducing agents added at 200 ^{o}C.

Etching of Cu in the Cu containing core-shell structures. The Cu cores were dissolved by ammonium hydroxide to produce metal oxide shells. In a typical procedure, the core-shell

structure suspension of Cu@Fe$_3$O$_4$ and Cu@MnO were separated from the solvent toluene by centrifugation and then dispersed in ammonium hydroxide solution. The etching process was carried out in the presence of excess oxygen. After etching, the product was purified by centrifugation and suspended in ethanol or water. The completion of the etching process is indicated by a lack of blue copper aqua-ammonium complex color when ammonium hydroxide is added to the purified product.

Characterization. Transmission electron microscopy (TEM) images were captured using a transmission electron microscope (JEOL JEM-1011) with an accelerating voltage of 100 kV. High angle annular dark field scanning transmission electron microscopy (HAADF-STEM) images, high-resolution TEM (HRTEM) images, and energy-dispersive X-ray (EDX) mapping were obtained using a double Cs-corrected JEOL JEM-ARM200F microscope. X-ray powder diffraction (XRD) was performed using a bench-top x-ray diffractometer (Rigaku Miniflex II). The concentrations of metals were determined using a flame atomic absorption (AA) spectrometer (GBC 932). UV-vis spectra were taken on a UV-vis spectrophotometer (Agilent Cary 50). Magnetic properties were measured by a superconducting quantum interference device (SQUID).

Results and Discussion:

The AuCu$_3$@Fe$_3$O$_4$ core-shell nanostructures were synthesized by thermally decomposing Fe(CO)$_5$ in the presence of the pre-formed AuCu$_3$ nanorods. The AuCu$_3$ cores were synthesized by the use of our previously published approach.[21] These nanorod cores have a dimension of 10 × 30 nm as shown in Figure **1A**. A fixed amount of these nanorod seeds was used for the deposition of Fe$_3$O$_4$ shells at different temperatures. At a low temperature (200°C), a uniform

coating of thin iron oxide with an average of 1-2 nm thickness was deposited on the nanorods to form the $AuCu_3@Fe_3O_4$ core-shell structures (**Fig. 1B**). Increasing the reaction temperature to 280 ^{o}C produced 5-6 nm Fe_3O_4 shells on the $AuCu_3$ seeds (**Fig. 1C**). At the same time, the aspect ratio of the nanorod cores decreased due to the instability of $AuCu_3$ at high temperature in the presence of the OLAM. This instability was also evidenced by the observation of the etched $AuCu_3$ cores presented in the sample. Interestingly, some of the coating appeared to be thicker along the side of the nanorods compared to that of the ends of the nanorods possibly due to the curvature effects. However, continuing to increase the reaction temperature above 280 ^{o}C does not help to increase the coating thickness. Instead, the shell coating remained to be thin and the excess free iron oxide particles were formed as by-products, as shown in **Figure 1D**. These results clearly show that the temperature of 280 ^{o}C is the critical turning point from heterogeneous nucleation and homogeneous nucleation of Fe on $AuCu_3$.
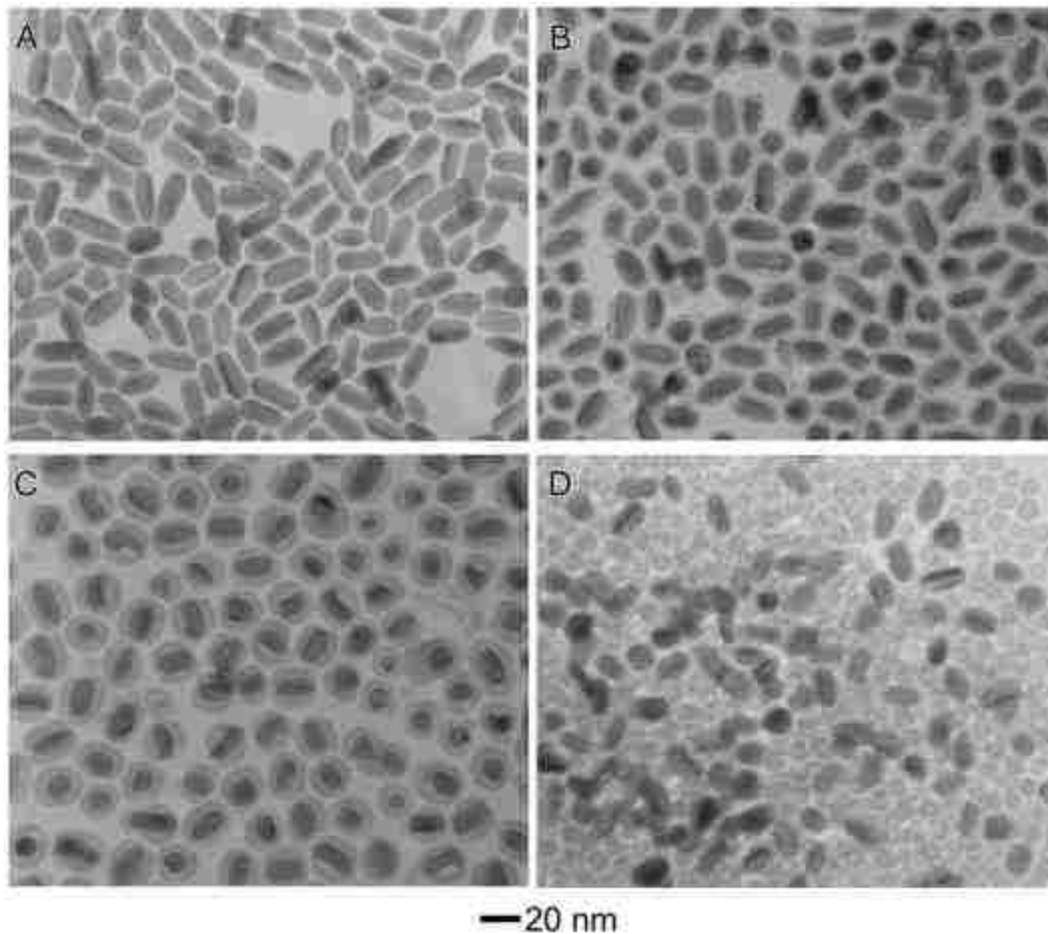
Figure 1. TEM images of controlled deposition of Fe_3O_4 shells on the $AuCu_3$ nanorods: (A) $AuCu_3$ nanorod seeds; (B) $AuCu_3@Fe_3O_4$ core-shell structures with a thin shell of 1-2 nm prepared at 200 ^oC; (C) $AuCu_3@Fe_3O_4$ core-shell structures with a thin shell of 6 nm prepared at 280^oC; and (D) a mixture of $AuCu_3@Fe_3O_4$ core-shell structures and free iron oxide particles prepared at 315^oC.

118

Figure 2 illustrates the temperature control of the $Fe(CO)_5$ decomposition to deposit Fe_3O_4 on $AuCu_3$ nanorods to form $AuCu_3@Fe_3O_4$ core-shell structures. $Fe(CO)_5$ is a common precursor used to produce Fe_3O_4 nanoparticles and metal-Fe_3O_4 hybrid nanostructures.[17,23] During the decomposition, the $Fe(CO)_5$ complex decomposes at elevated temperatures to produce Fe atoms. These atoms can self-nucleate to form Fe nuclei or, when seeds are present, deposit on the seeds *via* heterogeneous growth.[24] The heterogeneous growth has a lower activation barrier, therefore, at low temperature (i.e. below 280 ^{o}C), the deposition of Fe atoms on the $AuCu_3$ nanorods is favored. When the temperature increases above this critical temperature, the concentration of Fe atoms dramatically increases to exceed the critical supersaturation concentration, and thus rapidly self-nucleates to form Fe clusters and then Fe_3O_4 nanoparticles. In order to form core-shell structures, the temperature ramping rate (<5 ^{o}C/min) is important to avoid overshooting the critical temperature which may lead to shortening the $AuCu_3$ nanorod cores and/or produce undesired Fe_3O_4 nanoparticles.
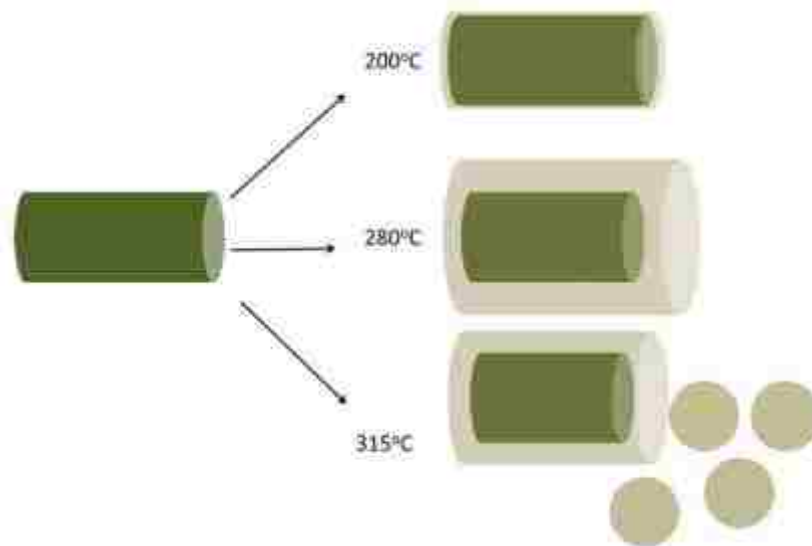
Figure 2. Schematic illustration of the controlled deposition of metal oxide coatings on the AuCu$_3$ nanorods to produce AuCu$_3$@Fe$_3$O$_4$ core-shell nanostructures through temperature control.

While the temperature is critical to control the Fe_3O_4 shell thickness, the ratio of the seeds to Fe precursor doesn't seem to play a significant role to the coating thickness. At 200 ^{o}C, $Fe(CO)_5$ was increased by 3 times, from 0.15 to 0.6 mmol, at the fixed amount of nanorod seeds. The shell thickness remained similar at ~2 nm, but a large amount of Fe_3O_4 was found in the product as a result of excess Fe precursor (**Fig. S1**). At the same temperature (200 ^{o}C), the seed concentrations were varied from ~0.5 mg to 6 mg, while holding the concentration of the Fe precursor constant. Similarly, the shell thickness does not vary with the seed concentration and remains to be ~2 nm (**Fig. S2**). Considering the geometry and particle concentration, this amount of seed particles corresponds to an estimated change in seed surface area from 3×10^{17} to 3×10^{18} nm^2 with no observed change in Fe_3O_4 thickness, suggesting that the Fe_3O_4 deposition is primarily governed thermodynamically, rather than kinetically limited. This observation implies that the barrier for self-nucleation of the Fe_3O_4 is above 280 ^{o}C, indeed many procedures call for heating above 280 ^{o}C to produce Fe_3O_4 nanoparticles utilizing a hot injection approach[25]. To minimize the by-product Fe_3O_4 nanoparticles, the reaction temperature and the precursor $Fe(CO)_5$ should be kept below 280 ^{o}C and 28 mM, respectively.

The $AuCu_3@Fe_3O_4$ core-shell nanostructures were further analyzed by HRTEM and EDX elemental mapping. **Figure 3A** shows the TEM characterization of the $AuCu_3@Fe_3O_4$ core-shell nanostructures with a thin shell. In the HRTEM, the Fe_3O_4 shell is measured to be ~2 nm thick and polycrystalline with very fine domains. The HAADF-STEM displays that a Fe_3O_4 shell uniformly coats the $AuCu_3$ nanorod and the EDX mapping confirms the composition of a Fe-containing shell on the Au-containing core. **Figure 3B** shows the TEM characterization of the $AuCu_3@Fe_3O_4$ core-shell nanostructures with a thick shell. In the HRTEM, the Fe_3O_4 shell is measured to be ~5 nm thick and also polycrystalline with relatively-large domains compared to

those in the thin shell; however, there seems to have a gap between the core and the shell. The HAADF-STEM and EDX mapping verifies the observation in the HRTEM indicating that the shell and core are indeed separate. The result of the gap can be attributed to the two factors: the oxidation of Fe to Fe_3O_4 and/or the etching of the $AuCu_3$ core. As can be seen, as the shell becomes thicker, the Fe_3O_4 coating becomes less uniform and deposits along the long side of the rods. This change may result from the increased crystallinity of the Fe_3O_4 domain at a higher reaction temperature, and the Fe atoms or Fe_3O_4 small clusters rearranging to minimize surface energy in the same fashion as layer-island growth on areas where the curvature is minimal.[17,26,27]
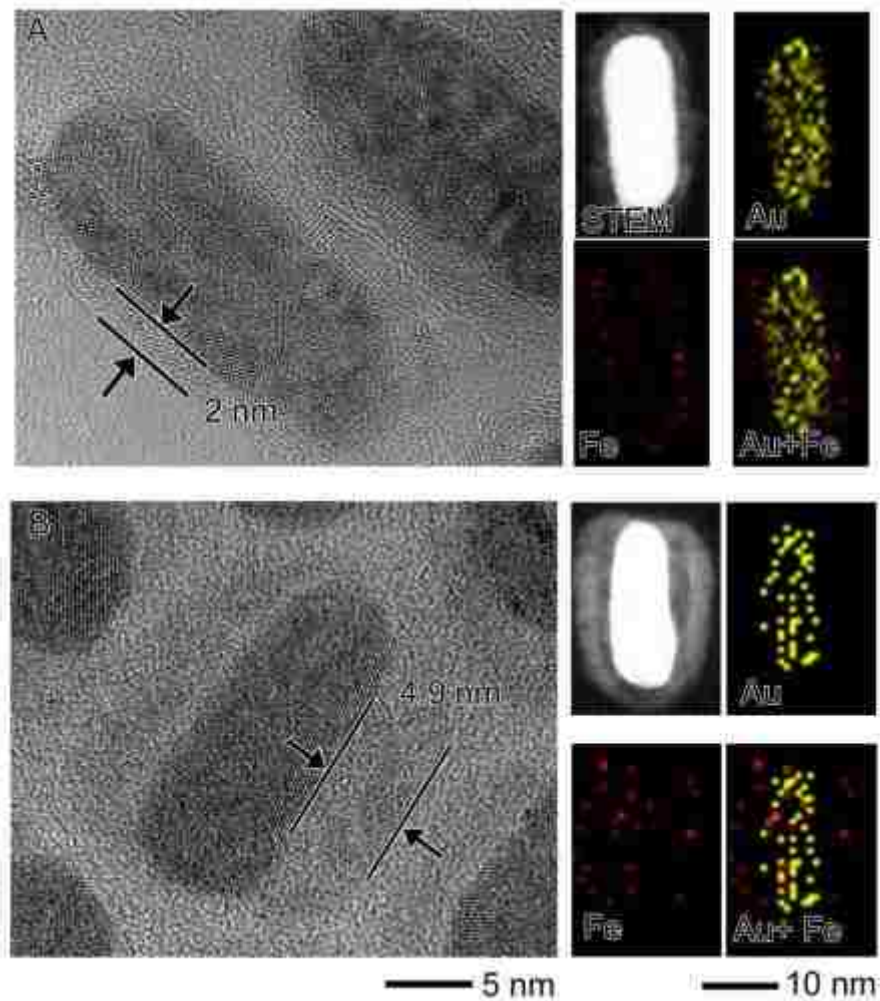
Figure 3. TEM characterization of $AuCu_3@Fe_3O_4$ core-shell nanostructures: (A) with a thin shell of 2 nm (HRTEM is on the left. HAADF-STEM and EDX elemental mapping is on the right); and (B) with a thick shell of 5 nm (HRTEM is on the left. HAADF-STEM and EDX elemental mapping is on the right).

The optical properties of these bi-functional $AuCu_3@Fe_3O_4$ core-shell nanostructures were studied. **Figure 4A** shows the extinction spectra of $AuCu_3$ nanorods before and after coating the thin and thick Fe_3O_4 shell, the samples labelled (a), (b), and (c), correspond to the samples shown in **Figure 1, A-C**, respectively. The longitudinal mode of the LSPR peak of $AuCu_3$ nanorods suspended in toluene was red shifted from 647 nm to 710 nm due to the coating of the Fe_3O_4 on the nanorod surface. In contrast, the peak was blue shifted to 590 nm for the $AuCu_3$ nanorods with a thick Fe_3O_4 shell because the effect of the change of the aspect ratio on the plasmonic properties of $AuCu_3$ nanorods dominates the effect of Fe_3O_4 coating. The histograms of size distribution were plotted in **Figure 4B**, indicating that the average particle length decreased from 18.7, 17.7, and 15.2, respectively. In addition to peak shift, the UV-vis spectra show the increase of the damping effect on the plasmonic peak as the Fe_3O_4 shell becomes thicker, which is consistent with the observations in a previous study.[28] In our case, this damping effect is not purely the result of shell thickness of Fe_3O_4. The broadening of the spectra could be attributed to the other factors such as inhomogeneity of size (i.e. aspect ratio) changes.
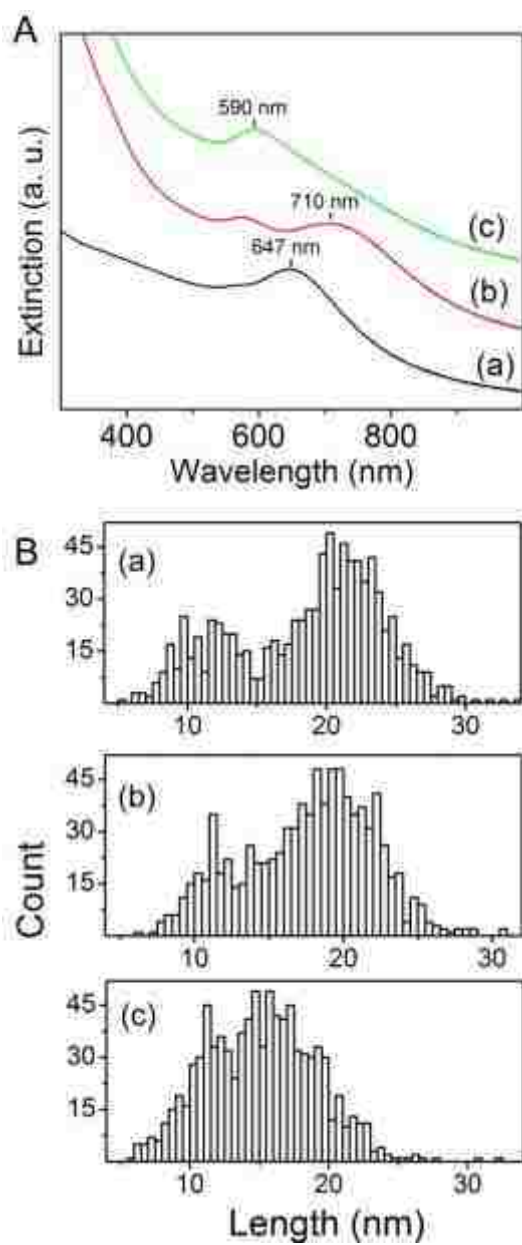
Figure 4. (A) UV-vis spectra of the AuCu$_3$ nanorods before (a) and after the coating of Fe$_3$O$_4$ with a thin shell of ~2 nm (b), and a thick shell of ~5 nm (c). (B) Histograms of size distribution of the samples (a), (b), and (c).

The magnetic properties of these bi-functional $AuCu_3@Fe_3O_4$ core-shell nanostructures were measured by SQUID and compared to that of the Fe_3O_4 nanoparticles with a size of 5 nm. **Figure 5** plots the magnetization of different samples as a function of magnetic field strength. After synthesis, these samples were exposed to atmosphere at 130 $^{\circ}$C for 60 min to ensure the complete oxidation of the Fe to iron oxide.[29]   Although all three samples exhibit a lack of hysteresis, indicating superparamagnetic behavior, the core-shell structure with a thin shell responses to the magnetic field slower that with a thick shell and Fe_3O_4 nanoparticles. Compared to Fe_3O_4 nanoparticles the magnitude of the magnetization of the core-shell structures decreases by half, possibly due to the crystallinity difference (i.e. polycrystalline vs. single crystalline). The domain wall in the polycrystalline Fe_3O_4 hampers the magnetic properties of the material.
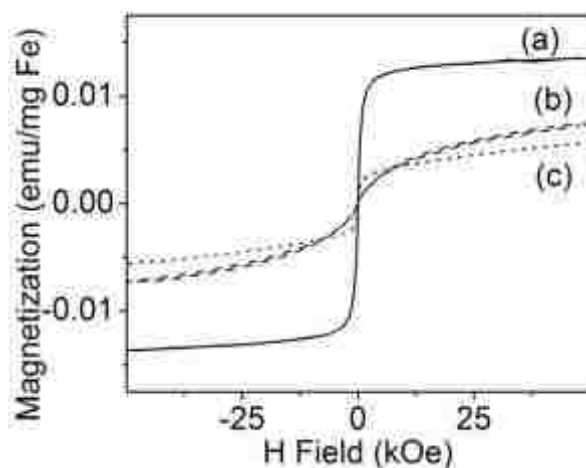

Figure 5. Magnetic measurements of (a) Fe_3O_4 nanoparticles with the size of 5 nm, (b) $AuCu_3@Fe_3O_4$ with a thin shell of ~2 nm, and (C) AuCu3@Fe_3O_4 with a thick shell of ~ 5 nm.

The temperature controlled approach of thermal decomposition of a zero valence complex to coat Fe_3O_4 on $AuCu_3$ seeds can be further expanded to other metal oxides such as Ni and Mn oxides. Ni oxides and Mn oxides are of interest as promising electrode materials and/or magnetic

resonance contrast materials for energy- or bio-related applications.[12,30] When the metal precursor was replaced by bis(cyclooctadiene)nickel and dimanganese decacarbonyl, core-shell structures of AuCu$_3$@NiO and AuCu$_3$@MnO were formed, respectively, at a reaction temperature of 200 ^{o}C. Similar to Fe$_3$O$_4$, thin layers of NiO and MnO were coated on the AuCu$_3$ seeds, as shown in the **Figure 6, A and B**. However, when the temperature was increased, thicker shells were not successfully produced. In the case of Ni, Ni atoms self-nucleate and form NiO nanoparticles at the temperature of 250 ^{o}C (**Fig. S3**), suggesting Ni undergoes homogenous growth at a lower temperature compared to Fe (i.e. homogeneous growth above 280 ^{o}C). For Mn, increasing temperature to 250 ^{o}C caused the dissolution of Cu from the AuCu$_3$ alloy, resulting in the formation of the Au nanoparticles, as shown in TEM image and XRD pattern of **Figure S4**. This observation could be attributed to the ability of Mn that could alloy with copper at elevated temperatures and at a broad continuum of Cu-Mn ratios.[31] Interestingly, the diffraction pattern of Cu-Mn alloy was not observed possibly due to the lack of crystallinity of the Cu-Mn alloy. The UV-vis spectrum of the AuCu$_3$@NiO core-shell structure shows a blue shift from that of AuCu$_3$ seeds by 80 nm while the UV-vis spectrum of the AuCu$_3$@MnO core-shell structure shows a red shift from that of AuCu$_3$ seeds for the longitudinal mode by 60 nm. In both cases, the peak intensity was dampened due to the presence of the metal oxide shell.
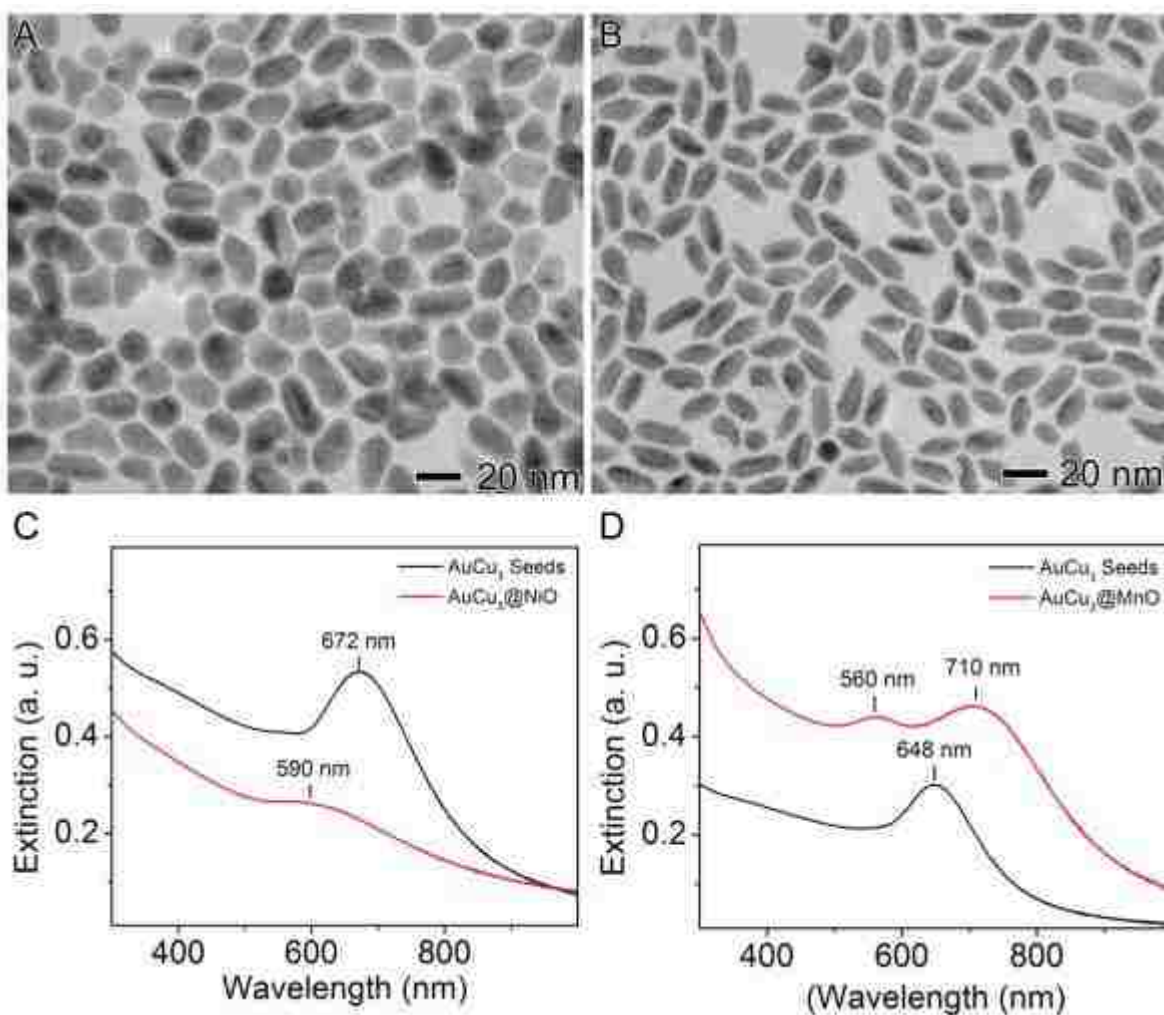
Figure 6. (A, B) TEM images of different core-shell structures: (A) AuCu$_3$@NiO; and (B) AuCu$_3$@MnO. (C, D) UV-vis spectra of the samples suspended in toluene before (black line) and after coating (red line): (C) AuCu$_3$@NiO; and (D) AuCu$_3$@MnO.

The core-shell structures of AuCu$_3$@NiO and AuCu$_3$@MnO were further confirmed by the HRTEM characterization and EDX elemental analysis. **Figure 7A** shows the TEM characterization of the AuCu$_3$@NiO core-shell nanostructures. In the HRTEM, the NiO shell is measured to be ~2 nm thick. The HAADF-STEM displays that a NiO shell uniformly coats the AuCu$_3$ nanorod and the EDX mapping confirms the composition of Ni-containing shell on the Au- and Cu-containing core. **Figure 7B** shows the TEM characterization of the AuCu$_3$@MnO

core-shell nanostructures. In the HRTEM, the MnO shell is measured to be ~2 nm thick. The HAADF-STEM displays that a MnO shell uniformly coats the $AuCu_3$ nanorod and the EDX mapping confirms the composition of Mn-containing shell on the Au- and Cu-containing core.
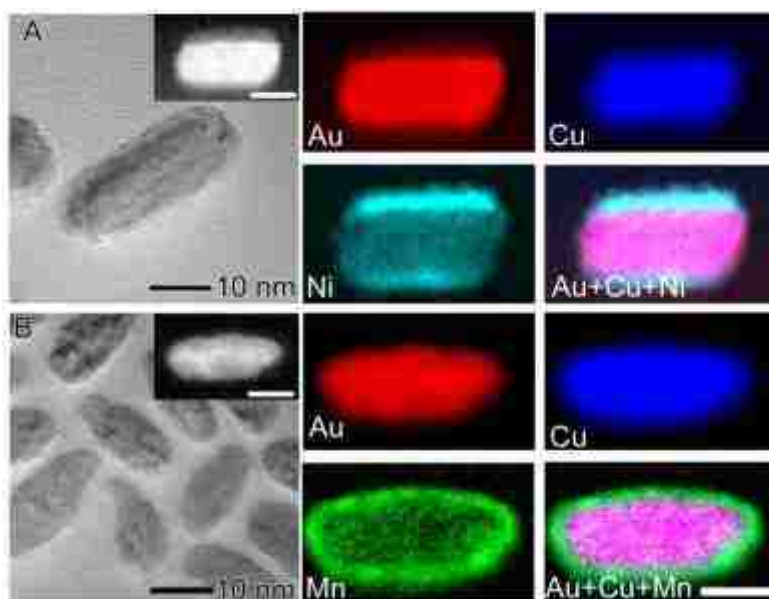

Figure 7. TEM characterization of different core-shell nanostructures: (A) $AuCu_3@NiO$ (HRTEM is on the left. HAADF-STEM and EDX elemental mapping is on the right); and (B) $AuCu_3@MnO$ (HRTEM is on the left. HAADF-STEM and EDX elemental mapping is on the right).

The temperature controlled approach of thermal decomposition of zero valence complexes to coat metal oxides on $AuCu_3$ seeds can be further expanded to other metals such as Cu. The Cu seeds were synthesized using our previously published Cu nanocubes.[22] From the TEM image (**Fig. S5**), the size of these Cu seeds were measured to be ~70 nm. The same procedure of metal oxide coating at 200 $^{\circ}$C was applied to these Cu seeds, followed by the ammonia hydroxide etching process to verify the success of the coating process. **Figure 8A** illustrates this procedure, suggesting this approach and the use of the Cu seeds provides a facile means to synthesize

hollow metal oxides. This approach could be applied to Fe_3O_4 and MnO to generate metal-metal oxide core-shell structures and then etched to form metal oxide hollow structures. **Figure 8, B and C**, shows TEM images of Cu@Fe_3O_4 core-shell structures and the Fe_3O_4 hollow shells, indicating a very thin layer of Fe_3O_4 shell could be homogeneously coated on the surface of the Cu seeds. Likewise, **Figure 8, D and E**, shows TEM images of Cu@MnO core-shell structures and the MnO hollow shells, indicating a very thin layer of MnO shells could be homogeneously coated on the surface of the Cu seeds. This approach can serve as a templating method to produce hollow metal shells of different shapes. For example, if Cu nanorods are present in the sample, rod-shaped iron oxide hollow shells can be synthesized, as shown in **Figure S6**. It is worth noting that these oxides are lacking of identifiable XRD pattern (**Fig. S7**), possibly due to the poor crystallinity of the thin shells. The attempt to apply this approach to NiO failed because Ni is very easy alloys with Cu especially at elevated temperature and Cu-Ni alloy surface protects against oxidative etching.[32]
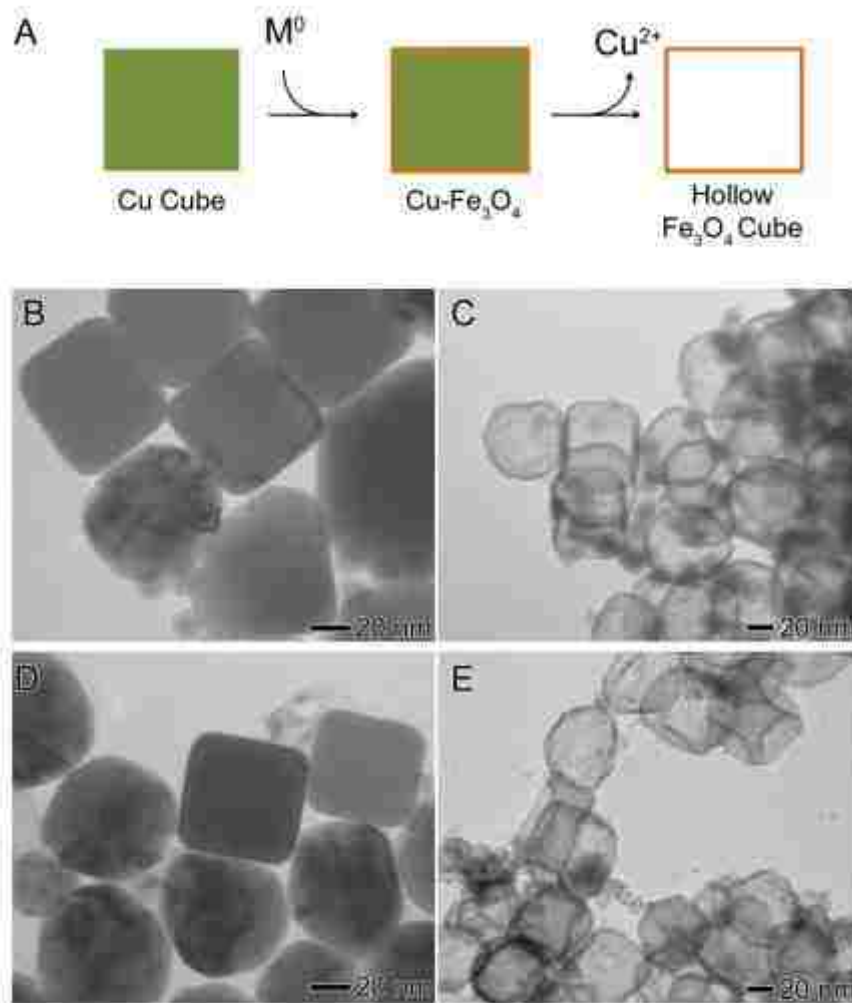
Figure 8. (A) schematic illustration of the use of Cu seeds to temperature control coating of metal oxide shells, followed by the etching of Cu to generate hollow metal oxide. (B,C) TEM characterization of Cu@Fe$_3$O$_4$ before (B) and after (C) etching with ammonium hydroxide. (D,E) TEM characterization of Cu@MnO before (D) and after (E) etching with ammonium hydroxide.

Conclusion

A temperature-controlled thermal decomposition of zero valence-transition metal complexes approach was developed to coat preformed hydrophobic metal nanoparticles and generated metal and metal oxide core-shell hybrid nanoparticles. This approach was successfully demonstrated to synthesize $AuCu_3@Fe_3O_4$ core-shell nanoparticles with a thin and a thick shell of ~2 nm and ~5 nm, respectively. These core-shell nanoparticles exhibit both optical and magnetic properties. The synthesis could be extended to other metal oxides to produce optically-active $AuCu_3@NiO$ and $AuCu_3@MnO$ core-shell structures, as well as Cu seeds to yield $Cu@Fe_3O_4$ and $Cu@MnO$ core-shell structures. Additionally, the Cu core in the $Cu@Fe_3O_4$ and $Cu@MnO$ core-shell structure could be etched to generate hollow metal oxide shells which could potentially become a versatile method for the production of hollow metal oxide nanostructures based on the shape of Cu templates. This work provides a general method to control heterogeneous growth of metal oxide on the metal particle surface to form core-shell hybrid nanostructures for various applications.

SURPPLEMENTAL INFORMATION

TEM image of $AuCu_3@Fe_3O_4$ produced with excess Fe precursor; Scatter plot of Fe_3O_4 shell thickness as a function of seed mass added to the reaction; TEM image of $AuCu_3@NiO$ produced by heating to 250^oC; TEM and XRD characterization of $AuCu_3@MnO$ produced by heating to 250^oC; ~70 nm Cu seed particles; TEM of Cu nanorods used to produce hollow Fe_3O_4 nanorod shells; XRD characterization of $Cu@Fe_3O_4$ before etching and resulting hollow Fe_3O_4 structures.

ACKNOWLEDGEMENT

REFERENCES

(1)   Elghanian, R.; Storhoff, J. J.; Mucic, R. C.; Letsinger, R. L.; Mirkin, C. A. Selective Colorimetric Detection of Polynucleotides Based on the Distance-Dependent Optical Properties of Gold Nanoparticles. *Science* **1997**, *277*, 1078.

(2)   Xia, Y.; Li, W.; Cobley, C. M.; Chen, J.; Xia, X.; Zhang, Q.; Yang, M.; Cho, E. C.; Brown, P. K. Gold Nanocages: From Synthesis to Theranostic Applications. *Accounts of Chemical Research* **2011**, *44*, 914.

(3)   Hou, W.; Cronin, S. B. A Review of Surface Plasmon Resonance-Enhanced Photocatalysis. *Advanced Functional Materials* **2013**, *23*, 1612.

(4)   Jain, P. K.; Lee, K. S.; El-Sayed, I. H.; El-Sayed, M. A. Calculated Absorption and Scattering Properties of Gold Nanoparticles of Different Size, Shape, and Composition: Applications in Biological Imaging and Biomedicine *The Journal of Physical Chemistry B* **2006**, *110*, 7238.

(5)   Levin, C. S.; Hofmann, C.; Ali, T. A.; Kelly, A. T.; Morosan, E.; Nordlander, P.; Whitmire, K. H.; Halas, N. J. Magnetic−Plasmonic Core−Shell Nanoparticles. *ACS Nano* **2009**, *3*, 1379.

(6)   Shin, J.; Anisur, R. M.; Ko, M. K.; Im, G. H.; Lee, J. H.; Lee, I. S. Hollow Manganese Oxide Nanoparticles as Multifunctional Agents for Magnetic Resonance Imaging and Drug Delivery. *Angewandte Chemie International Edition* **2009**, *48*, 321.

(7)   Sotiriou, G. A.; Hirt, A. M.; Lozach, P.-Y.; Teleki, A.; Krumeich, F.; Pratsinis, S. E. Hybrid, Silica-Coated, Janus-Like Plasmonic-Magnetic Nanoparticles *Chemistry of Materials* **2011**, *23*, 1985.

(8)   Xu, C.; Sun, S. Magnetic Core/Shell Fe3O4/Au and Fe3O4/Au/Ag Nanoparticles with Tunable Plasmonic Properties. *Polymer International* **2007**, *56*, 821.

(9)   Tang, X.; Liu, Z.-h.; Zhang, C.; Yang, Z.; Wang, Z. Synthesis and capacitive property of hierarchical hollow manganese oxide nanospheres with large specific surface area. *Journal of Power Sources* **2009**, *193*, 939.

(10)   Wei, W.; Cui, X.; Chen, W.; Ivey, D. G. Manganese oxide-based materials as electrochemical supercapacitor electrodes. *Chemical Society Reviews* **2011**, *40*, 1697.

(11)   Yin, Y.; Rioux, R. M.; Erdonmez, C. K.; Hughes, S.; Somorjai, G. A.; Alivisatos, A. P. Formation of Hollow Nanocrystals Through the Nanoscale Kirkendall Effect. *Science* **2004**, *304*, 711.

(12)   Sun, X.; Wang, G.; Hwang, J.-Y.; Lian, J. Porous nickel oxide nano-sheets for high performance pseudocapacitance materials. *Journal of Materials Chemistry* **2011**, *21*, 16581.

(13)   Zhou, G.; Wang, D.-W.; Li, F.; Zhang, L.; Li, N.; Wu, Z.-S.; Wen, L.; Lu, G. Q.; Cheng, H.-M. Graphene-Wrapped Fe3O4 Anode Material with Improved Reversible Capacity and Cyclic Stability for Lithium Ion Batteries. *Chemistry of Materials* **2010**, *22*, 5306.

(14)   Zhang, J.; Tang, Y.; Lee, K.; Ouyang, M. Tailoring light-matter-spin interactions in colloidal hetero-nanostructures *Nature* **2010**, *466*, 91.

(15)   Lim, Y. T.; Cho, M. Y.; Kim, J. K.; Hwangbo, S.; Chung, B. H. Plasmonic Magnetic Nanostructure for Bimodal Imaging and Photonic-Based Therapy of Cancer Cells. *ChemBioChem* **2007**, *8*, 2204.

(16)   Zhang, Y.; Ding, H.; Liu, Y.; Pan, S.; Luo, Y.; Li, G. Facile one-step synthesis of plasmonic/magnetic core/shell nanostructures and their multifunctionality. *Journal of Materials Chemistry* **2012**, *22*, 10779.

(17)   Yu, H.; Chen, M.; Rice, P. M.; Wang, S. X.; White, R. L.; Sun, S. Dumbbell-like Bifunctional Au−Fe3O4 Nanoparticles. *Nano Letters* **2005**, *5*, 379.

(18)   Xu, Z.; Hou, Y.; Sun, S. Magnetic Core/Shell Fe3O4/Au and Fe3O4/Au/Ag Nanoparticles with Tunable Plasmonic Properties. *Journal of the American Chemical Society* **2007**, *129*, 8698.

(19)   Bondi, J. F.; Misra, R.; Ke, X.; Sines, I. T.; Schiffer, P.; Schaak, R. E. Optimized Synthesis and Magnetic Properties of Intermetallic Au3Fe1−x, Au3Co1−x, and Au3Ni1−x Nanoparticles. *Chemistry of Materials* **2010**, *22*, 3988.

(20)   Fan, Z.; Shelton, M.; Singh, A. K.; Senapati, D.; Khan, S. A.; Ray, P. C. Multifunctional Plasmonic Shell–Magnetic Core Nanoparticles for Targeted Diagnostics, Isolation, and Photothermal Destruction of Tumor Cells. *ACS Nano* **2012**, *6*, 1065.

(21)   Chen, S.; Jenkins, S. V.; Tao, J.; Zhu, Y.; Chen, J. Anisotropic Seeded Growth of Cu–M (M = Au, Pt, or Pd) Bimetallic Nanorods with Tunable Optical and Catalytic Properties. *The Journal of Physical Chemistry C* **2013**, *117*, 8924.

(22)   Crane, C. C.; Wang, F.; Li, J.; Tao, J.; Zhu, Y.; Chen, J. Synthesis of Copper–Silica Core–Shell Nanostructures with Sharp and Stable Localized Surface Plasmon Resonance. *The Journal of Physical Chemistry C* **2017**, *121*, 5684.

(23)   Peng, S.; Wang, C.; Xie, J.; Sun, S. Synthesis and Stabilization of Monodisperse Fe Nanoparticles. *Journal of the American Chemical Society* **2006**, *128*, 10676.

(24)   Hodges, J. M.; Biacchi, A. J.; Schaak, R. E. Ternary Hybrid Nanoparticle Isomers: Directing the Nucleation of Ag on Pt–Fe3O4 Using a Solid-State Protecting Group. *ACS Nano* **2014**, *8*, 1047.

(25)   Ho, C.-H.; Tsai, C.-P.; Chung, C.-C.; Tsai, C.-Y.; Chen, F.-R.; Lin, H.-J.; Lai, C.-H. Shape-Controlled Growth and Shape-Dependent Cation Site Occupancy of Monodisperse Fe3O4 Nanoparticles. *Chemistry of Materials* **2011**, *23*, 1753.

(26)   Lopes, G.; Vargas, J. M.; Sharma, S. K.; Béron, F.; Pirota, K. R.; Knobel, M.; Rettori, C.; Zysler, R. D. Ag−Fe3O4 Dimer Colloidal Nanoparticles: Synthesis and Enhancement of Magnetic Properties. *The Journal of Physical Chemistry C* **2010**, *114*, 10148.

(27)   Brollo, M. E. F.; López-Ruiz, R.; Muraca, D.; Figueroa, S. J. A.; Pirota, K. R.; Knobel, M. Compact Ag@Fe(3)O(4) Core-shell Nanoparticles by Means of Single-step Thermal Decomposition Reaction. *Scientific Reports* **2014**, *4*, 6839.

(28)   Comin, A.; Korobchevskaya, K.; George, C.; Diaspro, A.; Manna, L. Plasmon Bleaching Dynamics in Colloidal Gold–Iron Oxide Nanocrystal Heterodimers. *Nano Letters* **2012**, *12*, 921.

(29)   Espinosa, A.; Muñoz-Noval, A.; García-Hernández, M.; Serrano, A.; Jiménez de la Morena, J.; Figuerola, A.; Quarta, A.; Pellegrino, T.; Wilhelm, C.; García, M. A. Magnetic properties of iron oxide nanoparticles prepared by seeded-growth route. *Journal of Nanoparticle Research* **2013**, *15*, 1514.

(30)   Zhen, Z.; Xie, J. Development of Manganese-Based Nanoparticles as Contrast Probes for Magnetic Resonance Imaging. *Theranostics* **2012**, *2*, 45.

(31)   Meneghetti, D.; Sidhu, S. S. Magnetic Structures in Copper-Manganese Alloys. *Physical Review* **1957**, *105*, 130.

(32)   Damle, C.; Sastry, M. Low temperature alloying of Cu and Ni nanoparticles formed within thermally evaporated fatty acid films. *Journal of Materials Chemistry* **2002**, *12*, 1860.

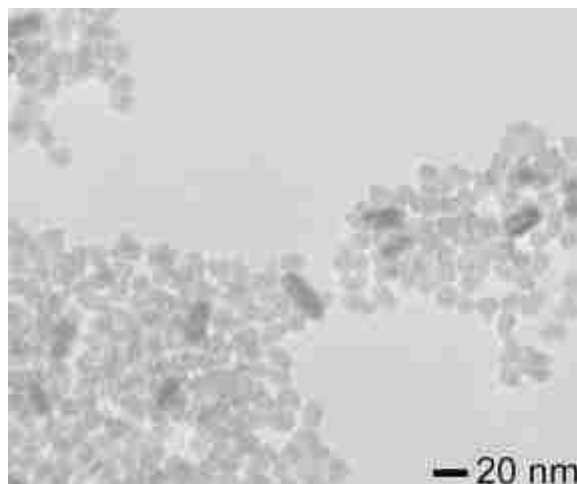# Appendix A: Supplemenal Information

Figure S1. TEM image of the product from the synthesis in which the same procedure as that of Figure 1B was used except the amount of Fe precursor was increased by 3 folds to 0.6 mmol.
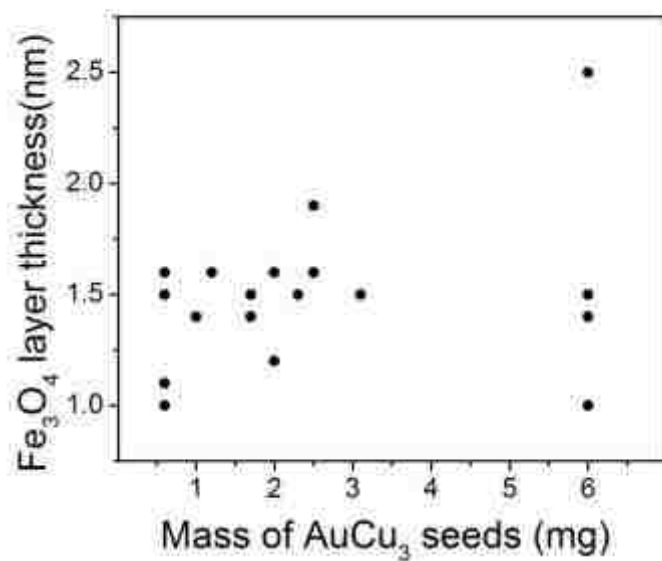
Figure S2. Scatter plot of measured iron oxide layer thickness as a function of total seed particle mass in the products from the synthesis in which the same procedure as that of Figure 1B was used except the amount of seeds was varied.
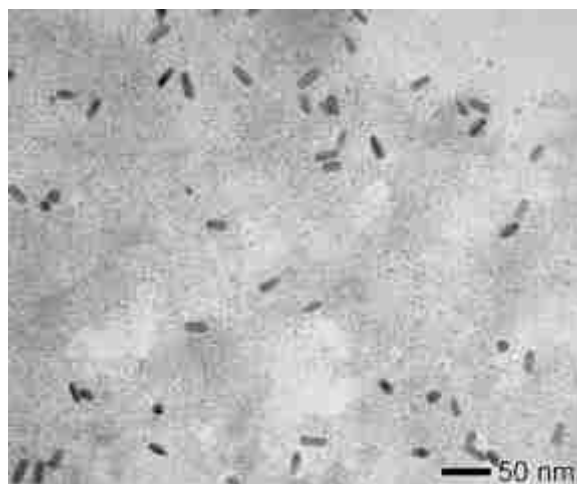
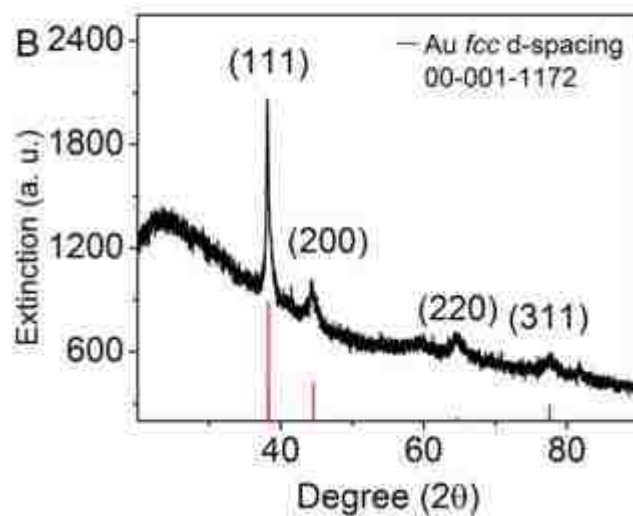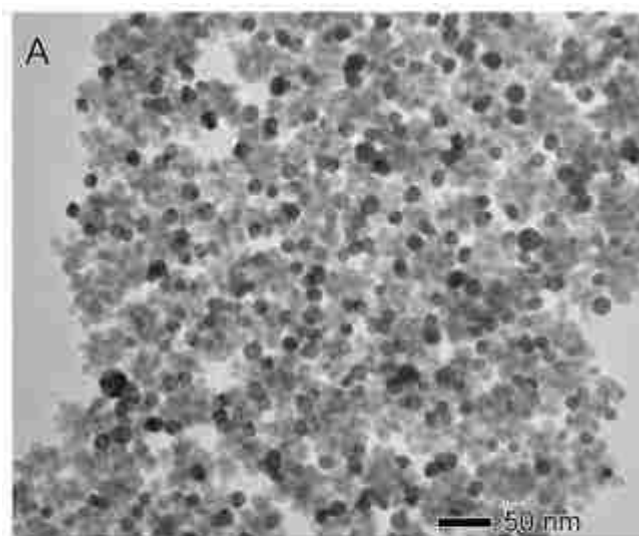**Figure S3.** TEM image of the product of the AuCu$_3$@NiO synthesis performed at a reaction temperature of 250$^{\text{o}}$C.

Figure S4. Characterization of the product of the AuCu$_3$@MnO synthesis performed at a reaction temperature of 250 ^{o}C: (A) TEM image; and (B) XRD pattern.
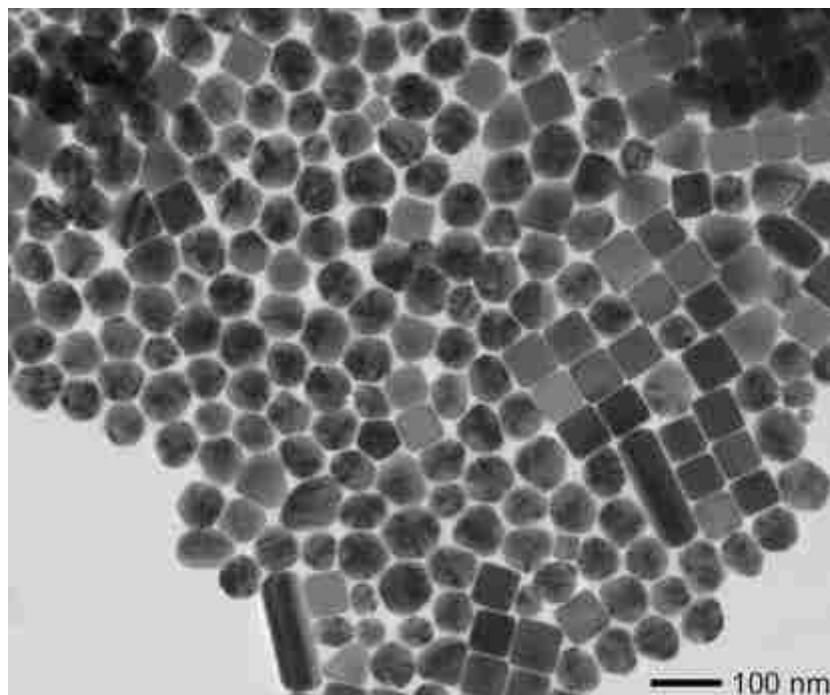
Figure S5. TEM image of the Cu seeds used for the deposition of the metal oxides shown in Figure 8.
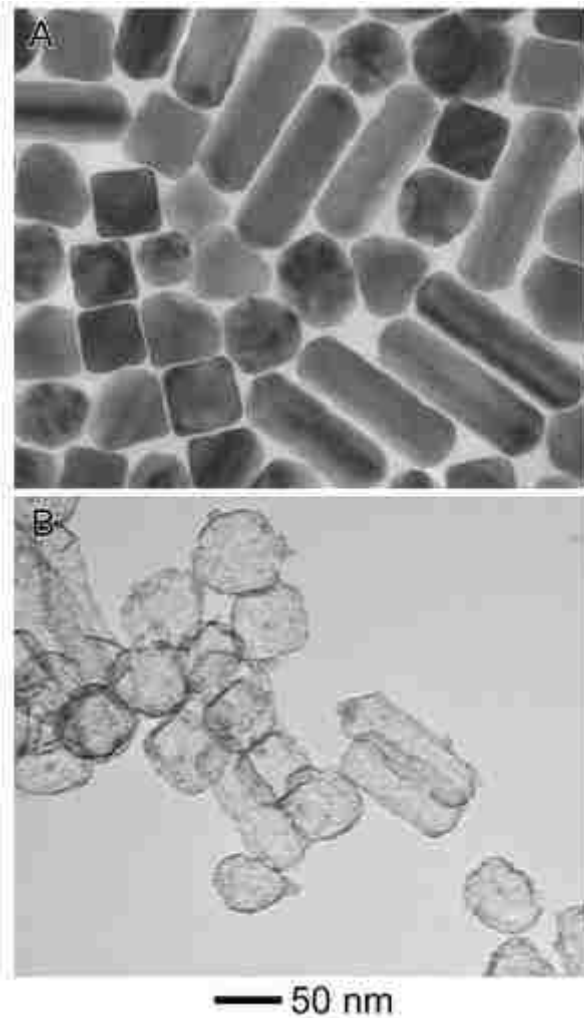
Figure S6. TEM images of the Cu seeds with a mixture of particles and rods used for the deposition of the iron oxides: (A) before the coating process; and (B) after coating and etching process.
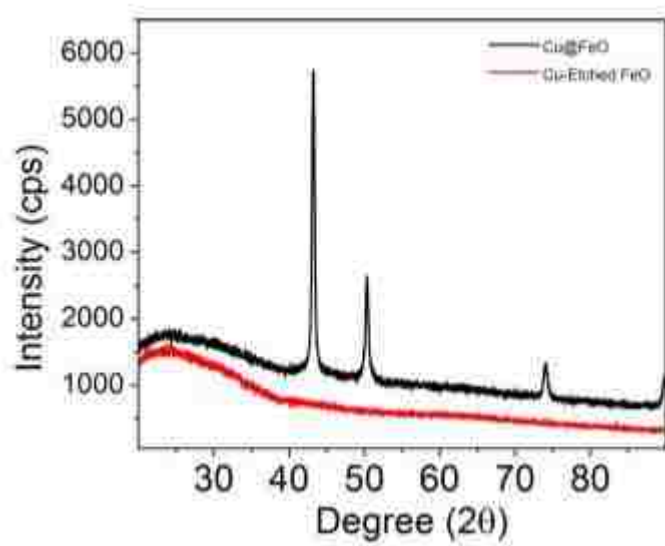
Figure S7. XRD pattern of Cu@Fe$_3$O$_4$ core-shell structure and hollow Fe$_3$O$_4$ shell.

Chapter V. Conclusion

This work develops several wet chemical methods to synthesize hybrid nanostructures with multiple functional materials which can find uses in various applications. These methods are summarized below along with future outlook for the continuation of this research.

The MASG approach was developed using SiO_2 as a mask, to partially protect the surface of seeds from further reaction, and subsequently applied to synthesize Pd-Au and Pt-Au heterodimers and Pt-Pd-Au heterotrimers. This approach is based on the textbox approach in organic synthesis of protection and deprotection. The initial $Au-SiO_2$ dumbbell, or Janus, structures were readily synthesized by modifying the amount of silica precursor in the microemulsion reaction system. The initial anisotropy produced a platform for forming bi-metallic Janus heterostructures. The relative energy barriers for homogeneous crystal growth for Pt and Pd manifested themselves in the final shape of the nanoparticle; Pd preferred to grow heterogeneously to produce mushroom cap like structures on the Au, while Pt preferred homogeneous growth, resulting in dendritic arms of Pt extending away from the Au surface. The extinction spectra, arising from the Au component of the nanostructure, provide a rapid method to determine thickness of the secondary material, as well as concentration, without time consuming total metal analysis techniques. Therefore, the described masking and unmasking approach is a versatile strategy to rationally synthesize heteronanostructures with multi-components, improving existing applications and finding new uses in many areas related to energy conversion and storage. An attractive next step for this approach is to extend the second metal into more reactive transition metals such as Cu, although additional steps must be developed to prevent premature oxidation of the Cu.

Cu nanostructures exhibit highly efficient coefficients of absorption and scattering, similar to Au and Ag nanostructures, but because of the reactivity of Cu, very few instances of solution phase Cu nanostructures have been studied for their optical properties. By incorporating the surfactant TOP as a Cu nanoparticle capping agent to prevent oxidation during the sol-gel process, Cu-SiO$_2$ core-shell structures were readily produced and persisted in water. The protective SiO$_2$ layer was so successful at preventing oxidation and aggregation of the particles, that the LSPR spectra was improved after the particles were phase transferred into water. This enhanced spectral measurement allowed Cu nanorods to be distinguished from nanocubes that had previously exhibited indistinguishable spectra. It was also found that the extinction efficiency of the cubes and nanorods was dramatically higher than spherical Cu particles. The addition of Cu to already available high quality Au-SiO$_2$ and Ag-SiO$_2$ core-shell nanostructures will be a low cost alternative to these nanoparticles for catalysis and sensing applications. Additionally, this approach can be used to determine if nanorods are present in mixture of nanorods and nanoparticles that has poor colloidal stability, without requiring TEM imaging.

The decomposition of zero valence first row transition metals onto preformed Cu-based seed nanostructures was used to produce core-shell structures with very thin metal oxide shells. The thickness of the oxide shell was limited by the temperature and by the self-nucleation potential of the zero-valence transition metal precursors. This metal oxide coating preserved the original seed particle's shape, and the original optical spectra arising from the LSPR when the shell was 2 nm or less in thickness, while also incorporating magnetic properties and changing the surface properties of the original particles, producing multi-functional nanostructures. Additionally, the oxide shells, when prepared on an easily etched metal such as Cu, can be

converted into hollow metal oxide nanostructures that may find use in drug delivery, electrode materials, high surface area catalysis, and magnetic imaging.

These approaches produce highly uniform nanostructures of multiple materials, and aid in the expansion of colloidal nanoparticle synthesis beyond noble metals and ads to the toolbox of chemical reactivity for rationally synthesizing complex nanostructures. These multifunctional materials will find use in catalytic and sensing applications, and can serve as platforms to replace more expensive noble metals Au and Ag.